Fakultät für Physik
Physik-Department E16
der Technischen Universität München

DETERMINATION OF THE COMPOSITION AND SIZE OF THE LUMINESCENT PARTICLES IN POROUS SILICON BY THERMAL EFFUSION OF HYDROGEN

Anastas Nikolov

Vollständiger Abdruck der von der Fakultät für Physik
der Technischen Universität München zur Erlangung des
akademischen Grades eines Doktors der Naturwissenschaften
(Dr. rer. nat.) genehmigten Dissertation.

Vorsitzender:	Univ.-Prof. Dr. M. Kleber
Prüfer der Dissertation:	1. Univ.-Prof. F. Koch, Ph.D. em.
	2. Univ.-Prof. Dr. Dr. h. c. St. Veprek, i. R.

Die Dissertation wurde am 09.05.2005 bei der Technischen
Universität München eingereicht und durch die Fakultät
für Physik am 20.10.2005 angenommen.

An meine Großmutter Elena, die mich großgezogen hat und an meine Tante Pobeda, die mich immer unterstützt hat.

CONTENTS

1. Introduction **6**

2. Fabrication of Porous Silicon 12

2.1. Brief History 12

2.2. Electrochemical Cell 12

2.3. Preparation Parameters of the Investigated Samples 14

2.4. Structure 16

2.5. Dissolution Chemistries 16

2.6. Formation Mechanism 17

3. Thermal Effusion Method for Porous Silicon Investigations **25**

3.1. Theory of Thermal Effusion 25

3.1.1. Adsorption and Desorption Concept 25

3.1.2. Thermal Desorption 27

3.1.3. Polanyi-Wigner Equation 29

3.1.4. Extraction of the Desorption Parameters 29

3.2. Experimental Equipment for Effusion Measurements 37

3.2.1. Description of the Apparatus 37

3.2.2. Measuring the Effusion Rate 42

3.2.3. Measuring the Absolute Gas Quantity 42

4. Gravimetry and Effusion of Hydrogen at a Constant Temperature for the H/Si Atom Ratio Determination **46**

4.1. Gravimetric Method 46

4.2. H/Si Atom Number Ratio as a Standard for the Surface to Volume Ratio of the Porous Silicon Structure 47

4.3. Experimental Results 47

4.3.1. Influence of the Etchcurrent Density 48

4.3.2. Influence of the Substrate Resistivity 49

4.3.3. Chemical Postetching 49

4.3.4. Influence of Illumination through Selected Filters during the Etching Procedure 50

4.4. Comments 51

4.5. Estimation of the experimental error in the method 53

4.6. Conclusions 55

5. Other Methods Used for Composition Determination 56

5.1. Elastic Recoil Detection Analysis (ERDA) 56

5.1.1. Principle 56

5.1.2. Theory 58

5.1.3. Data Analysis 59

5.1.4. Experimental Results 60

5.1.5. Comments 65

5.1.6. Conclusions 68

5.2. „Burning“ Method 70

5.2.1. Principle 70

5.2.2. Operation 70

5.2.3. Detection 72

5.2.4. Experimental results 72

5.2.5. Comments 73

5.2.6. Conclusions 75

6. EXAFS for the H/Si Atom Ratio Determination 77

6.1. EXAFS analysis: principles and accuracy 77

6.2. Data processing. Mean number of neighbor atoms 79

6.3. Case of bulk, amorphous and porous silicon 80

6.4. Influence of the surface reconstruction on the EXAFS signal 82

6.5. Conclusions 85

7. The Relationship between Luminescence and the H/Si Atom Number Ratio 88

7.1. Experimental conditions 88

7.2. Experimental results 88

7.3. Comments 90

7.4. Conclusions 94

8. Internal Surface Characterization of the Porous Silicon Structure 96

8.1. Effusion of Hydrogen as the Temperature is ramped 96

8.1.1. Typical Effusion Spectrum for Freshly prepared Porous Silicon 96

8.1.2. Experimental Results 97

8.1.3. Comments 102

8.1.4. Conclusions 108

8.2. Infrared Transmission Measurements 110

8.2.1. Experimental Conditions 113
8.2.2. Typical Infrared Transmission Spectra for Freshly prepared Porous Silicon 114
8.2.3. Experimental Results 114
8.2.4. Comments 118
8.2.5. Conclusions 130
9. Dimensions of the Particles Forming the Skeleton 133
9.1. Determination of Particle Size from the Experimental Data 133
9.2. Results and Comments 138
9.3. Comparison with Data Available in the Literature 140
10. Summary 146
11. Acknowledgements 149

Chapter 1. INTRODUCTION

Crystalline silicon has been the dominant material in electronics for the last three decades of the former and into the beginning of the current century. It has been investigated more thoroughly than any other material and its technological applications developed to a very high level. Present microelectronics, as the basis for modern information technology, is over $90\ \%$ based on silicon-CMOS technology. The properties of the elemental semiconductor Si and its oxide enable ultra large-scale integration (ULSI). The desire to combine optoelectronic devices with silicon microelectronics has lead to the search for Si-based materials and structures that emit light with high quantum efficiency. Crystalline silicon has a relatively small $(\sim 1.1\ \mathrm{eV})$ indirect band gap [see *Landolt*] and does not display efficient light emission. The radiative recombination of electrons excited into the conduction band minimum leaving a hole created in the valence band maximum requires the participation of a phonon to conserve momentum. Such electrons have to remain in the exited state for a long time in order to allow the necessary momentum transfer and most of them recombine non-radiatively at a surface or volume defect to produce heat. The band-to-band luminescence of bulk silicon occurs in the near infrared with an efficiency of usually $0.0001\ \%$ (i.e. one photon is produced for every million charge carrier recombinations) [see *Canham*]. One general approach to overcoming the indirect nature of the optical transition in Si is to relax the k-selection by exploiting the spatial confinement in low-dimensional Si nanostructures. These belong to one of the fastest growing areas of semiconductor research. Three categories are usually considered: two-dimensional (**2D**) quantum wells, one-dimensional (**1D**) quantum wires, and zero-dimensional (**0D**) quantum dots. One well-known effect within these structures, the so-called „quantum size“ or „quantum confinement“ effect, is band-gap widening caused by carriers acquiring a significant quantum energy of localization. This effect commonly occurs in structures with dimensions less than $10\ \mathrm{nm}$ and is more pronounced where the electronic charge carriers are confined in more than one dimension.

Theoretical particle-in-a-box calculations using the effective-mass theory predict a significant increase of the band gap in the region $1-5\ \mathrm{nm}$, as illustrated on fig.1.1. It can be seen that the entire visible spectral range $(1.6-3.2\ \mathrm{eV})$ is attainable.

Experimentally, luminescent materials have been produced in the entire visible range from red to violet under carefully controlled conditions and external efficiencies approaching $10\ \%$

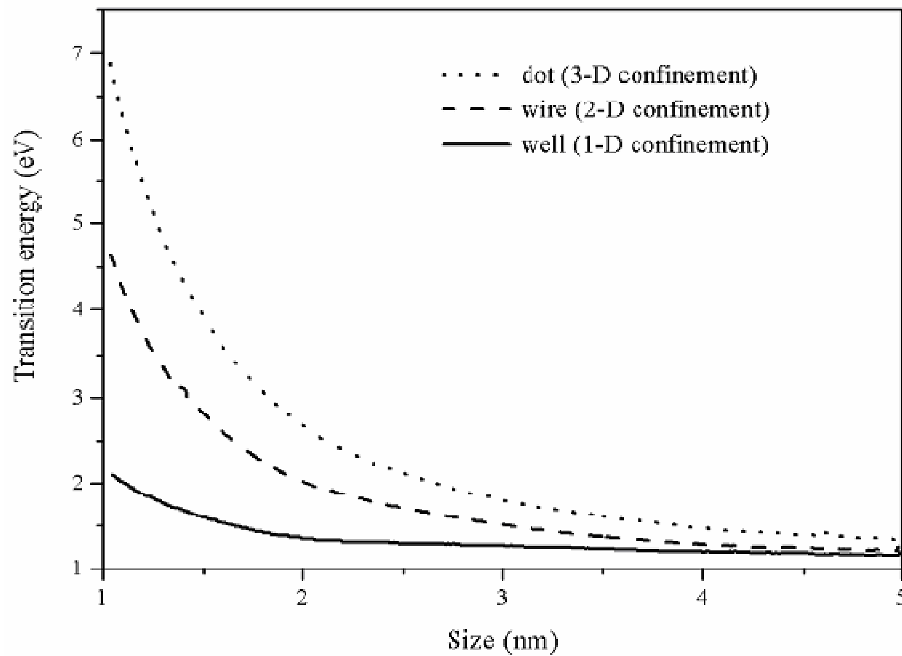

Fig.1.1: Predicted band gap increase in Si low-dimensional structures [after *Canham*].

(i.e. one hundred thousand times higher than that of bulk Si) have been obtained for orange-emitting structures at room temperature. Blue shift of the absorption coefficient of these materials compared to crystalline silicon can also be demonstrated by optical transmission experiments. The more the luminescence of one material approaches the high-energy end of the visible spectrum, the more blue-shifted is its absorption coefficient. All this is an indication of a dramatically modified Si band gap.

Another feature specific to the sponge-like porous silicon structure, and probably very important for an understanding of its optical behavior, is the vast internal surface (~ hundreds m^2/cm^3). This consists of a wide variety of molecular species which can participate in the luminescence in the same energy range as quantum sized crystallites might be expected to do. The enhanced surface to volume ratio, in any case, naturally inspires the idea that the physical and electronic surface structure strongly affects all properties of the structure, including the optical.

It is important from a scientific and technological point of view that the origin of the photoluminescence shift be understood. In spite of intensive experimental and theoretical investigations, no conclusive argument on the mechanism for efficient light emission has yet been given. Among the proposed models, three distinct categories can be distinguished:

(a) „pure“ quantum confinement effects in Si wires and dots,

(b) molecular agents, and

(c) surface localization states on Si nanocrystallites.

The first hypothesis asserts that the luminescence is a result of the radiative recombination of quantum-confined electrons and holes in columnar structures or modulated wires associated with silicon nanoparticles. The second model attributes the porous silicon (PS) luminescence to specific molecular luminescence centres such as polysilanes (Si_nH_m), silicon hydride complexes, and siloxane or siloxane-based molecular compounds. Finally, the third hypothesis, the surface-modified quantum picture („smart" quantum effect), suggests the importance of localized surface states created by irregularly shaped small crystallites which are not perfectly passivated and into which elementary excitations can be trapped prior to recombine radiative as bound states.

The methodology used for the calculation of the electronic structure, specifically the up shift from the bulk-Si value of the band gap, can be classified as semi-empirical, mainly employing the tight binding scheme, or first principal based and the calculation is premised on an assumed geometrical structure. Generally, the calculated energy gap is proportional to the reciprocal or inverse square of the crystal size, depending on the method. An experimental determination of this parameter is crucial for understanding the role of the electrons quantum confinement and enables the two hypotheses, the „pure" and the „smart" quantum effect, to be tested.

Several physically completely different approaches have been used to attack this complex task. The difficulties in determining luminescence particle shape and dimensions arise mainly from the inhomogeneity of the medium and the fact that structures < 20 Å are beyond practical detection with most of the methods used. The following group represents techniques with the potential for direct observation and estimation of particle size:

- transmission electron microscopy (TEM);
- scanning tunneling microscopy (STM);
- atomic force microscopy (AFM).

A few indirect methods have been also applied where a mathematical analysis of the experimental curve is necessary to provide the desired information. These include:

- X-ray diffraction – the average size of the crystalline microparticles can be calculated from the measured width of their diffraction curves using the Scherer formula.

- Small-angle X-ray or neutron Scattering (SAXS or SANS) – structural details have to be deduced either from the shape of the scattering function in reciprocal space or from the distance distribution function in real space.

- Raman spectroscopy – the line shift and shape of the one phonon Raman peak is used to estimate the crystal size.

A fourth group of indirect measurements exists which utilizes the well-known fact that the surface of the porous structure Si-skeleton is covered with H. Experimental determination of the H-atoms number enables an estimation of the particle size assuming:

a) a certain type of H-bonding. Specifically, the average number of H-bonds per unit Si-surface,

b) the shape of the luminescent crystallites having deduced the total number of Si atoms from the skeleton weight.

We have employed the thermal effusion of H as a main technique combined with more limited use of two other methods:

a) elastic recoil detection analysis (ERDA) and

b) “burning” in an O_2 atmosphere to determine respectively the relative quantity of H-atoms and the ratio of the H-atom number to the Si atom number in the porous structure $\left(N_H/N_{Si}\right)$.

Another approach reported in the literature, extended x-ray absorption fine structure (EXAFS), deals with the coordination number of the Si atoms $< X >$ in the porous Si sample. This final method also provides a check on $\left(N_H/N_{Si}\right)$ in that $N_H/N_{Si} = 4 - < X >$ and in this way the two experiments, the latter and the thermal effusion, complement one another. Two research groups have employed EXAFS and published their conclusions but there are great differences between the experimental results they have reported and the thermal effusion results. These discrepancies are the cause for the present work, whose aim is to take one step forward, via the method of thermal effusion, in the direction of solving the complicated problem of particle size determination in porous silicon.

Chapter 2 deals with the technique used to prepare the samples utilized in the present work. The reason for the wakened interest to this long known material through the last thirteen years is pointed out. The porous silicon production setup is sketched and various parameters, which influence the microstructure, including the etching velocity, are presented. The two types of porous structure, the chemistry behind their formation and the different proposed models for the formation mechanism are described and briefly commented upon.

In Chapter 3, the basic concepts and the theoretical approach to describing thermal effusion are presented. The two main groups, integral and differential, of various procedures for desorption spectra analysis and derivation of the kinetic parameters, which the Polanyi-Wigner equation contains, are indicated. Attention is focused on one integral method which, in our opinion, is appropriate for the description of the desorption spectra obtained in the current work. The second part of the chapter is concerned with a detailed description of the

measuring equipment used and the two different ways of performing the experiment to obtain either the effusion rate or the absolute gas quantity.

Chapter 4 contains a description of the gravimetric method which, combined with the thermal effusion results, enables H/Si atom number ratio determination for the porous samples investigated. The relationship of this ratio to the surface area to volume ratio of the particles forming the skeleton of the porous structure is pointed out. Different procedures for achieving a wide range of values for the hydrogen to silicon atom number ratio are described and the experimental error is estimated.

In chapter 5, two other methods for composition determination, which have been applied to our samples, are presented. They are used as an additional source of information to confirm the thermal effusion results and to make them more reliable. The principle, the theory and the experimental data analysis of the first method, the elastic recoil detection analysis (ERDA) performed with highly energetic heavy ions, are briefly described. The results from a selected series of porous samples are analyzed and compared to the results reported in the literature and to thermal effusion results of similar structures. The absence of significant oxygen quantity in freshly prepared samples is established. The second method, “burning” in an O_2 atmosphere, is applicable only to freestanding mesoporous structures. The principle of oxidative combustion, the technical embodiment of the fully automatic instrument, a “vario EL” elemental analyzer, by which the measurement is performed and its operation are described briefly. The results obtained are compared to thermal effusion results from freestanding mesoporous samples and the characteristics of this comparison are commented upon.

Chapter 6 deals with the extended x-ray absorption fine structure (EXAFS) method for H/Si atom number ratio determination. The reported literary data differs drastically from the thermal effusion results obtained for similar samples. In our opinion, the erroneous results arising when this method is applied to nanostructures are due to neglected role of the atom displacement and bond distortion on the internal surface of the porous silicon.

In chapter 7, the correlation established between the hydrogen to silicon atom number ratio and the position of the visible luminescence peak maximum for the porous silicon samples under consideration is shown. The greater the atom number ratio considered, the stronger the luminescent peak maximum blue shift of the corresponding porous structure is.

Chapter 8 is dedicated to the properties of the skeleton surface. Two appropriate methods deal with surface orientation, the type of the hydride coverage and the relation between the presented mono-, di- and trihydride bonds. Contrary to the predominant conception in the

literature, the analysis of the experimental results from the thermal effusion rate measurements shows that there is no preferential surface orientation. The surface is a combination of differently oriented plains with many steps and corners rather than amorphous. A local reconstruction is not excluded. It is populated mainly by mono- and dihydrides whose ratio decreases with H/Si atom number ratio increase for a particular porous structure. The experimental results from the infrared transmission measurements confirm the conclusions from the thermal effusion rate measurements concerning the skeleton surface orientation. As a consequence, an effective bending of the considered surface is conceivable. It is confirmed that the as-prepared samples are, and properly treated remain, free of oxide for at least two hours in air. An attempt at an unambiguous assignment of the features in the infrared spectrum by means of experiments with deuterium-terminated porous silicon didn't succeed. Regardless of the seeming simplicity of the infrared spectrum, it remains incompletely understood and needs further investigation. The existing contradictions in the literature are noted and are, in our opinion, connected with imperfections in the experiments. Their concrete modification is proposed.

In chapter 9, a model, which connects the experimental data with the particle size, is presented. The limitations of the proposed approach are pointed out. An extensive overview of the available theoretical and experimental data is performed.

Chapter 10 contains a short summary of the results discussed in this thesis.

Each chapter is divided into a variable number of sections followed by short conclusions and references.

References

1. *Landolt* Landolt-Börnstein, Numerical Data and Functional Relationships in Science and Technology **17a**, Springer-Verlag Berlin-Heidelberg-New York 1982, p.359.
2. *Canham* L. Ganham, Physics World, p.41 (March 1992).

Chapter 2. FABRICATION OF POROUS SILICON

2.1. Brief history

Porous Si was discovered in 1956 by Uhlir [see *Uhlir*] and later investigated by Turner [see *Turner*] in 1958 at Ball Labs in the USA during electro-polishing studies of Si in HF-based solutions. It was initially believed that the deposit on the surface of the monocrystal was Si suboxide. The real porous nature of the structure was first reported by Watanabe and co-workers [see *Watanabe*]. The intention had been to employ the material under consideration for dielectric isolation of active Si devices. A great interest was awakened and new possibilities for utilizing the porous silicon were opened after Canham [see *Canham1*] and, independently, Lehmann and Gösele [see *Lehmann1*] reported the observation of an effective photoluminescence from porous silicon at room temperature. Cullis et al. [see *Cullis*] illustrated the increased attention to this material by means of a histogram of the total number of publications per year in the period from the discovery of this structure till 1997.

2.2. Electrochemical Cell

The electrolytic cell for porous silicon formation used in the current study is schematically shown in fig.2.1. The setup is similar to the one used by Turner while its modifications are known in the literature [see *Kozlowski*]. A great advantage of such equipment is its simplicity. The silicon wafer or substrate **2**, p-type in our case, serves as an anode. Its lower face **3** is in

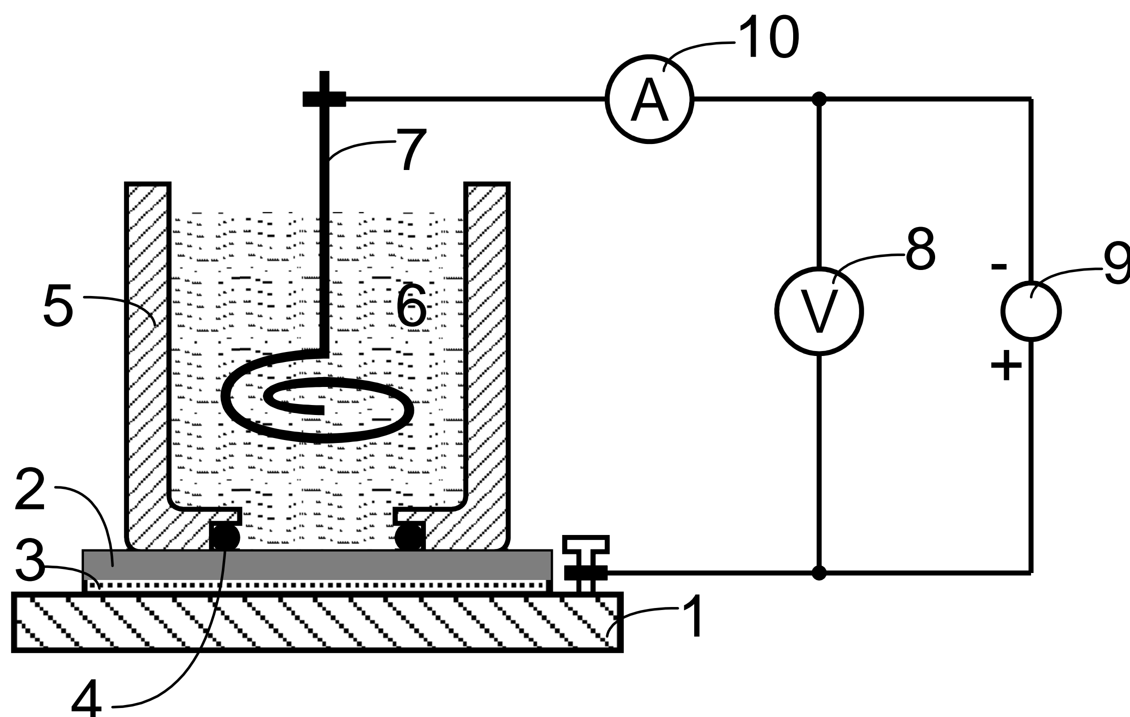

Fig.2.1: Sketch of the PS production setup.

contact with an aluminum plate **1** connected to the power supply **9**. For silicon wafers of low resistivity (usually $\sim$ few mΩ.cm), a good ohmic contact is obtained without the need of an additional metal contact on the substrate. Four possibilities have been utilized in the case of a high resistance material (typically $>$ few Ω.cm). First, an aluminum foil is pressed between the substrate and the aluminum plate. Because of the non-uniform pressure, a radial inhomogeneity of the porous structure has been observed. An alternative is to coat the lower face of the substrate with gallium. The latter has a low melting point of about $30\ ^{o}\mathrm{C}$ and can easily be spread over the silicon surface by, for instance, an aluminum bar to form a Schottky contact. For our sample, gallium was smeared sideways so that the lower face of the substrate just under the sample remains clean and enables infrared transmission measurements. The lateral positions of the gallium contacts allow for their removal by breaking off after sample preparation. In this way, the effusion measurement also becomes possible. Placing the gallium in the effusion installation is not desirable because of the danger of contamination. One disadvantage of such a contact position is the expected non-ideal structural uniformity as a consequence of the specific distribution of the current density lines. Better results in relation to the uniformity have been achieved by evaporating aluminum onto the substrate followed by annealing. This latter approach is unacceptable, however, since it becomes impossible for infrared measurements to be performed directly after the preparation of the samples. For such measurements, it becomes necessary for the lower face of the sample to be additionally treated with HF acid: a process that exacerbates the risk of damage, especially for highly porous structures. Implantation is the most appropriate means for avoiding this difficulty. In our case, (p-type material) boron $\left(^{11}\mathrm{B}\right)$ was implanted (dose $5\mathrm{x}10^{15}\ \mathrm{I/cm^{2}}$) before thermal annealing in an inert gas at $500\ ^{o}\mathrm{C}$ for 30 minutes. Under these conditions, a highly conductive layer a few microns thick is formed. This enables uniform samples to be obtained and is not a barrier to infrared radiation.

The upper face of the wafer is polished and exposed to the etching solution. The anodizing electrolyte **6** is placed in a cylindrical cell **5** made of Teflon (a highly acid-resistant polymer). A circular opening at the bottom of the container enables contact between the etching solution and the substrate and defines the form of the sample. The connection of the cell to the substrate is sealed by a viton (acid-resistant material) o-ring **4**, preventing the solution from leaking around the hole. Cells with four different diameters of opening together with their respective o-rings of $1.9, 8.5, 15$ and $32\ \mathrm{mm}$ have been utilized. The cathode is made of platinum wire **7** (HF-resistant) wound into a spiral in one plane to maintain homogeneity of

the current density field, as far as possible, during the etching process. The platinum wire is immersed in the etching solution and, on its return side, is joined to the power supply. The volt- **8** and ammeter **10** included in the electrical circuit enable simultaneous monitoring of the anodic current and potential. The etching set is placed in a plastic (HF -vapor resistant) box and the whole installation for photo-electrochemical etching is covered with a black coat to avoid the influence of room lighting on the anodization procedure. For the illumination-assisted process, a box with a circular opening on the upper side has been used. The light source was a 100 W halogen lamp. An optical diffuser provided for a homogeneous exposure over the whole sample area. Before reaching the surface of Si wafer, the light passed successively through a low-pass filter and a plastic foil. The latter, set across the opening of the box, is transparent to the irradiation and also HF -vapor resistant to protect the optical elements from the potentially damaging influence of the acid. The distance between the halogen lamp and the sample is about 25 cm .

2.3. Preparation parameters for the investigated samples

The following parameters are well known to influence the microstructure and need to be taken into account or controlled during the etching: the type of Si wafer (n- or p- type) and its resistivity, crystallographic orientation, electrolyte composition, temperature, current density, and light illumination (or absence) during anodization. The silicon wafers used for this study were p-type (boron doped) of various resistivities in the range $0.001 \div 200\ \Omega.\text{cm}$, from (100) oriented single crystals grown by the Czochralski method. The wide spectrum of resistivities makes it possible for both types of porous structures – mesoporous, characteristic of heavily doped (degenerate) silicon (dopant concentration of $\sim 10^{19}\ \text{cm}^{-3}$), and finer structured, typical of a lightly doped substrate ($\sim 10^{15}\ \text{cm}^{-3}$) - to be obtained and investigated.

The (100) orientation samples had been chosen **firstly** because such wafers are mostly utilized in microelectronics for the oxide quality on their surface and **secondly** because it is maintained in the literature that the pores selectively propagate in this direction. Such a choice assures the high in-plane structural homogeneity that is essential for the variety of optical measurements that are to be made.

All results in this work were obtained on samples etched by a 50% HF (acid with water) solution mixed with an equal part of ethanol $(1:1)$ giving a final volumetric ratio of $HF : H_2O : C_2H_5OH = 1:1:2$. It is known that during the chemical dissolution, hydrogen evolution takes place. When purely aqueous HF (without ethanol) solutions are used, the

hydrogen bubbles stick to the surface and induce lateral and in-depth inhomogeneity. The addition of a surfactant such as ethanol enables this problem to be overcome. For efficient bubble elimination, the ethanol concentration should not be less than 15%. The ethanoic HF solution completely infiltrates the pores and thus plays an important role in the flatness of the interface between the substrate and the porous Si. When the anodization is performed in a purely aqueous solution, the fluid can't penetrate completely into the pores due to the lack of wettability and capillary phenomena. Without a surfactant, the dissolution reaction, which takes place at the interface, is not uniform, thus leading to interface roughness and thickness inhomogeneity. Finally, the role of ethanol is to improve the PS layer uniformity by eliminating hydrogen bubbles and so improving electrolyte infiltration.

The current densities used lie in the region $1-1000\ \mathrm{mA/cm^2}$. A $100\ \mathrm{W}$ halogen lamp and a selection of colored glass low-pass filters with cut-off wavelengths at 665 (RG-665), 550 (RG-550) and 450 (WG-450) nm respectively were utilized for the light-assisted anodization of those samples not produced either in the dark or using direct illumination without any filter. The thickness of the samples was chosen according to the penetration depth of the incident light at the different wavelengths, which is important to achieve longitudinal (in-depth) homogeneity. Considering that the illumination can be viewed as having been adsorbed by that point at which its intensity becomes equal to or less than 10% of the initial intensity, the penetration depth is given by: $d \approx 1/\alpha(\lambda)$ (where α is the absorption coefficient, λ - the wavelength). Since low-pass filters have been used and the incident light is not monochromatic, the shortest wavelength of a particular beam has to be considered a porous structure definer. After removing of the electrolyte, the samples were blown dry by an inert gas, e.g. nitrogen, to reduce the rate of oxidation.

The only formula one can find in the literature for the etching-velocity applies to microcrystalline porous silicon [see *Möller*]. For the empirical etching-velocity $R\ [\mu\mathrm{m/min}]$ dependent on the magnitude of the etch-current density $j\ [\mathrm{mA/cm^2}]$ lying in the interval $3\ \mathrm{mA/cm^2} \le j \le 2000\ \mathrm{mA/cm^2}$ at substrate resistivity $\rho = 1-5\ \Omega\mathrm{cm}$ in an etching solution of 50% HF and ethanol (C_2H_5OH) in the volume ratio $1:1$, a valid the empirical expression is:

$$\log R = 0.89 \log j - 1.2. \tag{2.1}$$

Our experience shows that at a substrate resistivity of about $\rho = 1\ \mathrm{m}\Omega\mathrm{cm}$ (mesoporous silicon) and the same etching solution, the etching time for the same sample thickness is about 0.6 times the calculated value.

2.4. Structure

Beal et al**.** [see *Beal1*, *Beal2*] have investigated porous material using cross-sectional transmission electron microscopy. They have shown that for the p-type doped substrate material, two types of porous structure can be distinguished (see fig. 2.2). The doping level is decisive in determining which type of structure is developed during the etching process. In heavily doped silicon (see fig. 2.2-a), the structure consists of many long voids running perpendicular to the surface. There are also many small 'buds' on the sides of the pores and

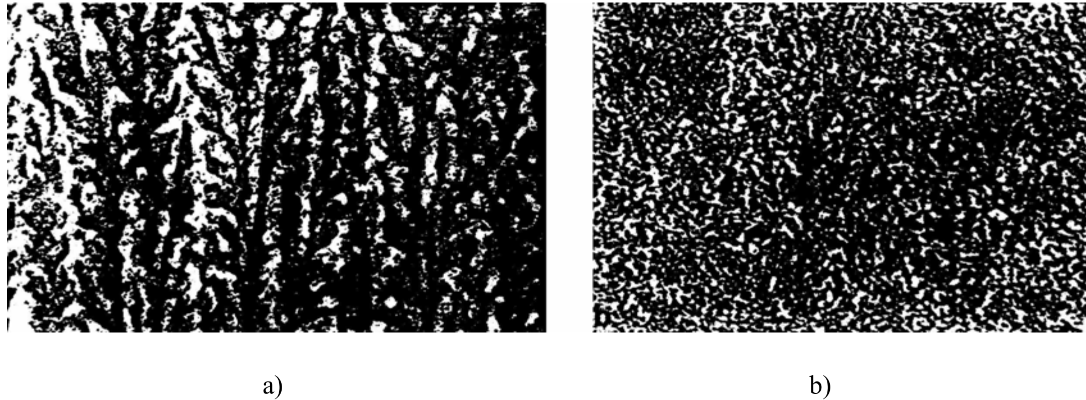

a) b)

Fig.2.2: Cross-sectional transmission electron micrographs of a) heavily doped (0.01 Ω.cm) and b) lightly doped (25 Ω.cm) p-type silicon [after *Beal2*].

occasional branches, which emerge at wide angles to the main pores. In lightly doped silicon (see fig. 2.2-b), the pore structure is not obviously directional but consists of an apparently random array of fine holes. The images suggest that the pores wander in a semi-random manner. As the electrolyte must be able to penetrate into the structure for the removal of silicon to occur, it is evident that the pores must be continuous from the surface. The pore size increases with reduction in density for both microstructures. However, the size of the voids in non-degenerate material is, in general, significantly smaller than those in degenerate material of comparable density. The distinction between the two types of microstructure existed over the full range of film densities studied, i.e. it was determined by the doping level of the silicon. The microstructure of the films investigated was found to be depth independent.

2.5. Dissolution chemistries

The overall reaction mechanism of the silicon anodic dissolution in HF media is still incompletely understood, although it is generally accepted that holes are required in the initial steps of the process. There are several reaction scheme proposals, but it appears from all available data that the mechanism presented by Lehmann and Gösele [see *Lehmann1*] is the main chemistry behind the formation of porous silicon. For this formation, is essential that a

silicon surface saturated with hydrogen (according to the authors' supposition – SiH_2 at the beginning) is inert against attack by fluoride ions as long as no holes (h^+) are available in the vicinity of the surface. This is because the electro-negativity of H is similar to that of Si and both the polarization of the bond and the induced polarization are low. If a hole (h^+) reaches the silicon/solution interface, an attack on $Si-H$ bonds by fluoride ions can occur and a $Si-F$ bond is established. Due to the polarizing influence of the bonded F, another F^- ion can attack and bond causing the generation of a H_2 molecule and the injection of one electron into the electrode. Because of the polarization induced by the $Si-F$ groups, the electron density of the $Si-Si$ back-bonds is lowered and HF or H_2O will now attack these weakened bonds while the silicon surface atoms remain bonded to hydrogen. If a silicon atom is removed from an atomically flat surface by this reaction, an atomic size dip remains. Such a change in the surface geometry will change the electric field distribution in such a way that hole transfer occurs preferentially at this location. Therefore, surface inhomogeneities are amplified.

This model provokes some justified questions, which must be addressed. The bond energy for $Si-F$ is the highest of all possible surface species, $Si-F\ (129.3\ \text{kcal/mol}) > Si-O\ (88.2\ \text{kcal/mol}) > Si-H\ (70.4\ \text{kcal/mol}) > Si-Si\ (42.2\ \text{kcal/mol})$, which indicates that fluoride adsorption should be prevalent at the silicon surface since it is the most thermodynamically stable bond. However, experimental results (secondary-ion mass spectrometry (SIMS), nuclear reaction analysis (NRA), Rutherford backscattering (RBS)) have shown surprisingly small amounts of surface fluoride (about 0.1 at.%). It appears that despite the thermodynamic stability of the $Si-F$ bond, it does not remain on the silicon surface in any stable, readily measured, form but is extremely important to the chemical reactivity of silicon. It is known that HF treated silicon surfaces are less reactive to oxidation and have a lower density of surface states than untreated ones. The cause has been assigned to the presence of surface hydrides and fluoride is proposed as the active "catalyst" which loads the surface with hydrides. Despite the relative bond energies of $Si-F$ and $Si-O$, the surface $Si-F$ bond quickly hydrolyzes to $Si-OH$ and $Si-H$ in the presence of water. The mechanism is not completely understood.

2.6. Formation mechanism

There exist three independently proposed models which try to explain pore formation in porous silicon [see *Smith1*]:

(1) the Beal model [see *Beal1, Beal2, Pickering*],
(2) the diffusion-limited model [see *Smith2, Smith3*] and
(3) the quantum-based model developed by V. Lehmann and U. Gösele [see *Lehmann1, Foll*].

The Beal model is based on a theory of electrostatic discharge and dielectric breakdown in which the electric field lines concentrate at surface irregularities, focus current flow at the pore tips and locally enhance the dissolution there. Two premises have to be considered. First of all, the material is only dissolved where an anodizing current flows. Secondly, the large surface state density of the silicon surface in the porous film results in pinning of the Fermi level in the gap. A consideration of the I-V curves has shown that they display some basic similarities to the normal Schottky diode behavior. The total voltage drop is treated as occurring in two regions connected in series. The first is the interface region that includes the surface states on the semiconductor surface and the screening layer in the electrolyte while the second is the bulk silicon up to the interface including the Schottky barrier. For lightly doped silicon in hydrofluoric acid, a rectifying contact is observed, which implies the presence of a potential barrier. This barrier is explained by the pinning of the Fermi level at the silicon surface somewhere near mid-gap. This pinning is a consequence of a large density of surface states at the silicon-electrolyte interface. The potential barrier has an associated depletion region that gives rise to the rectifying characteristics. The current flow is determined primarily by the height of the barrier; its width being relatively unimportant. This height can be reduced at the pore tips by applying a forward bias and exploiting image charge effects. These latter arise from the image charge induced in the surface states and the electrolyte by charge moving through the barrier. The lowering of the barrier is proportional to the electric field at the semiconductor-electrolyte interface, whose field, in its turn, is reciprocal to the pore tip radius. If a small protrusion forms on a pore, it will initially have a small radius of curvature and significant barrier lowering will occur. Preferential current flow, and therefore enhanced dissolution, will take place at this point. As the pore grows and its radius is increased, these effects are reduced and growth is retarded. Small protrusions are therefore formed. They initially grow rapidly but their growth rate then slows as another protrusion is initiated. The direction of growth of the individual pores is determined by the chance nature of the initiation of protrusions and is therefore itself of a random nature. However, the overall trend in the growth direction is determined by the general direction of current flow, i.e. normal to the surface. By these mechanisms, the formation of the random pore structure observed can be understood qualitatively. Some of the possible effects of the hydrofluoric

acid concentration and current density can also be explained qualitatively as follows. The current flow at the pore tips is through the Schottky barrier in series with this interfacial impedance. Two effects modify this current flow. Firstly, the image charge barrier lowering enhances the current flow through the Schottky barrier. This effect is increased by an increase in the surface electric field, which occurs only if a small fraction of the interface is occupied by pore tips. This current enhancement mechanism therefore favors the growth of a high-density porous film. Secondly, the voltage dropped at the interface impedance is minimized if the current is distributed over a large area of the interface. This effect is greatest when pore tips cover a large fraction of the interface and so this mechanism favors the formation of low-density material. The balance between these two competing effects determines the density of the film formed under a given set of anodizing conditions. As the current density is increased, the voltage drop across the interfacial impedance rises. In consequence, the minimization of this voltage drop becomes more important than the maximization of the image charge barrier lowering. The decrease in the porous film density when lower concentrations of hydrofluoric acid are used would be consistent with an increase in the interfacial impedance. The smaller a pore is, the greater the barrier lowering on that pore will be and hence the greater the current flow and the growth rate are. In the limit of low current density, this would favor the growth of pores with atomic dimensions rather than those observed. The lower limit to pore size may be determined by the thickness of the double layer in the electrolyte whose dimensions are expected to be similar to the smallest pores observed, i.e. a few nanometers, or by the requirement for the diffusion of the ions down the pores. Since the pore formation process is depth independent for tens of microns, the diffusion of reaction products down the pores is not a rate limiting process, so presumably this regime is never entered in practice.

For heavily doped silicon in hydrofluoric acid, the greatest voltage drop occurs in the interface region rather than in the bulk silicon region and so this interface region dominates the current-voltage characteristic. The increased doping has made the barrier sufficiently narrow for tunneling to occur. Current can pass freely across the Schottky barrier in both directions and the rectifying property disappears. The current density depends on the width of the barrier and tunneling becomes possible for barrier widths less than approximately 80 Å. At a pore tip, which may be considered as a hemisphere, the non-planar interface results in electric field enhancement with a consequent reduction in the depletion layer width. It can be shown that the depletion layer width decreases with increasing doping density, decreasing barrier height and decreasing tip radius. The presence of other nearby pores gives a further geometrical mechanism for forcing the current to flow through the pore tip. Due to the

overlap of the depletion regions of adjacent pores, charge carriers would have to tunnel a prohibitive distance if they came from anywhere other than the tip of a pore. The columnar structures observed are a consequence of this cooperative effect. If the depletion regions of two adjacent pore tips were to overlap, then the depletion layer thickness would increase so that the current density in that region would be reduced. The growth is therefore greater on the non-overlapping sides and the pores in effect repel one another. This repulsion, when combined with the overall tendency of the individual pores to grow in the direction of current flow, results in the type of columnar structure observed. Unlike the lightly doped case, the depletion region around each pore is predominantly due to that pore and not to cooperative effects with other pores. The tunneling current increases rapidly while the depletion layer width is reduced. The current flow is therefore concentrated at the extreme tip of the pore where, due to its small radius of curvature and the lack of interaction with the depletion regions of surrounding pores, the depletion width has a maximum. As the current density is increased, the voltage drop across the interface resistance rises and the area of the pore tip that is sufficiently forward biased to pass current increases. This results in the formation of larger pores. The use of lower hydrofluoric acid concentrations would be expected to increase the interfacial resistance and thus to encourage current flow over a larger area of the pore tip and so form wider pores, as observed. The authors give the general conditions under which a porous structure may be formed:

(1) The material is a semiconductor so that depletion layer widths are of suitable dimensions.

(2) The Fermi level of the semiconductor must be pinned near mid-gap at the semiconductor-electrolyte interface.

(3) The electrolyte must attack the semiconductor only when a current is passed.

(4) The electrochemical reaction products must be soluble in the electrolyte.

(5) The electrolyte must be capable of carrying the required current density.

One unresolved problem is that, although the Fermi level is probably pinned as indicated by the impedance data, it is also known that HF-treated silicon surfaces show one of the lowest known recombination velocities. If there is a high density of surface defects, one would expect these defects to provide an extremely high capture cross section for recombination; in contradiction to available data. In addition, pore formation also occurs in other semiconductors, GaAs and Ge, whose interfaces are not necessarily pinned. The authors give an explanation that may resolve this quandary.

The diffusion-limited model presented by Smith et al. [see *Smith1*, *Smith2*] is the second proposed theory. It assumes that the rate of porous silicon formation is diffusion limited by a necessary reactant from the bulk of the silicon to the growing pore. Since holes are known to be required in the anodic dissolution of silicon, they are strongly implicated as the required diffusion limited species. A characteristic diffusion length, which is a function of the dopant concentration, voltage, etc., controls the different pore morphologies. The essence of the pore structure is generally characterized by the intrinsic nature of the random walk and the magnitude of the diffusion length. In silicon, the step length of the random walk can be approximated by the mean free path of a hole. The diffusion length has physical significance as the characteristic diffusion length of a hole. As the particle (hole) randomly walks towards the growing pores, it is more likely to contact those pores that are nearest to it. This means that the outermost tips of the pores have the highest probability of hole capture and growth. The further into the pore labyrinth the particle diffuses, the higher the probability that it will encounter an active site is. This process produces a characteristic active zone, described by an average penetration depth, where the majority of the particles are trapped. The growing porous silicon film is typified by a leading active zone at the interface between porous silicon and bulk silicon where the structure of the porous film is determined leaving an inert or frozen region trailing behind it. This explains the stability of the porous structure once it is formed. However, it is within the active zone that the final structure of the porous silicon is ultimately determined. The random walk of the diffusing particle favors preferential tip growth in the active zone and it can be shown that the diffusion length favors a condition of continually branching pores until the inter-pore distance is approximately twice the diffusion length and so determines the general morphology of the porous silicon. The resulting interplay produces a porous structure of constant density and growth rate. It can be shown that when the step of the random walk doesn't change with decreasing the diffusion length, the silicon density decreases and the pores become increasingly more interconnected with the typical "tree" structure diminishing in favor of a random lattice of interconnected pores. In fact, the important parameter that determines the degree of pore interconnectedness is the ratio of the diffusion length to the average step length of the random walk. As this ratio approaches unity, the morphology of the porous silicon changes quickly from "tree'' to interconnected pores. Thus far is valid for the low current density regime. As the applied potential, and hence the current density, increases and/or the HF concentration decreases, the anodic dissolution of silicon passes from the pore formation regime to an electro polishing regime. Electro polishing is assumed to be a direct consequence of a passivating oxide formed within the

interior of the pores as the formation potential approaches a critical value. Because of the distribution of the field lines as a consequence of the pore geometry, the oxide formation will be most promoted at the tips. The oxide is a barrier for the incoming diffusing holes and its formation will tend to negate the geometric effects of increased tip growth probability. In this case, the dissolution still occurs generally at the interface between the pores and bulk silicon; just not directly at the pore tips. There is a transition regime between the onset of oxide formation and complete electro polishing. At the onset of oxide formation, the field density limits oxide formation to the extreme portions of the pore tips. This reduces the sticking probability only at the pore tip and increases the probability that growth will occur at the sides of the pores. As the pore diameter increases, the radius of curvature of the pore also increases so that the field lines at the pore tip decrease and less oxide is formed which, in turn, increases the sticking probability at the tip. This feedback between oxide formation and pore diameter results in a pore propagating with a characteristic diameter determined by the degree of oxide within the pore interior, which is a function of the formation voltage. As the formation potential approaches the electro polishing potential, the pore diameter approaches the spacing between pores. When the pore diameter is approximately equal to the inter-pore spacing, electro-polishing is favored. This model also takes into account the well-known fact that the {100} crystallographic planes of silicon are considerably more reactive towards dissolution than those of, for example, the {111} and are generally the crystal planes with the fastest dissolution rates. The theory predicts that the pore propagation should have a strong tendency to follow the crystal lattice rather than propagate parallel to the direction of current flow and it is therefore expected that the direction of pore propagation should demonstrate crystallographic selectivity. This is consistent with the experimentally observed facts. This model is capable of predicting the general morphologies obtained for different dopant types and concentrations, HF concentrations and current densities.

The validity of this model is verified by performing computer simulations to construct various porous silicon structures.

Both the Beal and the diffusion-limited models provide adequate explanation for porous silicon formation but posse seemingly divergent pore generation mechanisms. However, any differences between the two models are only apparent differences. In reality, a fundamental equivalence exists between the two models that arises naturally from a mathematical equivalence between the spatial electric and diffusion field distributions. Substitution of electric fields for diffusion fluxes and potential gradients for concentration gradients in any

electrostatic or diffusion phenomena generates an equivalent model in terms of its analogous counterpart.

Different authors have found the interface between porous silicon and bulk silicon to be depleted of holes during porous silicon formation. The model proposed by V. Lehmann et al. [see *Lehmann1*] also assigns the growth of pores to the fact that holes are necessary for the electrochemical dissolution and that they deplete in the walls between the pores due to an increased band gap. In order to understand the h^+ depletion mechanism responsible for micropore formation, one has to study the energy band structure of this material. This is visualized in fig. 2.3. This shows a sketch of the porous silicon/bulk silicon interface and corresponding band structure diagram. The increase in band gap energy is due to the size of the microporous structure. If the characteristic dimension of the remaining silicon approaches values as small as a few nanometers, the band-gap in this structure increases due to quantum confinement. When a hole (h^+) in the bulk silicon approaches the interface with the porous silicon, it needs additional energy to penetrate into the wall between two pores (broken arrows in fig. 2.3) whereas no additional energy is necessary to move to a pore tip (solid arrows). As a result, the pore walls will be depleted of holes (h^+) and will therefore become chemically inert whereas the dissolution reaction continues at the pore tips. This process is self-adjusting: a thick wall implies a low energy barrier for h^+, which allows h^+ entering the wall to initiate

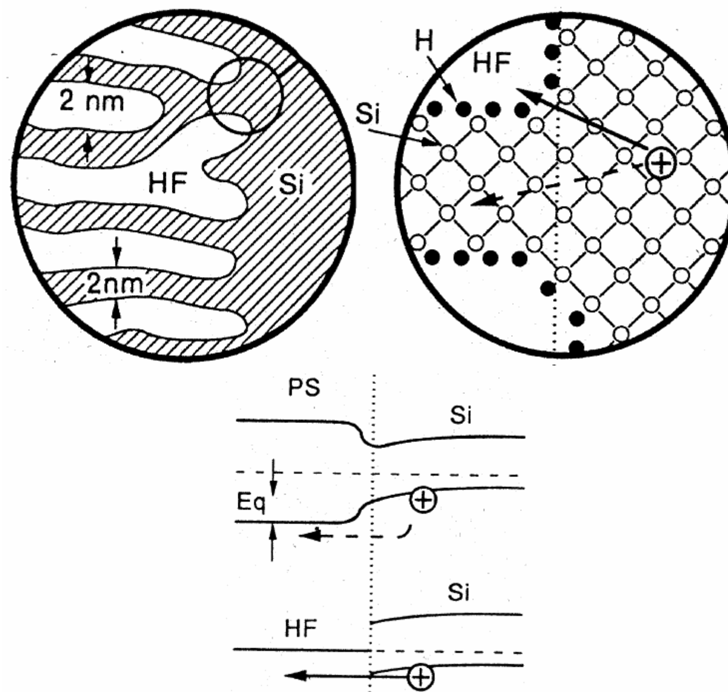

Fig.2.3: An enlarged cross-section of the PS-silicon interface and the corresponding band diagram [**after** *Lehmann2*].

further electrochemical dissolution.

The process of the thinning of the walls will continue until the band gap increases to a value at which h^+ can no longer enter the wall. The wall becomes depleted of h^+ and the dissolution stops. Applying a higher anodic bias to the substrate will increase the energy of the h^+ and therefore decrease the characteristic dimension of the remaining walls leading to the production of porous silicon with a larger band gap

A comprehensive model describing all aspects of pore formation, including selective crystallographic pore propagation, potential distributions, etc. does not yet exist.

References

1. *Uhlir* A. Uhlir, Bell System Tech. J. **35**, 333 (1956).
2. *Turner* D.R. Turner, J. Elektrochem. Soc. **105**, 402 (1958).
3. *Watanabe* Y. Watanabe, Y. Arita, A. Yokoyama and Y. Igarashi, J. Electrochem. Soc. **122**, 1351 (1975).
4. *Canham1* L.T. Canham, Appl. Phys. Lett. **57**, 1046 (1990).
5. *Lehmann1* V. Lehmann and U. Gösele, Appl. Phys. Lett., Vol.58, p.856(1991).
6. *Cullis* A.G. Cullis, L.T. Canham and P.D. Calcott, J. Appl. Phys., **82**, 909 (1997).
7. *Kozlowski* Fr. Kozlowski, Thesis (Dissertation), TU Munich (1996).
8. *Möller* Fr. Möller, Thesis (Dissertation), TU Munich (1996).
9. *Beal1* M.I.J. Beal, N.G. Chew, M.J. Uren, A.G. Cullis, and J.D. Benjamin, Appl. Phys. Lett. **46**, 86 (1985).
10. *Beal2* M.I.J. Beal, L.D. Benjamin, M.J. Uren, N.G. Chew and A.G. Cullis, J. Cryst. Growth **73**, 622 (1985).
11. *Smith1* R.L. Smith and S.D. Collins, J. Appl. Phys. **71**(8), R1 (1992).
12. *Pickering* C. Pickering, M.I.J. Beal, D.J. Robbins, P.J. Pearson, and R. Greef, J. Phys. C **17**, 6535 (1984).
13. *Smith2* R.L. Smith, S.-F. Chuang, and S.D. Collins, J. Electron. Mater. **17**, 533 (1988).
14. *Smith3* R.L. Smith and S.D. Collins, Phys. Rev. A **43**, 5409 (1989).
15. *Foll* H. Foll, Appl. Phys. A 53, 8 (1991).
16. *Lehmann2* V. Lehmann, B. Jobst, Th. Muschik, A. Kux and V. Petrova-Koch, Jpn. J. Appl. Phys. 32, 2095 (1993).

Chapter 3. THE THERMAL EFFUSION METHOD FOR POROUS SILICON INVESTIGATIONS

3.1. The Theory of thermal effusion

3.1.1. The adsorption and desorption concept

Adsorption is the result of electromagnetic in nature interaction between a solid and a gas. When one isolated atom or molecule is brought close to the surface of the solid, an interaction between the electrons of the particle and those of the solid occurs. Several aspects of adsorption phenomena can be distinguished if the charge transfers and the types of bond created are taken into account. If the electronic configuration of the adsorbing particle is only slightly changed by the process to the extent of inducing an overall dipole polarization, the interaction can be modeled as an attractive van der Waals-type potential acting on the adsorbate particle. Particles adsorbed by this mechanism are said to be physically adsorbed or **physisorbed**. When the solid is a metal, forces associated with the collectivization of the valence electrons of the adsorbed molecule and the metal exist and one can speak of **metal adsorption**. If there is a rearrangement of the electronic orbitals, possibly accompanied by charge transfer and the establishment of bonding orbitals between the adsorbate and the solid, one speaks of chemical adsorption, **chemisorption**. The type of interaction for chemisorption usually displays a monolayer character, which can be likened to a chemical reaction. Under real conditions, each of these forces contributes to some extent to making up the binding energy of adsorption of an adsorbed particle on an adsorbent. The interaction between an adsorbed particle and an adsorbent is usually presented in the form of a potential curve (fig.3.1.1-a), the potential energy of the system being calculated from its value at $x=\infty$. At $x = x_0$, the potential energy has a minimum, reflecting the fact that, at distances $x < x_0$, the forces of attraction between the particle and the surfaces become less than those of repulsion. The adsorbed particle in the potential well undergoes thermal vibrations along the x-axis about the equilibrium position at $x = x_0$. The depth of the potential well is equal to the energy E', which should become liberated as a result of the adsorption of each particle. Conversely, in order for the particle to be desorbed, i.e. the adsorption bond between the adsorbent and the particle to be broken, the system should transfer energy equal to or greater than E' to the hitherto adsorbed particle. The number of adsorption centers per unit surface

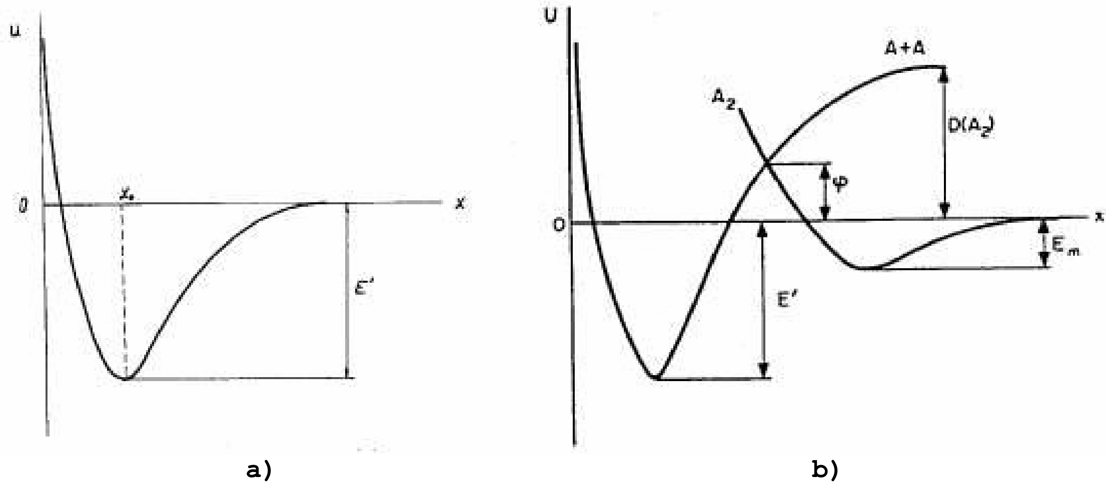

a) b)

Fig.3.1.1: Potential energy U(x) a) of adsorbent-adsorbed particle system and b) of diatomic molecule transferring to chemisorbed state with dissociation into atoms vs. separation x [**after** *Ageev*].

area is always finite, in the case of chemisorption it is usually of the order of the adsorbent atoms surface concentration. The concentration of the adsorption centers may be different for different adsorbates with the same adsorbent. One may introduce the concept of the adsorption capacity of an adsorbent, understanding by this the maximum possible concentration, n_{max}, of adsorbed particles on the surface of a given adsorbent for that a given adsorbate. One may apply the concept of a monolayer to the adsorbate concentration n_{max}, by which one means the most closely packed arrangement of adsorbed particles on the adsorbent surface residing in the same state of adsorption bonding. When the surface of a homogeneous adsorbent is uniformly filled by the adsorbate, the states of the adsorbed particles are indistinguishable from one another. With increasing particle concentration n, or degree of surface coverage $\theta = n/n_{max}$, the average separation between neighbouring particles decreases. This may bring about the appearance of an interaction between the particles, which is dependent on the magnitude of θ. In some cases, chemisorption of particles proceeds in accordance with not one, but rather two or even a larger number of states of adsorption bonding between the adsorbate and the adsorbent; the filling of these states being possible both consecutively and simultaneously. In other words, the monolayer corresponding to saturation of the adsorption bonds of the adsorbent can be separated into several sublayers of adsorbed particles, each with its characteristic heat of adsorption E'. In many cases, chemisorption is accompanied by a dissociation of the molecules in which bonds of the adsorbed molecule are destroyed by the action of the adsorbent. In this process, saturated molecules, which do not have free valence bonds, are first adsorbed in a weakly bound state (prestate) of physical adsorption from which they transfer by dissociation into a chemisorption state with strong coupling. The potential curve for this case is presented

schematically in (fig.3.1.1-b). This illustrates a diatomic molecule built up from identical atoms. For the molecule A_2 to become chemisorbed with dissociation directly from the gas phase, or via an intermediate stage of physical adsorption, its energy should be sufficient to surmount the activation barrier of height φ.

Accordingly, the activation energy E_d of desorption of the molecule A_2 will be the sum of the heat of adsorption E' and φ, i.e. $E_d = E' + \varphi$. In the case of $\varphi > 0$, we have activated adsorption. The energy necessary to desorb a particle from the adsorbate can either come from the solid or from some external source. The latter, lasers or other sources of electromagnetic radiation, have been used in photodesorption and phonon stimulated desorption. Likewise, electron and ion beams are employed to cause electron and ion stimulated desorption respectively. Strong electric fields at field emission tips cause field desorption and field evaporation, sometimes used in conjunction with lasers or electrons to produce photon- and electron-stimulated field desorption.

3.1.2. Thermal desorption

Thermal desorption takes place if the solid itself acts as the reservoir from which the desorption energy is taken. Lennard-Jones and Devonshire [see *Lennard1*, *Lennard2*] argued that the thermal motion of the lattice should act as a time-dependent perturbation on the surface potential with which the adsorbate is bound to the solid and can hence supply the desorption energy. This picture (so-called phonon-mediated desorption) is appropriate and sufficient for physisorption, in which the kinetics is much simpler than that of chemisorption. For the latter, additional questions concerning energy transfer between the electronic degrees of freedom for the solid and the adsorbate are still largely unanswered. Thermal desorption mass spectrometry (TDS) is one of the most commonly used techniques in gas-surface interaction investigations and has been widely used to study the kinetics of the desorption of chemisorbed gases from the surface of refractory metals. In a thermal desorption experiment, after a rigorous cleaning of the sample in vacuum, a known gas is introduced at a constant input rate and allowed to adsorb on the surface of the solid substrate. The gas is then desorbed by increasing the temperature of the sample while the change of partial pressure within the system is detected mass-spectrometrically and recorded. The resulting pressure-time curve is referred to as a "desorption spectrum". It is assumed that the desorption rate is proportional to the change in pressure with time. Initially, the method had employed [see *Apker, Becker, Ehrlich*] a high rate of heating $\left(\sim 10^3\ \mathrm{Ks}^{-1}\right)$; so-called flash desorption. Redhead [see

Redhead1] has carried out temperature-programmed desorption at very much slower rates of heating. This simple change in experimental procedure has led to an increase in the resolution of the method and to the discovery of additional binding states unresolved by rapid flash desorption. If the temperature-time relation for the heating of the sample is suitably controlled, the desorption spectra can be analysed to yield information on various adsorption parameters. There are four important kinetic parameters which may be determined by a thermal desorption experiment:

(1) the kinetic order of the desorption reaction,
(2) the activation energy of desorption in the various phases,
(3) the pre-exponential factor of the desorption rate coefficient and
(4) the number of the various desorbing phases and the population of the individual phases.

A variety of methods are available for deducing values for these parameters from the experimental data. The first methods for analyzing the desorption spectra have been described by Smith [see *Smith*] and Erlich [see *Ehrlich*]. Redhead [see *Redhead2*] was the first to show how the various adsorption parameters may be derived from the curve of desorption rate as a function of a sample temperature for two heating schedules which, especially the first, are preferably used in practice: a linear variation of sample temperature with time $\left(T = T_0 + \beta t\right)$, and a reciprocal variation $\left(1/T = 1/T_0 - \alpha t\right)$.

The process has been viewed as a system into which gas is being leaked at a constant rate $L\ [\text{molecules/second}]$ and being pumped away at a constant speed $S\ [\text{l/sec}]$. At equilibrium, when adsorption on the sample has ceased, $p \equiv p_{eq}$ and

$$L = KS_{eq} \tag{3.1.1}$$

where $K = 3.27x10^{19}$ molecules/l at $p = 1\,\text{Torr}$, and $T = 295\,\text{K}$. If, during the desorption cycle, it is be assumed that no adsorption occurs, then a mass balance in the flow system yields:

$$AR(t) + L = KSp + KVdp/dt \tag{3.1.2}$$

where A is the sample area $\left[\text{cm}^2\right]$, R is the desorption rate $\left[\text{molecules/cm}^2\text{sec}\right]$ and V is the volume of the system $[\text{l}]$. For chemisorbed gases, re-adsorption depends on the population of the various adsorbed phases, the pumping speed, and the time duration of the desorption cycle. The amount of re-adsorption is usually trivial unless the pumping speed is very low and the desorption cycle is long. Adsorption on the walls of the system has also been ignored.

With a glass system at room temperature, adsorption on the walls is, however, significant for hydrogen and carbon monoxide.

Combining (3.1.1) and (3.1.2) and putting $p^* = p - p_{eq}$, we obtain

$$dp^*/dt + p^*/\tau = aR(t) \qquad (3.1.3)$$

where $a = A/KV$ and $\tau = V/S$ is the characteristic pumping time. From the last equation, it can be seen that for small pumping speeds $(\tau \to \infty)$ the desorption rate is proportional to the first derivative of pressure with time. This condition can be approximated in practice when the duration of the desorption sweep is made short compared with the characteristic pumping time. With chemically active gases, this condition can be approached with very fast sweep rates $(> 10^3\ \text{K/sec})$. Alternatively, for very high pumping speeds $(\tau \to 0)$ we see that $p^* \to a\tau R(t)$, thus the desorption rate is proportional to the pressure. Chan and Weinberg [see *Chan1*] have investigated and demonstrated the importance of the combined effect of heating rate and pumping speed in thermal desorption mass spectrometry experiments. Thereby to assess the “goodness” of the kinetic parameters, the magnitudes of both above-mentioned parameters should be accurately measured and reported if the values of these parameters have to be compared with already published values. They have shown that in order to obtain a pressure profile during a desorption measurement which is proportional to the desorption rate, the reciprocal of the product (dimensionless) of heating rate and pumping time constant must be large; greater than approximately 0.5. Thus, the distortions of the peak shape and the peak position in thermal desorption spectra can be minimized.

3.1.3. Polanyi-Wigner equation

The simplest phenomenological description of desorption possible is by applying an exponential temperature dependence of the desorption rate, R. If it is assumed that this rate is proportional to the number of the desorption capable objects, the following differential equation (Polanyi-Wigner or Frenkel-Arrhenius) can be written for the rate of desorption:

$$R(t) = -dn/dt = \nu_0^{(m)} n^m \exp(-E_d/kT_s) \qquad (3.1.4)$$

where:

$R(t)$ is the rate of desorption, which is a function of time, presents the flux density of desorbing particles and equals the rate of decrease of the particle concentration n on the surface,

T_s is the temperature of the substrate,

n is the two-dimensional molecular concentration $\left[\text{molecules/cm}^2\right]$ of the surface coverage,

$\nu_0^{(m)}$ is the pre-exponential factor $\left[s^{-1}\right]$ associated with the change in the character of particle motion as particles transfer from the adsorbed to the free state and is of the order of the magnitude of the frequency of vibration of the adsorbed molecule,

m is the order of the desorption reaction,

k is the Boltzmann constant, and

E_d is the activation energy of desorption $[\text{cal/mole}]$.

In a classical picture, ν_0 can be interpreted as a frequency with which the adsorbed particle tries to escape from the adsorption well and, in the general case, depends on the coverage θ and the temperature T. Particles can become desorbed both in the form in which they resided on the surface and after their association in molecular complexes (associative desorption). In the first case, $m = 1$ (the desorption kinetics is first order) and E_d equals the binding energy of the particles, while in the case of desorption being preceded by the formation of a diatomic molecule from two identical atoms, $m = 2$ (second order kinetics) and E_d correspond to the activation energy of desorption. Similarly to the pre-exponential factor, in the general case, E_d is coverage and temperature dependent. This differential equation contains all the kinetic desorption parameters $\left(\nu_0^{(m)}, E_d, \text{and } m\right)$ which have to be determined.

If there are multiple states on a given plane, then:

$$R(t) = \sum_i dn_i/dt. \tag{3.1.5}$$

If the thermal desorption spectra are measured by increasing the substrate temperature linearly with time, then the relationship between substrate temperature and time is given by

$$T_s = T_{s0} + \beta t, \tag{3.1.6}$$

where T_{s0} is the initial temperature of the substrate, and β is the heating rate, i.e. dT_s/dt.

Equations (3.1.4) and (3.1.6) may be combined to yield

$$R(T_s) = -\beta dn/dT_s = \nu_0^{(m)} n^m \exp\left(-E_d/kT_s\right). \tag{3.1.7}$$

3.1.4. Extraction of the desorption parameters

Many methods have been developed for the extraction of desorption parameters. Since the aim of this work is not to compile a comprehensive list, we shall mention only few of them.

Assuming E_d is constant with respect to time and temperature and the substrate temperature (T_s) is uniform, Redhead [see *Redhead2*] has suggested the following procedure. Equation (3.1.7) can be solved to find the temperature T_M at which the desorption rate has a maximum, then

$$E_d/kT_M^2 = \left(\nu_0^{(1)}/\beta\right)\exp\left(-E_d/kT_M\right) \qquad \text{for } m = 1 \qquad (3.1.8)$$

and

$$E_d/kT_M^2 = \left(\nu_0^{(2)}n_0/\beta\right)\exp\left(-E_d/kT_M\right) \qquad \text{for } m = 2\,. \qquad (3.1.9)$$

where n_0 is the initial surface coverage.

Equation (3.1.8) shows that T_M is coverage independent for a first-order reaction with constant E_d. Thus, E_d can be found directly from the measurement of T_M provided a value of $\nu_0^{(1)}$ is assumed. Often for first order desorption kinetics, the pre-exponential factor has been assumed to be $10^{13}\ s^{-1}$. However, using an assumed value for the pre-exponential factor may result in a considerable error in E_d determination. Another possibility is to determine the activation energy by varying β and plotting $\log T_M$ against $\log\beta$. E_d can then be obtained from the relation,

$$2 + E_d/kT_M = d(\ln\beta)/d(\ln T_M). \qquad (3.1.10)$$

Therefore, the rate constant can be found by substituting E_d in equation (3.1.8). For reasonable accuracy, β must be varied by at least two orders of magnitude.

For the second-order case, it can be seen from equation (3.1.9) that T_M now depends on the surface coverage. n_0 may be found from the area under the desorption rate curve as a function of time. A plot of $\ln\left(n_0T_M^2\right)$ versus $1/T_M$ must be constructed and the value of E_d/k determined from the slope of the straight line. $\nu_0^{(2)}$ can then be found by substitution in equation (3.1.9).

Thus, the desorption reaction order can be determined from the behavior of the desorption rate curve maximum with coverage. A first order reaction with a fixed activation energy of desorption gives rise to a peak in the desorption rate curve which does not change in temperature with coverage. If the temperature of the peak decreases with increasing coverage, the reaction may be second-order with fixed activation energy or first order with energy that depends on coverage. These two cases can be distinguished by plotting $\ln\left(n_0T_M^2\right)$ against $1/T_M$. A second-order reaction with fixed activation energy yields a straight line.

The shape of the experimental desorption rate curve as a function of the sample temperature can be used to determine the order of the desorption reaction and to answer the question of whether the activation energy is constant or, alternatively, a function of surface coverage. It can be shown that, for the first order case, an equation describing the shape of the desorption rate curve, which is asymmetric about the maximum at T_M, is valid. Similarly, for the second-order case, it can be shown that when $(T/T_M)^2 \to 1$, the desorption rate curve is symmetric about the maximum. Fig.3.1.2 shows theoretically calculated thermal desorption spectra obtained by solving eq. (3.1.7) for the case of first- and second-order kinetics, respectively. It is evident from fig. (3.1.2-a) that for first-order desorption kinetics, the temperature at which the maximum rate of desorption occurs is invariant with surface coverage. Fig. (3.1.2-b) shows that for the second-order desorption kinetics, the temperature at which the maximum rate of desorption occurs shifts to lower values as surface coverage increases. This method of thermal desorption spectra analysis has been extensively used by workers in this field but it has its own drawbacks. The varying of β by several orders of magnitude is not always possible for the case of desorption from the surfaces of bulk single crystals that is of interest. If β is very small, wall or re-adsorption effects may be important. Alternatively, β may not be too large due to limitations in heating massive single crystals. Even if β could be made very large, then multiple peaks might not be resolved. When the plot

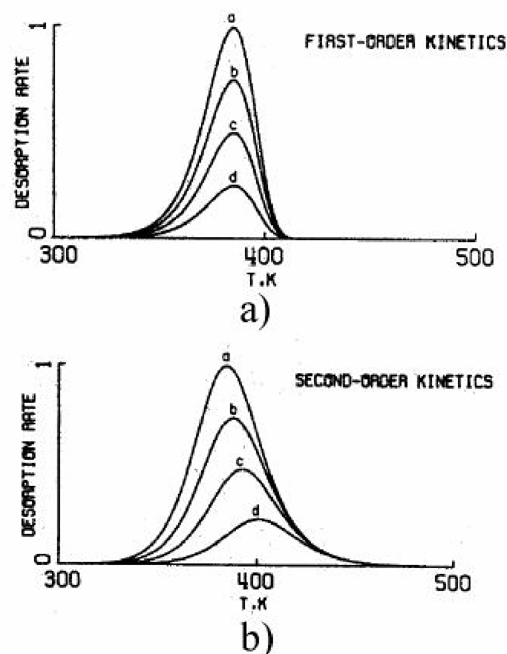

Fig.3.1.2: Calculated dimensionless desorption rate at different fractional surface coverages (a: Θ=1.0; b: Θ=0.75; C: Θ=0.5; d: Θ=0.25) for a) first-order and b) second-order desorption kinetics [after *Chan2*].

of $\ln\beta$ versus $\ln T_M$ is not linear, the application of eq. (3.1.10) to determine an accurate value of E_d is difficult.

Lord and Kittelberger (1974) [see *Lord*] have proposed an extension of the Redhead's method by means of which it is possible to find the maximum desorption rate temperature T_M and the initial surface coverage n_0 in order to determine the activation energy E_d and the pre-exponential factor regardless of the kinetic order. Kornelsen and O'Hara (1974) [see *Kornelsen*] have used a computer graphics procedure allowing the experimental thermal-desorption spectra to be matched visually with the sum of up to twelve theoretical first-order desorption peaks, but at constant ν_0 and E_d. Falconer and Madix (1975) [see *Falconer*] have suggested two methods for determining the activation energy E_d without making assumptions about pre-exponential factors, reaction orders or specific reaction mechanisms. One method employs a relationship for the shift in peak temperature with change in heating rate while the other utilizes the change in peak amplitude with shift in peak temperature for different heating rates. Edwards (1976) [see *Edwards*] has given expressions for the peak widths of first and second order desorption transients determined in terms of the parameters of the desorption equation. These expressions permit an accurate estimate of the activation energy of desorption, E_d, from the peak width and peak temperature obtained from a single desorption transient for situations in which the desorption energy and pre-exponential factor are independent of both temperature and coverage. King (1977) [see *King*] has proposed a model, which assumes that a molecule approaching a surface is initially adsorbed into a mobile second layer in which migration can occur until an empty site is found. The influence of this intermediate state on desorption kinetics is illustrated through computed desorption spectra; the major features being a broadening of the desorption peak and a shift towards higher peak temperature. It is shown that lineshape analysis of desorption spectra made by ignoring the role of the intermediate state can lead to very large errors in the derived values for both desorption energies and rate constant pre-exponentials. Soler and Garcia (1983) [see *Soler*] have simulated diverse effects on the first order desorption curves by changing the dependence of ν and E_d on θ and T and predict which ones could be distinguished and which could not. Forzatti et al. (1984) [see *Forzatti*] have presented a new method for analysing normalized thermal desorption spectra with respect to the maximum point of the desorption curve from heterogeneous surfaces. The method provides the coverage dependence of the desorption activation energy and of the frequency factor ν and, by iteration, the correct kinetic order can be obtained. Miller et al. (1987) [see *Miller*] have given a classification of

the procedures for a kinetic desorption parameter determination. They can be divided into two groups:

(1) the integral approach, which relates the kinetic parameters to bulk peak characteristics such as half-widths and temperatures at peak maxima. It is well known that this strategy is useful only in cases where the parameters are not coverage dependent;

(2) differential analyses, where desorption rate/temperature pairs taken from one or more TPD spectra are used to prepare an Arrhenius plot whose slope and intercept are related to E_d and ν_0.

While the integral techniques are almost always used to extract the coverage-independent kinetic parameters, the differential techniques may, in favorable situations, be applied to obtain reliable coverage-dependent kinetic parameters. The authors contrast the integral and differential approaches to kinetic analysis of TPD experiments, emphasizing the inherent assumptions, which limit the applicability of each. Pavlovska et al. (1988) [see *Pavlovska*] make a comparative study of the possibilities and limitations of desorption methods. Tronconi and Lietti (1988) [see *Tronconi*] present another method which relates the position and the area in normalized coordinates of a single temperature-programmed desorption peak to the characteristic parameters of desorption kinetics. The method applies to TPD from homogeneous surfaces (i.e. with coverage-independent kinetic parameters), and handles both the limiting cases of negligible re-adsorption and of re-adsorption equilibrium. It requires a single TPD curve; its derivation involves no approximations and can be applied for any kinetic order.

Chan et al. (1978) [see *Chan2*] present one approach, which is representative of the integral techniques for a kinetic desorption parameter determination. The method uses the spectral peak widths and the temperature at which the maximum rate of desorption occurs to describe both first- and second-order desorption kinetics. The mathematical apparatus of this method is explicitly described in the considered article so need not be detailed here. This approach needs the subsidiary dimensionless quantities by means of which eq. (3.1.7) may also be rendered dimensionless to be introduced. One part of dimensionless quantities such as E_M (see below) and θ_0, the fractional surface coverage at the initial temperature, are determined from experimental thermal desorption mass spectra. E_M is defined as $E_M \equiv E/Z_M$, where Z_M is the dimensionless temperature at the maximum rate of desorption, $E \equiv E_d/kT^*$ and $T^* \equiv 1\,K$. It can be shown that in order to determine the pre-exponential factor of the desorption rate coefficient $\nu_0^{(m)}$ for first-order desorption kinetics, E_M must be

known while for second order kinetics, both E_M and θ_0 must be known. For the determination of E_M, experimentally measurable quantities such as peak widths at one-half and three-quarters the peak maximum (the half-width and ¾-width, respectively) are chosen. These can be determined easily and accurately.

The width of a peak is defined as $\Delta W \equiv Z' - Z''$ (in terms of the dimensionless temperature Z), where $Z' = Z_M(1+\zeta)$, $Z'' = Z_M(1-\zeta)$ and $\zeta > 0$. Using an expansion in a Taylor series about Z_M of the dimensionless desorption rate and defining $Y \equiv \Delta W / Z_M$, one comes to the following expressions for E_M :

- for first-order desorption kinetics,

$$E_M = -1 + \frac{\sqrt{Y_{1/2}^2 + 5.832}}{Y_{1/2}} \quad \text{and} \quad E_M = -1 + \frac{\sqrt{Y_{3/4}^2 + 2.353}}{Y_{3/4}}, \tag{3.1.11}$$

- for second-order desorption kinetics,

$$E_M = 2\left[-1 + \frac{\sqrt{Y_{1/2}^2 + 3.117}}{Y_{1/2}}\right] \quad \text{and} \quad E_M = 2\left[-1 + \frac{\sqrt{Y_{3/4}^2 + 1.209}}{Y_{3/4}}\right]. \tag{3.1.12}$$

These expressions include a correction, which reflects the fact that the expansion of the dimensionless desorption rate in a Taylor series is valid only for rather small values of $|Z - Z_M|$ or ($\zeta << 1$), which is not the case for the points determining the half- and the $3/4$-width generally.

It is known (see fig.3.1.2) that second-order desorption spectra are approximately symmetrical about the peak maxima, whereas first-order desorption spectra are asymmetric. This statement can be quantified by defining the skewness parameter:

$$\chi \equiv \left[\frac{(Z' + Z'' - 2Z_M)}{\Delta W}\right] x100 . \tag{3.1.13}$$

The peak is symmetrical about the peak maximum when $\chi = 0$. It is skewed toward high temperatures or low temperatures for $\chi > 0$ or $\chi < 0$, respectively. The authors give the following calculated values for χ over the range of $10 < E_d < 50$ kcal/mol (corresponding to $5.033 \le E \le 25.164$) and $10^8 \le \nu_0 \le 10^{15}$

-at half the peak maxima, χ varies in the interval

$-15.5 \div -17.6$ for first-order desorption kinetics, and

$3.2 \div 5.1$ for second-order desorption kinetics,

-at three-fourths the peak maxima

$-10 \div -11$ for first-order desorption kinetics, and

2 ÷ 3 for second-order desorption kinetics.

Eq. (3.1.13) may be used as a supplementary test to determine the order of the desorption kinetics.

References

1. *Ageev* V.N. Ageev and N.I. Ionov, Studies of Adsorption
2. *Lennard1* J.E. Lennard-Jones, A.F. Devonshire, Nature **137**, 1069 (1936).
3. *Lennard2* J.E. Lennard-Jones, A.F. Devonshire, Proc.R.Soc.Lond. A **158**, 242 (1937).
4. *Apker* L. Apker, Ind. Eng. Chem. **40**, 846 (1948).
5. *Becker* J.A. Becker and C.D. Hartman, J. Phys. Chem. **57**, 158 (1953).
6. *Ehrlich* G. Ehrlich, J. Appl. Phys. **32**, 4 (1961).
7. *Redhead1* P.A. Redhead, Trans. Faraday Soc. **57**, 641 (1961).
8. *Smith* A.W. Smith and S. Aranoff, J. Phys. Chem. **62**, 684 (1958).
9. *Redhead2* P.A. Redhead, Vacuum **12**, 203 (1962).
10. *Chan1* C.M. Chan and W.H. Weinberg, Appl. Surf. Sci. **1**, 377 (1978).
11. *Chan2* C.-M. Chan, R. Aris and W.H. Weinberg, Appl. Surf. Sci. **1**, 360 (1978).
12. *Lord* Frances M. Lord and J.S. Kittelberger, Surf. Sci. **43**, 173 (1974).
13. *Kornelsen* E.V. Kornelsen and D.H. O'Hara, J. Vac. Sci. Technol. **11**, No.5 Sept/Oct., 885 (1974).
14. *Falconer* J.L. Falconer and R.J. Madix, Surf. Sci. **48**, 393 (1975).
15. *Edwards* D. Edwards,Jr., Surf. Sci. **54**, 1 (1976).
16. *King* David A. King, Surf. Sci. **64**, 43 (1977).
17. *Soler* J.M. Soler and N. Garcia, Surf. Sci. **124**, 563 (1983).
18. *Forzatti* Pio Forzatti, Massimo Borghesi, Italo Pasquon and Enrico Tronconi, Surf. Sci. **137**, 595 (1984).
19. *Miller* J.B. Miller, H.R. Siddiqui, S.M. Gates, J.N. Russel,Jr., J.C. Tully and M.J. Cardillo, J. Chem. Phys. **87** (11), 6725 (1987).
20. *Pavlovska* A. Pavlovska, H. Steffen and E. Bauer, Surf. Sci. **195**, 207 (1988).
21. *Tronconi* Enrico Tronconi and Luca Lietti, Surf. Sci. **199**, 43 (1988).

3.2. Experimental equipment for effusion measurements

3.2.1. Description of the apparatus

A scheme of the experimental equipment is represented in fig.3.2.1. It has to be mentioned that the components of the measuring volume consist exclusively of ultra-high vacuum

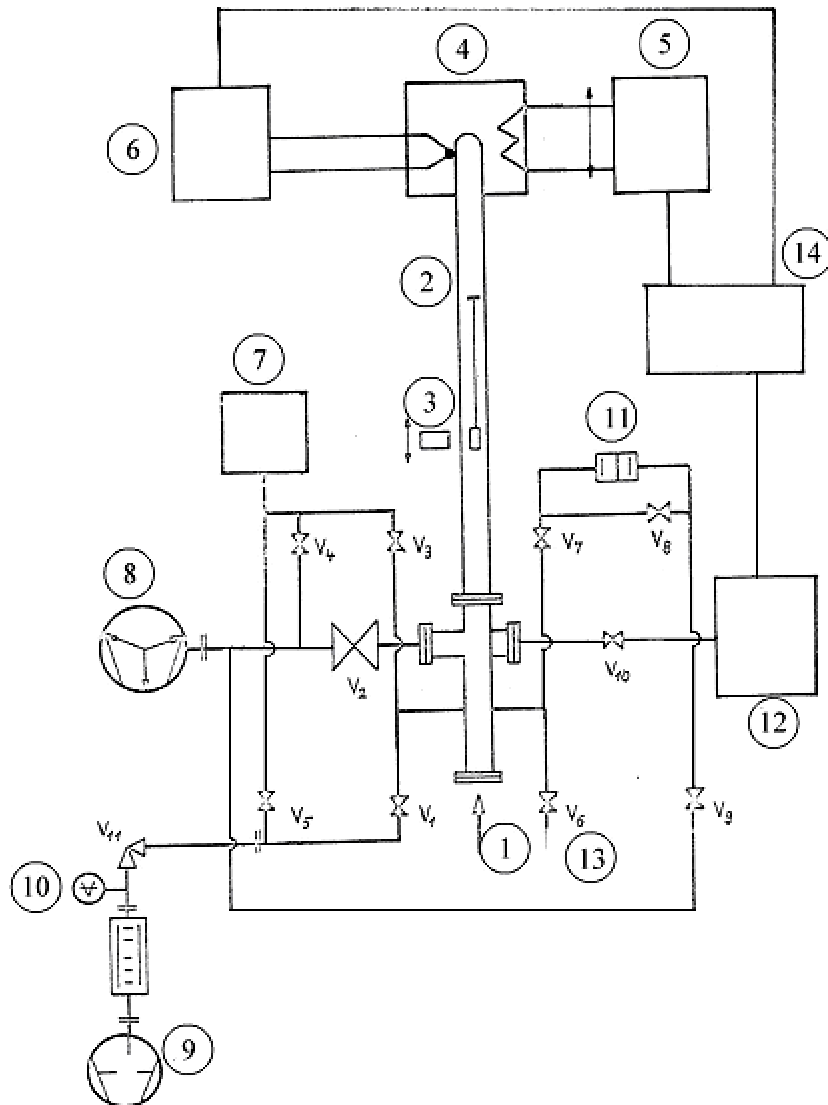

1. **1.** Sample supply (application)
2. **2.** Extraction volume
3. **3.** Magnetic manipulators
4. **4.** Extraction oven
5. **5.** Heat controller
6. **6.** Temperature measuring instrument for thermocouples
7. **7.** Measuring volume
8. **8.** Ion-getter pump with pressure indication (pressure gauge)
9. **9.** Rotary pump with molecular sieve
10. **10.** Pre-vacuum gauge (measuring cell)
11. **11.** Capacitive pressure gauge (capacitive manometer)
12. **12.** Mass-spectrometer
13. **13.** Ventilating system (N_2, Ar)
14. **14.** Computer

$V_1 \div V_{10}$ - UHV-stop valves

V_{11} - stop valve

Fig.3.2.1: Sketch of the thermal effusion setup

structural elements. The extraction recipient is of quartz. The quartz tube **2** is connected to the metal by a cascade of passage glasses. The measuring volume **7** is evacuated by a two-step rotational (rotary) pump via a molecular sieve **9** up to a coarse vacuum of $4x10^{-3}$ Torr. The ultra-high end-vacuum of $10^{-9} \div 10^{-8}$ Torr is then attained by use of a 20 l/sec ion-getter pump **8**. The operational principle of these pumps is based on the production of ionized gas particles (atomic or molecular ions) in an electrical field of some kV applied between two electrodes. The anode consists of a large number of closely packed high-grade steel cylinders aligned along parallel axes. Perpendicular to the cylinder axes, two cathodes are formed from metal plates placed parallel to each other at each end of the cylinders. A strong homogeneous magnetic field is also applied parallel to the axes of the cylinders. Ionized gas-particles are accelerated by the electrical field and bombard the cathodes. These penetrate the metal surface and are captured in the crystal lattice. Metal atoms are ejected from the cathodes by the bombardment. These atoms take a seat on the other electrodes places to form a metal layer, which acts as a getter and binds neutral and ionized gas particles. Electrons, which penetrate into or are liberated within the interior of a cylinder, cannot leave. Because of the electrical field distribution at each end of the cylinders, such an electron swings between these ends. The existence of a radial component to the electron's velocity perpendicular to the strong magnetic field causes the electron to assume a spiral motion with an enhanced path length and consequently an increased number of ionizing 'pushes'. The positive ions created are much less deflected by the magnetic field. They leave the cylinder and bombard the cathodes. The above-described process enables pressures lower than 10^{-10} Torr to be reached.

It has to be mentioned that the ion-getter pump exhaustion rates differ for the various gases that may be present. For air, N_2, CO_2 and H_2O, the exhaust rates are practically the same. The air-exhaust rate is taken as a standard. The exhaust rates for a selection of gases relative to air are given in table 3.2.1. It is important to know when a mixture of gases is

Type of gas	**Exhausting rate relative to the air exhausting rate [%]**
H_2	200
D_2	190
CH_4	150
Light hydrocarbons	90-160
O_2	60

Tab.3.2.1: Exhausting rates of some gases relative to the exhausting rate of air [after *Balzers*].

present in the extraction volume, which is evacuated, and to simultaneously take mass-spectrometer measurements. If one is interested in a determination of the ratio of the corresponding partial pressures, the above-mentioned specific exhaust rates have to be taken into account.

The presence of pipes and valves, with their corresponding stream resistivities, between the pump and the extraction volume causes an effective reduction of the pumping speed, in our case to $3\ \text{l/sec}$.

All valves are metallic to allow for heating.

The resistively heated extraction oven creates a temperature field whose longitudinal function has a plateau necessary for the homogeneity of the heating. The oven **4** is movable - on rails - to enable the sample to be placed within this plateau. The sample is shifted along the quartz tube by means of two magnetic manipulators **3** – one inside and another outside the tube. These enable the position of the sample to be changed without opening the evacuated tube. It is also possible for a number of samples to be charged together within the extraction tube and then measured successively by means of sequential insertion into and removal from the active plateau region of the oven of the desired sample.

Eurotherm controller **5** regulates the temperature field in the extraction oven**.** This gauge offers the possibility of establishing different temperature regimes, including temperature ramping, to be used. Additionally, computer control is available.

The temperature of the sample is obtained by means of a Ni-Cr thermocouple placed as close as possible to the sample outside the quartz tube. The thermocouple is connected to a temperature-measuring instrument **6**, which interprets the thermo-voltage generated, and displays it as a temperature. The measuring instrument also communicates with the computer.

The measuring volume **7** has an exactly determined value of $834\ \text{cm}^3$.

The capacitive manometer **11** shows the pressure within the measured volume. It works on the principle of reading the deformation of a membrane placed between two distinct volumes. Within the first volume, the pressure is equal to that of the vacuum attained before the onset of effusion. Within the second volume, the pressure is enhanced as a result of the performed effusion. The curvature of the membrane is in the direction of the lower pressure and causes a change in the capacitance between the membrane and a fixed electrode. The magnitude of the signal is proportional to this curvature and is converted into pressure units.

For measuring the partial pressures created by the components of the gas mixture after effusion, a quadrupole mass-spectrometer QMG 111 **12** is used. This spectrometer operates on the principle of mass-separation by oscillation of the ions within a high-frequency

quadrupole field. The atoms or molecules of the investigated gas are ionized by ‘pushes’ with electrons. The ions created this way are accelerated, pass through a system of rods and are collected in a Faraday-collector. The resulting collector-current is proportional to the partial pressures of the gas mixture components and, by means of a current-voltage converter, is transformed into the final measured signal. The mass-separation is accomplished by a system of four cylindrical rod-electrodes. The opposite rods are electrically connected and a voltage $U + V\cos\omega t$ is applied to both rod pairs. This voltage causes a vibration of the ions passing through the quadrupole. The ratio $U/V = \lambda$ is constant during the measurement. The following equation is valid for each ion in the quadrupole field:

$$\frac{m}{e} = \lambda \frac{V}{\omega^2}$$

where m is the mass and e the electrical charge of the ion. Only those ions whose masses and charge fulfill the filter condition can pass through the quadrupole and reach the collector. Other ions vibrate unstably, land on the surface of the rods where they are charge neutralized and are filtered out. By changing the ratio U/V, it is possible for different masses (or ratios m/e) to be measured.

Because of the proportionality between m (or m/e) and V, if the latter is being uniformly changed, a linear run through all masses (mass spectrum) can be seen. The graphics of the function of the ion current versus V shows characteristic peaks, which can be assigned to determined masses (m/e) unambiguously.

The resolution R of the mass-spectrometer is presented by the ratio of the mass m and one interval Δm of the mass scale expressed in mass units $(R = m/\Delta m)$. This interval Δm is the distance between two neighboring peaks of the mass spectrum with the same height. The depth of the valley between them amounts up to max. $x\%$ (depending on the convention - e.g. 10%) of the peak height.

The sensitivity E of the mass-spectrometer is presented by the ratio of the ion-current I_+ measured in the collector (I_+ in ampere) to the partial pressure p of the determined gas component (p in Torr) when the electron component of the current is given:

$$E = \frac{I_+}{p} \ [\text{A/Torr}].$$

The ion-current I_+ created is directly proportional to the partial pressure of the corresponding gas component at a sufficiently low working pressure within the quadrupole. The partial pressure is given by:

$$p = \frac{I_+}{E} \; [\mathrm{Torr}].$$

Two factors contribute to the sensitivity of the mass spectrometer – the sensitivity of the ion source and the transmitting capacity of the system for mass-separation (the system of rods). Because of the different ionization energies of the particular gasses, the sensitivity E of the mass-spectrometer is normally given for nitrogen or argon. For this reason, the determination of the absolute partial pressure of a certain gas, whose relative ionization probability with respect to that of nitrogen is unknown, could be determined by means of an absolute calibration measurement with the same gas used as a test gas. In tab.3.2.2, the relative ionization probabilities of some of the gases most often created by effusion are given. The ion-source sensitivity and the mass-separation transmission capacity have to be considered together as the transmission capacity depends on the entrance conditions of the ions into the mass-separation system. For an ion source of relatively low sensitivity, it is permissible for the transmission capacity to be high if the ions enter the mass-separating system on favorable terms and this can result in a very high sensitivity for the whole system. In table 3.2.3 are listed the sensitivities of the mass-spectrometer for some gases often appearing at the effusion.

Two types of measurements are possible using the mass-spectrometer. The first is when the instrument is tuned to measure the effusion velocity of a certain gas at a constant temperature or as the temperature is ramped. The second is a relatively rapid run over all masses at equidistant temperatures. In this latter case, one can simultaneously receive

Type of gas	**Relative ionization probability**
D_2	0.35
H_2	0.44
N_2	1.00
O_2	1.00
H_2O	1.00
CO	1.05
HF	1.40
CO_2	1.40
CH_4	1.60
C_2H_6	2.60
CH_3OH	1.80
C_2H_5OH	3.60

Tab. 3.2.2: Relative ionization probabilities of some gases with regard to nitrogen [after *Balzers*].

Type of gas	Mass number	Sensitivity $x10^{-5}$ [A/mbar]
H_2	2	13
N_2	28	20
CO	28	20
O_2	32	14
CO_2	44	13
CH_4	16	28
C_2H_6	28	34
H_2O	18	20

Tab. 3.2.3: Mass-spectrometer sensitivities of some gases [after *Balzers*].

information for the effusion rates of all gases released during the process but at the expense of the accuracy. This loss of accuracy occurs because of the lack of information in the regions between the measuring points compared with the quasi-continuous spectra for the measurement of a single mass. The mass-spectrometer is also connected to the computer.

The ultra-high vacuum stop valves are: V_1 – for pre-vacuum, V_2 – for ultra-high vacuum. V_3, V_4, V_5 – are used when configured for measuring volume, V_6 – for a ventilation with dry nitrogen, V_7 – for a blocking of the measuring head of the capacitive pressure gauge. V_8, V_9 – are used when the difference pressure chamber of the capacitive pressure measuring head of the gauge has to be evacuated to an ultra-high vacuum and calibrated, V_{10} – for a blocking off of the mass-spectrometer. The V_{11} stop valve serves to block off the rotary pump with the molecular sieve. The quartz tube entrance is closed by a flange, which is sealed by a Cu – ring.

3.2.2. Measuring the effusion rate

The sample is put in the extraction volume in a position near the entrance. The extraction volume is evacuated by the rotary pump and through the valves V_1 and V_{11} for about 10 min to reach $p = 6x10^{-4}$ Torr. Then the pump is turned off and isolated from the extraction volume by closing V_1.

In order to perform the effusion measurement, two different methods were utilized.

The first was to measure the effusion rate of hydrogen as temperature is ramped. When this method is used, the extraction volume, after isolation from the rotary pump, is connected to the ion-getter pump. This is accomplished by an opening of V_2. The ion-getter pump needs about 20 hours to reach the vacuum of about $2x10^{-8}$ Torr which is necessary to perform the

experiment. After achieving the working vacuum, it is essential that part of the internal surface of the quartz tube, which is heated during the effusion, must release the adsorbed hydrogen. For this purpose, the extraction oven is moved to the working position on the rails. The oven's temperature is then raised to $900\ ^{o}C$ by the heat controller. The quartz tube is tempered for about $30\ min$. In this way the danger of the measured results being influenced by the quartz tube is avoided. After the heating, the temperature controller is switched off; the extraction oven is moved back to its initial position away from the quartz tube and cooling, either passive or with the assistance of a ventilator, follows. When the temperature of the extraction oven and the quartz tube reaches room temperature, it is possible for the sample to be shifted to the front part of the quartz tube to a position for the experiment to be performed. This movement is accomplished by means of the magnetic manipulators. The extraction oven is again transposed to the working position. The mass-spectrometer is connected to the extraction volume by opening V_{10}. It is to be mentioned that, before the connection is established, it is necessary for the mass-spectrometer to have already been switched on for at least one hour. This is because at switch off the mass-spectrometer, a strong, temporary desorption from the internal surfaces of the instrument normally appears. This desorption decreases until the apparatus reaches the working temperature. Another undesirable effect is the transient occurrence of partial pressure gradients within the mass-spectrometer. The overcoming of these two effects needs the device to have been working for about one hour before it is ready for correct operation.

Giving a definite temperature regime to the heat controller, we can perform the experiment. A temperature ramp of $20\ ^{o}C/min$ has been used. A computer program written at the institute controls the experiment and collects the measured information. The experimental data are presented in the form of a three-column file - the extraction oven temperature, the sample temperature and the mass spectrometer signal, respectively. The difference between the two temperatures, that of the extraction oven and that of the sample, is about $2\ ^{o}C$ at low temperatures and about $20\ ^{o}C$ at high ones. The increased role of heat dissipation at the higher temperatures is the explanation for the growing difference.

3.2.3. Measuring the absolute gas quantity

The second way to perform this measurement is by means of the effusion of hydrogen at a constant temperature. The selected temperature is high enough to ensure that all possible

SiH_x, x = 1, 2, 3 bonds will be broken and the whole quantity of hydrogen will leave the sample. The hydrogen is pumped out through the measuring volume, whose value is known exactly. Having set the temperature of the gas, its pressure and its volume, the number of hydrogen molecules present in that volume can be determined. This variant of the viewed method is performed in a closed regime within which the ion-getter pump is not connected to the extraction or the measuring volumes during the whole experiment.

The pre-vacuum in the extraction volume is attainable and the switching on of the ion-getter pump is performed in the same way as in the previous section. Additionally, the measuring volume, through valve V_4, and the two chambers of the capacitive pressure gauge, through valves V_7 and V_9, respectively, also have to be connected to this pump. V_8 remains open until the working vacuum is reached but must be closed after calibration of the capacitive pressure gauge. The extraction and measuring volumes are connected through V_3, which is initially open. The same annealing procedure for the walls of the quartz tube and the following cooling is executed as for the measurement of effusion rate. At the end of the preparatory stage of the measurement, the sample is moved to the front side of the quartz tube by means of the magnetic manipulators. The temperature of the extraction oven is meanwhile raised to $800\ ^{o}C$. After achieving the working vacuum of about $2x10^{-8}$ Torr, V_4 and V_2 have to be closed, which means that the extraction and the measuring volumes are no longer being evacuated. The extraction oven is shifted in working position over the front side of the quartz tube and the sample. The effusion begins and, after a certain time of about 3 min, the equilibrium state is reached. The indication of the capacitive pressure gauge has to be read and noted. Then, by closing V_3, the measuring volume is disconnected from the extraction volume. This enables the latter to be evacuated by first opening V_5 to the rotary pump for about $10-30$ sec, and then, after its closing, opening V_4 to the ion-getter pump. By recovering the initial working ultra-high vacuum and closing V_4, the effusion system returns to its initial state and this marks the end of the first measuring cycle. The opening of V_3 and the coupling of the measuring to the extraction volume create the conditions for achieving a new equilibrium state at a lower pressure. The evacuation procedure for the measuring volume can then be repeated. The above-described cycle has to be performed several times (normally 6 or 7) until the threshold of the capacitive pressure gauge's sensitivity is reached. One must ensure that the whole quantity of hydrogen released from the sample during the effusion is pumped out through the measuring volume. Using the addition of the pressures

obtained from each experimental cycle, one can calculate the number of the hydrogen molecules occurring in the measuring volume and creating the resulting pressure at the established temperature.

The utilized formula, which in reality is the equation of state, is

$$N_{H_2} = L\frac{\Delta V}{V_A}\frac{T_0}{T_1}\frac{\Delta p}{p_0}, \qquad (3.2.1)$$

where:

L is the Loschmidt's constant $(6.02252 \pm 0.00028)\text{x}10^{23}\ \text{mol}^{-1}$ and equals the number of molecules in one mole of substance,

T_0 is the $0\ ^\circ\text{C}$ temperature or $273\ \text{K}$ on Kelvin's absolute temperature scale,

p_0 is the atmospheric pressure of $760\ \text{Torr}$,

V_A is the molar volume or the volume of one mole substance at $0\ ^\circ\text{C}$ temperature and $760\ \text{Torr}$ pressure and equals $(2.24136 \pm 0.00030)\text{x}10^{4}\ \text{cm}^3$,

ΔV is the measuring volume of $834\ \text{cm}^{-3}$,

T_1 is the Kelvin temperature of the gas,

Δp is the change of the gas pressure after effusion of the sample.

Because L, V_A, T_0, p_0 are absolute constants and ΔV is constant for this experiment, eq. (3.2.1.) can be rewritten in the form:

$$N_{H_2} = 7{,}9574259\text{x}10^{21}\frac{\Delta p}{T_1}, \qquad (3.2.2)$$

where Δp is in Torr and T_1 in K. The value of the molar volume of an ideal gas has been corrected for H_2 real gas to $2.2442\text{x}10^{4}\ \text{cm}^3$.

References

1. *Balzers* Balzers, quadrupole mass-spectrometer QMG 111, User instruction Nr. BG 800 001 BD, Edition: December 1971/DN 4640.

Chapter 4. GRAVIMETRY AND EFFUSION OF HYDROGEN AT A CONSTANT TEMPERATURE FOR H/SI ATOM NUMBER RATIO DETERMINATION

An experimental determination of the atom number ratio H/Si in porous silicon plays a crucial role in the selected approach to the silicon particle size assessment. A combination of two methods, gravimetry and thermal effusion, gives the possibility for such an experimental result. In this connection, the effusion at a constant temperature delivers the number of hydrogen atoms and the gravimetry is responsible for determining the number of silicon atoms.

4.1. Gravimetric method

The gravimetric method results in the determination of the sample weight. A distinctive feature of the investigated samples is the fact that most of them, except the freestanding mesoporous samples, remain connected to the substrate on which they are grown after their preparation and so cannot be weighed independently. The wanted component can be found by an initial weighing of the sample together with the substrate and, following chemical or mechanical separation of the sample from the substrate, performing a second weighing of the substrate alone. The difference between the two measured weights represents the sample weight. This indirect method has the disadvantage that it demands mechanical stability of the substrate during the treatment. The substrate itself is a rectangular section cut from a silicon wafer delivered, for instance, from “Wacker”. To avoid the danger of a piece of material from the edges or corners being broken during handling, smooth edges to the rectangular cut are required. These may be machined using a “Tempress” diamond-scratching machine.

Separation of the sample from the substrate is performed by scrapping off the sample with the help of a scalpel under a microscope.

Checks were made for monitoring of the scrapping off quality and its influence on the weight value. Thus, the selected procedure was proved trustworthy. Because of the big difference between the fill factors of the substrate $(FF_{Si} = 1)$ and that of the porous structure $(FF_{PS} \approx 0.3)$ and between their solidity respectively, both media can be easily separated. A microscope with a magnification of 16 times is sufficient to allow the scrapping off process to be reliably controlled. A “Mettler” precision mechanical balance of $5\,\mu g$ accuracy was used

for weighing. Assuming that the skeleton of the porous silicon structure consists only of Si atoms and knowing the number of Si atoms in 1 g of monocrystalline Si to be 2.10×10^{22} [see *Sze*], one can determine the entire number of Si atoms in the sample from its weight.

4.2. H/Si atom number ratio as a standard for the surface to volume ratio of the porous structure

It is known that the hydrogen atoms are bound to the silicon atoms on the internal surface of the porous silicon structure. Thus, the number of hydrogen atoms and the bond type distribution between mono-, di- and trihydride determines the total number of silicon atoms, which lie on this surface. The relative presence of the various hydrides depends on the surface condition, which will be discussed in detail in chapter 8 of this work. If one is familiar with the surface density of the silicon atoms, the total number of the hydrogen atoms appears as a standard for the magnitude of the surface area.

Conversely, nothing in the literature suggests that the core of the skeleton is other than crystalline silicon. This latter observation justifies the statement that the number of the silicon atoms is a standard for the volume of the skeleton.

Consequently, the H/Si atom number ratio expresses the surface to volume ratio for the porous silicon structure and in this way characterizes the structure itself.

4.3. Experimental results

As already described (see part 2.3.), a set of production parameters determining the porous silicon structure exists. Our aim is to obtain structures with clearly distinguishable values of the H/Si atom number ratio by varying of those parameters. The strategy we chose was to change one of the production parameters while keeping all others constant. The following four parameters were varied in the attempt to obtain the structural modifications sought:

- changing the etching current density;
- changing the substrate resistivity;
- chemical post-etching;
- changing the illumination through selected filters during the etching procedure.

The values shown below have to be viewed as representative of a far greater number of performed measurements giving reproducible results.

4.3.1. Influence of the etching current density

The etching current density was varied over a wide interval of three orders of magnitude, $1 \div 1000\ \mathrm{mA/cm^2}$, and a great number of samples were measured. Substrate resistivities of $1-10\ \Omega\mathrm{cm}$ and an etching solution of $HF : C_2H_5OH : H_2O = 1:2:1$ were used. The samples were made in darkness. To reduce the measurement error, the method requires samples to be as thick as possible. The following problems arise in their preparation. At small etching current densities, the etching velocity is also small. For example, at $1\ \mathrm{mA/cm^2}$ etchcurrent density, the etching velocity is $1\ \mu\mathrm{m}$ per $15\ \mathrm{min}\ 51\ \mathrm{s}$ for a nanoporous sample (see section 2.3.). For the same sample, a thickness of $5\ \mu\mathrm{m}$ demands more than $1\ \mathrm{hour}\ 15\ \mathrm{min}$. Remaining in the etching solution for such a long time enhances the probability of a noticeable in-depth structural inhomogeneity to occur. This is a result of chemical etching taking place simultaneously with the basic electrochemical process. Thus, a thickness of more than five $\mu\mathrm{m}$ is not recommended for such of samples.

At higher etch-current densities, about $300\ \mathrm{mA/cm^2}$ and more, the porous structure formed is very unstable mechanically. This complicates their treatment and makes the results less than completely reliable. This fact limits the admissible thickness of the samples. The results obtained are presented in table 4.1. The types of contact used (see part 2.2.) and, in one case, a crystallographic substrate orientation, which differed from that usually utilized $[100]$,

Etchcurrent density [mA/cm^2]	H/Si atom number ratio [%]
1	35.60(Al)
5	38.57(Al)
10	35.65(Al); 35.11
30	43.30(HF); 43.37(Al); 43.33(Al); 37.54(Al); 41.66(Al); 39.88(Ga);
50	45.04(HF); 46.34(Al); 34.79; 43.50([111]);
80	42.65(HF);
100	39.40(Al); 41.80(Al); 46.27;
300	82.62(Al);
1000	78.47;

Tab. 4.1: Obtained H/Si atom number ratio vs. etch-current density.

are shown in brackets.

4.3.2. Influence of substrate resistivity

A series of boron doped silicon wafers of resistivities in the interval from $5 \div 20$ mΩcm up to 106 Ωcm were used as a substrate. Two different concentrations of a liquid HF were used as etching solution components. Both the concentrations of 40% and 50%, respectively, are determined by the producer. $HF : C_2H_5OH : H_2O = 2:5:3$ was the composition of the etching solution in the first case, and $HF : C_2H_5OH : H_2O = 1:2:1$ in the second. The etching current density was 30 mA/cm^2 and the samples were prepared in darkness.

It has to be mentioned that, when highly doped degenerate material is used, the implementation of the measurement is possible only in a freestanding realization. It is experimentally established that a sample on such a substrate can't be scrapped off so that the weight of the porous structure can't be determined. The results obtained are presented in table 4.2.

Substrate resistivity [Ωcm]	**H/Si atom number ratio [%]**	
	Etching solution HF(40%) : ethanol = 1:1	**Etching solution HF(50%) : ethanol = 1:1**
0.01		15
0.2÷0.4	35.69	42.44
5		40
10.23	47.30	42.57
106	43.63	38.47

Tab.4.2: Obtained H/Si atom number ratio vs. substrate resistivity.

4.3.3. Chemical post-etching

This procedure is based on the well-known fact that two independent etching mechanisms take place during the porous structure formation. The first is the basic electrochemical mechanism associated with the current flowing through the substrate and the simultaneous influence of the etching solution. This process is the faster. The second is caused only by the

contact of the porous silicon with the etching solution and has a purely chemical nature. This process is slower and its influence is evident only after the sample has been lying in the etching solution for longer than one hour. An attempt was made to influence the structure, and thus the H/Si atom number ratio, of four identically prepared samples by varying their time remaining in the etching solution after the etch-current had been switched off and so the electrochemical etching had ceased. The samples were prepared on boron-doped substrate of $1-10\ \Omega\mathrm{cm}$ resistivity with $HF : C_2H_5OH : H_2O = 1:2:1$ etching solution and1 0 mA/cm^2 etch-current density. Table 4.3 shows the results.

Postetch-ing [min]	**H/Si atom number ratio [%]**	
	10 mA/cm^2 etchcurrent density	**30 mA/cm^2 etchcurrent density**
after Prepara-tion	36.68(Ga)	39.04(Ga)
30	41.30(Ga)	35.63(Ga)
60	43.30(Ga)	39.01(Ga)
120	31.80(Ga)	35.90(Ga)

Tab.4.3: Obtained H/Si atom number ratio vs. postetching time.

4.3.4. The Influence of illumination through selected filters during the etching procedure

This series was made in the presence of illumination through selected filters as a microstructure forming parameter. A substrate resistivity of 4.5÷6 Ωcm, a current density of 10 mA/cm^2 and an etching solution $HF : C_2H_5OH : H_2O = 1:2:1$ was used. The experimental

Illumination conditions (cut-off wavelengths of low-pass filters [nm])	Sample **thickness** [μm]	H/Si atom number ratio [%]
in darkness	insignificant	35.72
665	15	37.30
550	5	44.74; 47.50; 41.42;
450	1	46.28
without filter	1	59.26; 59.57; 58.35

Tab.4.4: Obtained H/Si atom number ratio vs. illumination.

conditions are described in section 2.3 and the thicknesses of the samples (see table 4.4) were chosen in conformity with the considerations discussed in that section. The results obtained are presented on table 4.4.

4.4. Comments

The results from the “etch-current density” series show that the values of the H/Si atom number ratio are generally increased for higher etch-current densities. This can be clearly seen when one compares the values on both boundaries of the interval of used etch-current densities. Independently of the reservations, which we have towards the values at high etch-current densities, the difference of about $30\,\%$ in the H/Si atom number ratio is sufficiently significant to allow conclusions to be drawn. In the interval $1 \div 100\ \mathrm{mA/cm^2}$, there are differences in the structures, which cannot be overlooked. After preparation, the samples produced with $1\ \mathrm{mA/cm^2}$ exhibit better mechanical stability and their color is dark brown. The $100\ \mathrm{mA/cm^2}$ samples compared with them are more fragile and have light brown color. Other methods, more sensitive than thermal effusion (see section 5.1.), also confirm the existence of such differences. It is probable that a very high number of effusion and gravimetry measurements for each individual etch-current density presented in table 4.1 would distinguish inherent values of H/Si atom number ratio. From our measurements in the interval viewed, although the tendency can be established, it is not possible to determine the value of the used etch-current density if we have an experimental value of the H/Si atom number ratio for a certain porous structure. In other words, the sensitivity of this method is not sufficient for such a task. All that can be said is that a measured value of about $35\,\%$ most probably belongs to a structure produced by $1\ \mathrm{mA/cm^2}$ and a value of about $46\,\%$ to a $100\ \mathrm{mA/cm^2}$ structure. The results near the upper boundary of the operating interval can be generalized with the statement that a value of about $80\,\%$ is characteristic for a porous structure created by a few hundred $\mathrm{mA/cm^2}$ etch-current density. The data obtained don’t allow more precise conclusions.

The results from the “substrate resistivity” series show that they can be divided into two groups. This separation corresponds to the two types of porous silicon structure (see section 2.4.) formed on heavily and on lightly doped substrates. The values of the H/Si atom number ratios for these two different structures differ significantly. For the structure formed on a heavily doped substrate of $0.01\ \Omega\mathrm{cm}$, the values are about $15\,\%$. For structures formed on lightly doped material, the results obtained group around the value of about $40\,\%$. The

resistivity in the second group varies over an interval of three orders of magnitude. No tendency for the results to very over this interval can be recognized. The rapid change essentially takes place in the region $0.01 \div 0.2\ \Omega\text{cm}$, where the transition from the first to the second porous structure also happens. It is remarkable that this region encompasses a change in the substrate resistivity of only one order of magnitude.

The postetching method was considered as promising, which allows the particle size change to be followed over a wide interval from that value, determined by the production parameters from the electrochemical etching to the complete dissolution of the structure. This is why the method has been intensively applied on structures formed at low etch-current densities, which presumably create large enough particles for a clear tracking of the procedure operation. However, the results obtained show that the effusion plus gravimetry method can't establish any tendency in the value of the H/Si atom number ratio dependent on the time for which the sample lies in the etching solution after the etch-current is switched off. The differences in the measured values are a result of the combined effusion plus gravimetry method sensitivity and don't reflect a change in the structure. Conversely, one must consider:

- the visually observed change,
- the change of the remaining substance weight from the gravimetric measurements (e.g. for the series produced by $10\ \text{mA/cm}^2$ etching current, the weight of the sample is: after preparation – $955\ \mu\text{g}$, after $30\ \text{min}$ post-etching – $514\ \mu\text{g}$, after 1 hour – $440\ \mu\text{g}$ and after 2 hours– $346\ \mu\text{g}$),
- the reduction of the area under the characteristic peaks in the infrared transmission measurements shows that the substance of the samples dissolves in the etching solution. One possible explanation for this fact is that the dissolution does not take place by a successive reduction of the particle size. The chemical etching probably causes the skeleton to break-off at its narrowest points and the separation of whole complexes of particles to follow.

Most fruitful are the results obtained from the fourth series. The usage of different filters enables mechanically stable structures to be produced, which, at the same time, differ significantly in the values of their H/Si atom number ratios. In both extreme cases, preparation in darkness and under direct illumination, the difference amounts to more than $20\ \%$. We present one possible explanation of the role of light in the etching procedure. According to the accepted theory (see section 2.5.) for the electrochemical dissolution of silicon, the availability of holes in the material is of primary importance. The absorbed light causes, by means of inter-band (valence to conduction band) transitions, the appearance of electron-hole pairs and in this way supports the etching process. The quantum size effect

requires a band gap widening to be associated with the decrease in the size of the particles building the porous silicon skeleton. On other hand, the utilization of a particular low-pass filter defines the shortest wavelength, and thus the most energetic quanta, that appear in the incident illumination. The following etching process causes progressive particle size reduction, which terminates with the completion of the electron-hole pair creation. The latter happens when the band gap reaches the value of the most energetic quanta. In this way, the particle size depends on the selected filter. In our opinion, it is possible for the whole interval of H/Si atom number ratio values from about $36\ \%$ to about $59\ \%$ to be uninterruptedly filled by the selection of appropriate filters. Using other etch-current densities or an alteration of the etching solution, values outside this interval could be achieved.

4.5. Estimation of the experimental error

In the following table 4.5, a review and an assessment of the experimental errors, which have a bearing on the accuracy of the measured quantities in the considered method, are given.

In order to determine the random error, a series of measurements using identical production parameters has been made and the Gauss error reproduction law used for calculations.

The inaccuracy in determining the measured volume is given by the effusion installation producer.

The average weight of the samples considered and the accuracy of the precision balance determine the weighing error. An average value of about $800\ \mu g$, together with the device

Error estimation		
Nr.	Measured quantity	Relative error (%)
1.	Measuring volume: $824 \pm 6\ cm^3$	< 0.8
2.	Sample weight	0.7
3.	Temperature measurement	0.17
4.	Pressure measurement:	< 1
5.	Residual gas in the sample	< 1
	Resultant error	< 2

Tab.4.5: Error estimation of H/Si atom ratio determination.

accuracy of $5x10^{-6}$ g, forms an error of about 0.7 %.

For temperature measurements, values have been rounded to full degrees for a consequent accuracy of ± 0.5 deg. The average room temperature of about 298 K, at which the volume is measured during the experiment, defines a relative error of about 0.17 %.

The average value of the absolute pressure for the hydrogen-poorest porous silicon structures, which we have measured, is about 0.013 Torr and the accuracy of the capacitive pressure gauge is $1x10^{-4}$ Torr. This means a relative error smaller than 1 %.

The value at the last (fifth) step is clearly always smaller than 1 % of the entire measured pressure value. That means a relative error for the residual gas in the sample of less than 1 %.

Having in mind how the hydrogen to silicon atom number ratio depends on the above-presented quantities and using the Gauss error reproduction law, it can be asserted that the entire relative error is about 2 %.

An additional factor for the assessment of the experimental error is the drift of the zero reference of the capacitive pressure gauge during the measurement. To reduce the influence of this drift on the result, we make the following correction. The apparatus is adjusted before the first and after the last step of the measurement (see section 3.2.3.). The difference D between the two values is divided by the number of the measurement steps M minus one. It is assumed that any misalignment during the measurement takes place linearly with time and can be positive or negative. The second step value thus needs a correction factor of $\frac{D}{M-1}$, the third step - $\frac{2D}{M-1}$,...., the M-th step - $\frac{(M-1)D}{M-1} = D$. The general correction R_d to the obtained pressure is a sum of the corrections at every step of the measuring procedure:

$$R_d = \pm \frac{[1 + 2 + ... + (M-1)]D|}{M-1}. \tag{4.1}$$

The magnitude of this correction depends on the number of steps M and the duration of the measurement. In practice, five steps are sufficient to complete the measurement in most cases and R_d isn't larger than 2 %.

Another approach incorporates repeated measurement of samples produced under the same structure-determining parameters (see in tab.4.1 the obtained H/Si atom number ratio values at 30 mA/cm^2 etch-current density). This leads to a value of about 3 % for the statistical error in determining the H/Si atom number ratio. The standard deviation from the mean value is used.

If we supplement the $4\,\%$ systematic error originating from the supposed inaccurate determination of the H-atom number, we obtain about $7\,\%$ error for the H/Si atom number ratio determination.

4.6. Conclusions

- By changing the four structure-determining parameters – etch-current density, substrate resistivity, duration of post-etching and illumination during etching, a wide interval from about 12 % to about 78 % in the values for the hydrogen to silicon atom number ratio has been achieved;

- There is an ‘empty’ region in the above-mentioned interval of hydrogen to silicon atom number ratio values between about 17% to about 36% in which values have not been obtained by the procedures utilized and the selected values for the structure determining parameters;

- It has been discovered that the experimental error in the H/Si atom number ratio determination is about $7\,\%$.

References

1. *Sze* S.M. Sze, Physics of Semiconductor Devices, John Wiley, New York (1981).

Chapter 5. OTHER METHODS FOR COMPOSITION DETERMINATION

Having in mind the crucial role of the H/Si atom number ratio for the selected approach to a particle size assessment, it is relevant to confirm the values obtained. Parallel to the main technique of thermal effusion, two other methods have been utilized on some of the porous structures: a) Elastic Recoil Detection Analysis and b) “Burning” in an O_2 atmosphere. The first method also gives information concerning the very important question (see chapter 7) of oxygen (and oxide) availability in the as-prepared porous structure.

5.1. Elastic Recoil Detection Analysis (ERDA)

The elastic recoil detection analysis, especially when performed with highly energetic heavy ions (e.g. $60-170\ \mathrm{MeV}$), is a suitable method for measuring depth profiles of light and medium heavy elements in thin films. The advantages of this procedure are reliable quantitative results and elementally and isotopically resolved depth profiles. An essential reason for the attractive potential of the technique is the ability to detect all background elements, especially the light elements (H to F), with sensitivities in the p.p.m. range. The method itself was originally developed for H detection with He beams. Its more general application for light element detection, if heavier beams are used, was first pointed out by L’Ecuyer at the University of Montreal [see *L’Ecuyer*]. The increasing availability of accelerators with heavier ion beams and higher energies and the development of advanced detection techniques have created the possibility of ERDA being applied to the measurement of a wider spectrum of elements; up to mass 100 ($Z \approx 40$).

5.1.1. Principle

A schematic drawing of the ERDA method is shown on fig. 5.1.1. The samples are

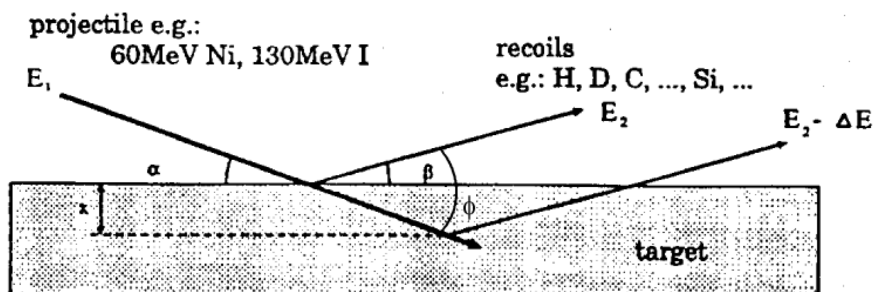

Fig. 5.1.1: Principle of an ERDA setup [after *Dollinger1*].

irradiated by a heavy ion beam, e.g. 170 MeV ^{127}I. The irradiation is performed at small angles of incidence α, allowing the detection of recoil ions, which are also scattered at relatively small forward angles ϕ to the ion beam direction (e.g. $\phi = 40^0$) on the same side of a bulk target; the so-called reflection geometry. The use of small angles of incidence α and exit β is intended to enhance the relative energy resolution and the depth resolution, respectively. This means the energy spread obtained for recoil ions scattered at a certain depth is kept lower than the energy shift of recoil emissions from the two adjacent layers in order to get a separate signal for each layer in the recoil energy spectrum. The kinetic energy of the ejected atoms depends on the scattering angle and the energy loss of both the incoming and the ejected atom on the distance covered in the samples. Quantitative concentration profiles dependent on the depth under the surface of the sample can be obtained from the measured relative recoil energy shift $\Delta E_R/E_R$ of the backscattered ions with respect to those coming from the surface. A compact hybrid $\Delta E - E_{res}$ detector telescope is used to get profiles of all elements simultaneously. The depth of the origin and the elemental information can be measured separately for each detected recoil ion. Especially the carbon, nitrogen and oxygen but also the hydrogen isotopes can be analyzed with high accuracy.

When light primary ions are applied, the usage of the technique is limited to the analysis of very light ions. The light projectiles are also scattered into the detector with a much higher count rate than the recoil atoms due to the higher scattering cross sections of the primary ions in forward directions. In order to avoid pile-up problems, the scattered projectiles are stopped in a foil of correctly tuned thickness positioned in front of the detector. With such a foil, only ions lighter than the primary ions, in many cases only hydrogen can be measured. This disadvantage can be avoided by using high-energy heavy ions (e.g. $1-3$ MeV/u, I or Au). As long as the masses M_P of the primary ions used are higher than the masses M_R of the main target atoms, the primary ions are scattered only in a cone with a halfangle θ_{max} given by two-body kinematics:

$$\theta_{max} = \arcsin(M_R/M_P) \qquad (5.1.1)$$

and cannot be scattered outside this angle. If the detector is positioned at an angle larger than θ_{max}, the scattering of the primary beam into the detector will be eliminated and in this way the overlap of scattered projectiles with recoil atoms in the coincidence spectrum will be avoided, which reduces the dead time of the detector. The advantage of ERDA in this case, concerning the quantification of the experimental data, is the possibility for an unambiguous identification of the back-scattered ions. Since ions of atomic number Z whose velocity lies

in the region $v_B Z^{2/3}$ (v_B – Bohr's velocity) and above differ in their specific stopping powers (stopping power per unit path), by using high-energy heavy projectiles, enough energy is transferred in a collision that particle identification may be made by measuring the residual energy and energy loss. A compact $\Delta E - E_{res}$ detector telescope, consisting principally of a transversal field Frisch grid ionization chamber for energy loss (ΔE) measurements and a silicon position sensitive PIN diode for residual energy measurements (E_{res}), is installed as a detector [see *Bergmaier1*]. The two quantities of the energy loss ΔE and the residual energy E_{res} are obtained for each impinging target ion and the assembly of such data forms a two-dimensional $\Delta E - E_{res}$ matrix.

5.1.2. Theory

The concentrations (atomic fractions) of all light and medium heavy elements in the sample can be obtained directly from the respective yields and the known differential Rutherford scattering cross sections [see *Dollinger2*]

$$\frac{\partial\sigma}{\partial\Omega} = \left[\frac{e^2}{8\pi\varepsilon_0}\frac{Z_P Z_R}{E_P}\frac{(M_P + M_R)}{M_R}\right]^2 \frac{1}{\cos^3\phi} \tag{5.1.2}$$

where Ω is the solid angle of the detection, $M_{P,R}$ and $Z_{P,R}$ are respectively the masses and the atomic numbers of the projectile and the recoil atom and E_P is the kinetic energy of the projectile.

Since the ratio Z_R/M_R is almost constant for all elements except hydrogen, recoil cross sections are nearly independent of the recoil species. Thus light and heavy elements can be detected with almost equal sensitivity and hydrogen with larger sensitivity than any other element. Another characteristic feature of the ERDA cross section is the strong $Z_P^2 M_P^2/E_P^2$ dependence on the projectile mass and atomic number. Even if we compare different projectiles with the same E_P/M_P value, the Z_P^2 dependence remains. Because of the very small beam currents (i.e. usually $< 10^9$ ion/s), the beam heating effects are even smaller than when using light ions.

The recoil energies, which come from a δ-layer lying x in depth under the surface of the sample, can be described by a distribution function $f(x)$. The depth resolution is defined as the smallest distance δx at which the sum of the two distribution functions $f(x)+f(x+\delta x)$ has a local maximum. If the distribution functions are symmetric, the depth resolution $\delta x(x)$ is

directly related to the energy width $\delta E_R(x)$ of the recoil energy distribution:

$$\delta x(x) = \frac{\delta E_R(x)/E_R}{\dfrac{S_P}{E_P \sin\alpha} + \dfrac{S_R}{E_R \sin\beta}} \tag{5.1.3}$$

where $S_{P(R)}$ is the stopping power of the projectiles (the recoil), respectively. This formula shows the linear dependence of the depth resolution δx on the relative energy resolution $\Delta E/E$ of the experimental setup. The total energy resolution attained, which depends on the experimental conditions, is $\Delta E/E \approx 1\%$ for the detection system used in these measurements.

The importance of the condition that the two angles α and β be small for the depth resolution is obvious. The actual depth resolution achieved in the experiment was about $10\ \text{nm}$.

The surface nature also plays a certain role in the attainable depth resolution. One very rough surface is shown on fig. 5.1.2. At small angles α and β for the incident and the deflected beam respectively, shadow effects are possible. One of the two projectiles on the figure has already lost energy in the sample before the collision happens. Because of the already reduced energy at the moment of the collision, a source point below the surface will erroneously be allocated to the recoil ion.

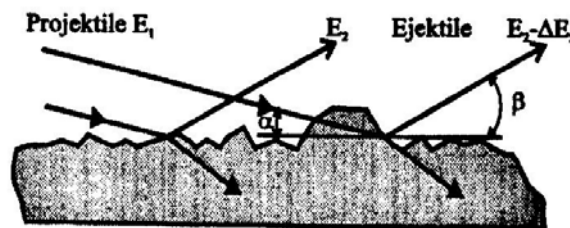

Fig. 5.1.2: Influence of the surface roughness on the depth resolution [after *Frey*].

5.1.3. Data analysis

The procedure for determining the depth profiles from the primary spectra is shown and commented upon in detail in ref. *Bergmaier2*. From ERDA measurements, one normally obtains an $\Delta E - E_{res}$ energy matrix in which all recoil elements are well separated. In two steps, this spectrum can be converted first as $\Delta E - E_{tot}$ $(E_{tot} = \Delta E + E_{res})$ for all available elements in the sample and subsequently, by using an appropriate programme, in a counts-energy spectrum for each element in the target. The main problem with the conversion from raw energy spectra to concentration profiles is the transformation of the energy scale into a depth scale. This transformation depends on the energy loss of the projectiles and the recoil

events in the sample. On the other hand, this energy loss depends on the elemental composition given by the yield for the different elements. In order to obtain the correct number of events for a certain slice of depth, the corresponding energy band has to be known which, in turn, depends on the energy loss. Therefore, an endless loop has to be solved by iteration. It has to be mentioned that the stopping powers of the projectiles and the recoil events in the different monoelemental matrixes, which are used in this procedure, are tabulated. Also, a linear additivity of the atomic stopping powers (Bragg's rule) is assumed.

5.1.4. Experimental results

In performing these measurements, we have pursued several aims. The first was to compare the results with those obtained by thermal effusion for similarly prepared samples. A second purpose was to use the method as arbitral for some results from EXAFS (see chapter 6) and effusion experiments on samples prepared under reported conditions [see *Schuppler*]. This method can also be helpful in answering the question of whether there is a significant presence of oxygen (and oxide) in the freshly-prepared samples shortly after their preparation as an additional result.

A series of measurements has been made in order to determine the composition of the samples prepared as shown in tab. 5.1.1. Samples 1 and 2 present a typical mesoporous structure in a freestanding configuration and on a substrate respectively. Their preparation parameters refer samples 3, 4 and 5 to the most investigated nanoporous structures. The last two samples, 6 and 7, were produced under the same conditions as samples A and B respectively on table I in the ref. *Schuppler* in order to check the values of the atom number ratios H_H/N_{Si} obtained by EXAFS (see chapter 6) for these structures. All samples were

Sample Nr.	p-Si(100), backimplanted, resistivity (Ωcm)	Etching solution ($HF:H_2O:C_2H_5OH$)	Current density (mA/cm^2)	Etching time	Thickness (μm)
1	$(5\div25)\times10^{-3}$	1:1:2	50	2 min 56 sec	10
2	$(5\div25)\times10^{-3}$	1:1:2	50	1 min 28 sec	5
3	1÷3	1:1:2	1	15 min 51 sec	1
4	1÷3	1:1:2	50	1 min	2
5	1÷3	1:1:2	100	47 sec	3
6	20÷200	1:1:3	20	60 min	
7	20÷200	1.5:1.5:7	25	12 min	

Tab. 5.1.1: Preparation parameters of the measured PS samples.

produced in darkness and immediately after the preparation inserted into the measuring volume under vacuum for the ERDA measurement.

On fig. 5.1.3 a)-i) are shown the experimental results from the whole series presented on tab. 5.1.1. The number of atoms N, which the volume of the sample contains down to the particular depth, normalized to the surface area, appears on the x-axis. In other words, it is the number of atoms in the volume of a rectangular parallelepiped, whose first of the two $1\,cm^2$ bases' areas lies on the surface of the sample and the second one - at a certain depth in the sample, given by the edge length. If we suppose a differential rise of the edge length from l to $l + \Delta l$, this corresponds to an increase of the parallelepiped's volume. The newly formed volume dV contains dN number of atoms including dN_H number of hydrogen, dN_{Si} number of silicon and so on atoms. The quantities dN_H/dN and dN_{Si}/dN present the corresponding hydrogen and silicon atom concentrations characteristic of a particular depth. This is an average concentration of atoms lying in the plane occurring at the particular distance from the surface and is represented on the y-axis of the graphs. (Such a definition of the displayed concentration makes it clear that from the ERDA measurement technique no lateral resolution can be obtained).

Figs. 5.1.3 a) and b) give the concentrations' profile of two identical porous structures – sample 1 and 2, as freestanding and "on substrate" realization, respectively. Figs. 5.1.3 c) and d) are related to one and the same structure – sample 3, where c) shows the profiles only for Si and H. After completion of the ERDA measurements for structures 3 and 4, they were scraped off the substrate by a scalpel under a microscope. This is, in fact, a repetition of the procedure for the gravimetric experiment (see chapter 4.1.). The newly revealed surface and the underlying residual substrate for both samples have been also investigated by ERDA.

Fig. 5.1.3 d) shows the profile of sample 3 after scrapping off. In figs. 5.1.3 e) and f) are presented the concentration profiles of sample 4 after preparation and after scrapping off respectively. The experimental results for samples 5, 6 and 7 after preparation, in this order, are seen on fig. 5.1.3 g)-i). It has to be mentioned that, on some of the pictures, the measuring points are connected in different ways, directly or stepwise, but that this has no bearing on the results appearing in the next table.

The volume average atom concentrations for all elements available in the samples in significant amounts are shown in table 5.1.2. The presented errors include the following two components: a) the statistical error and b) the $5\,\%$ error, which accommodates the indeterminacy in defining the porous structure boundary in the substrate.

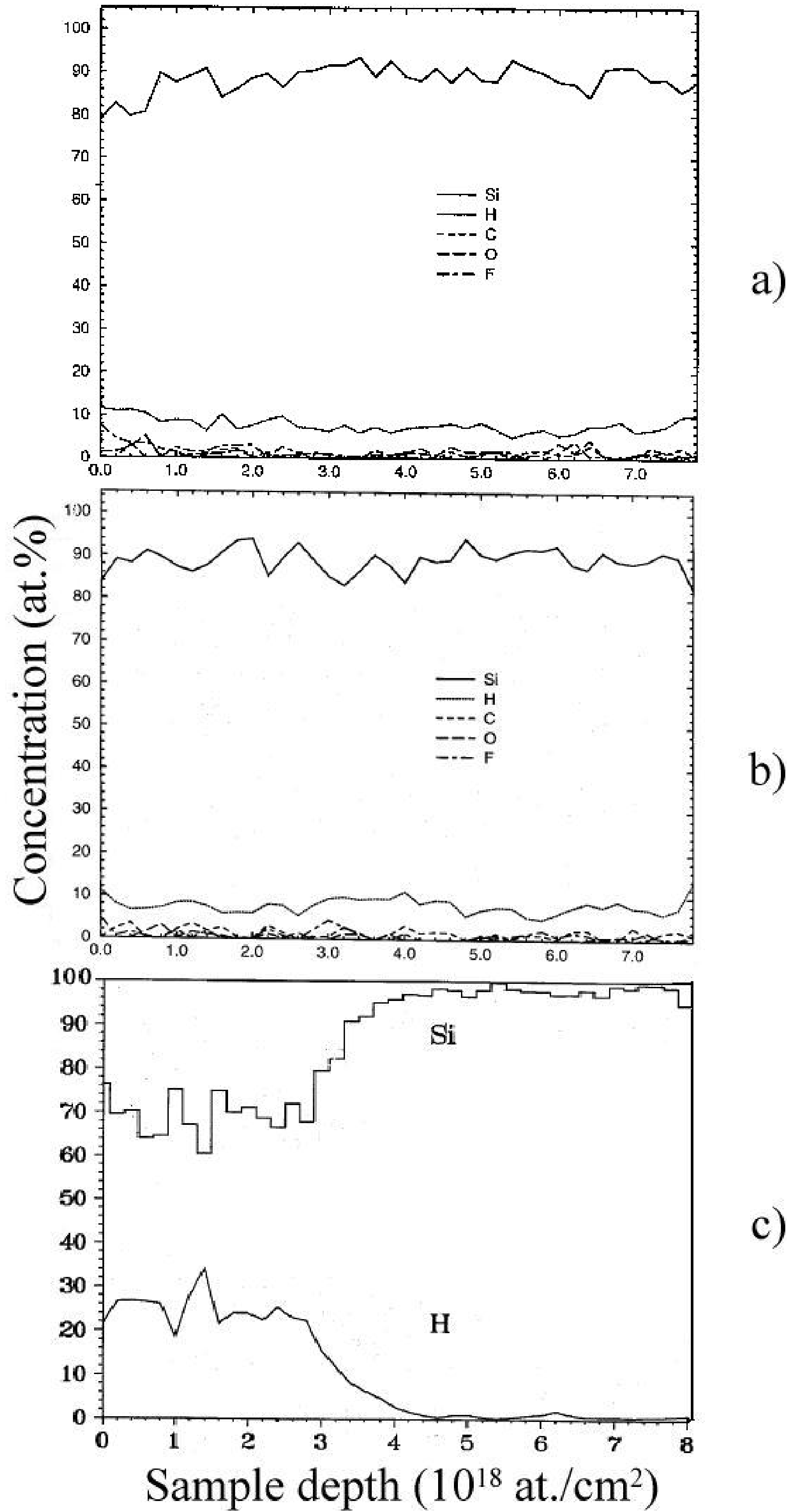

Fig.5.1.3: ERDA results from the samples in tab. 5.1.1:

a) concentration profiles of the available elements in as-prepared sample 1;

b) concentration profiles in as-prepared sample 2;

c) Si and H concentration profiles in as-prepared sample 3.

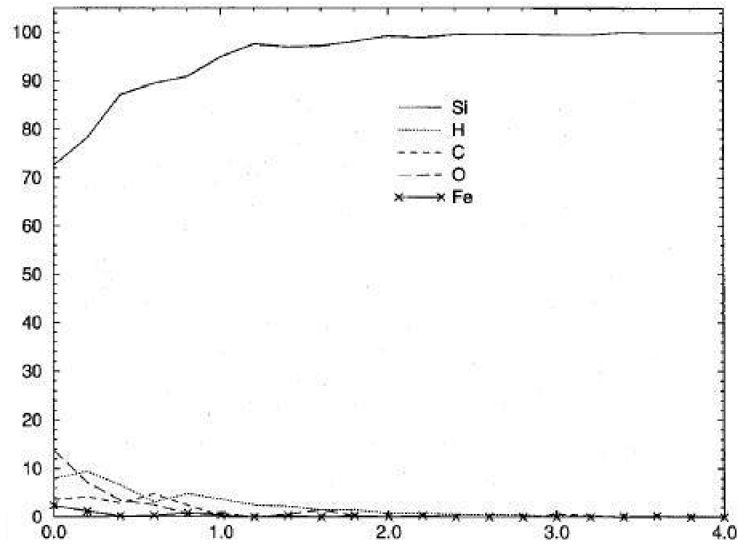

d)

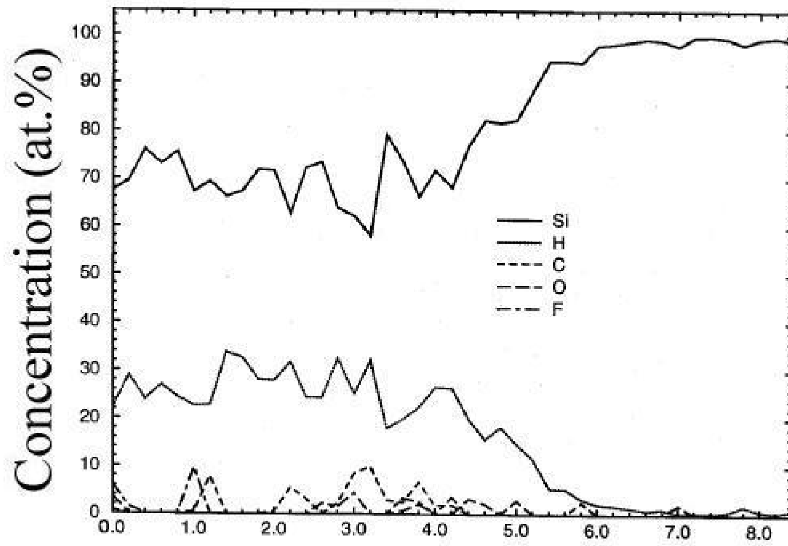

e)

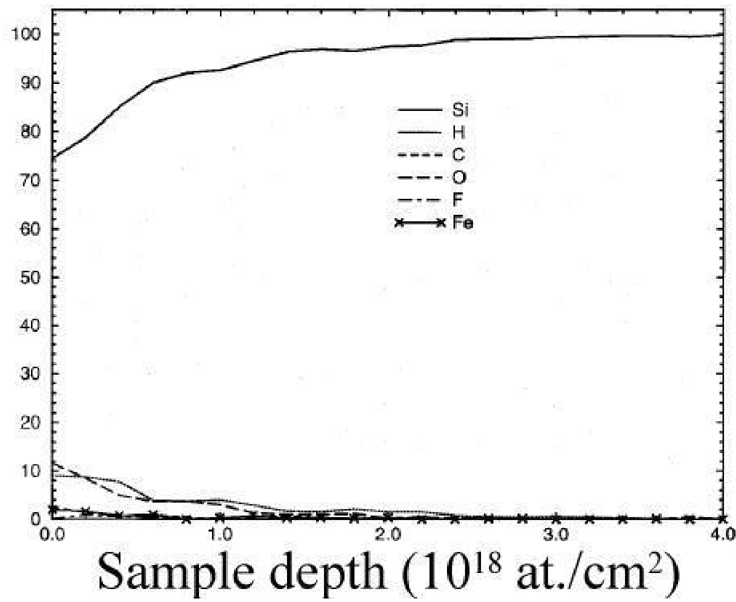

f)

d) concentrations' profile of sample 3 after scraping off;

e) concentrations' profile of as-prepared sample 4;

f) concentrations' profile of sample 4 after scraping off;

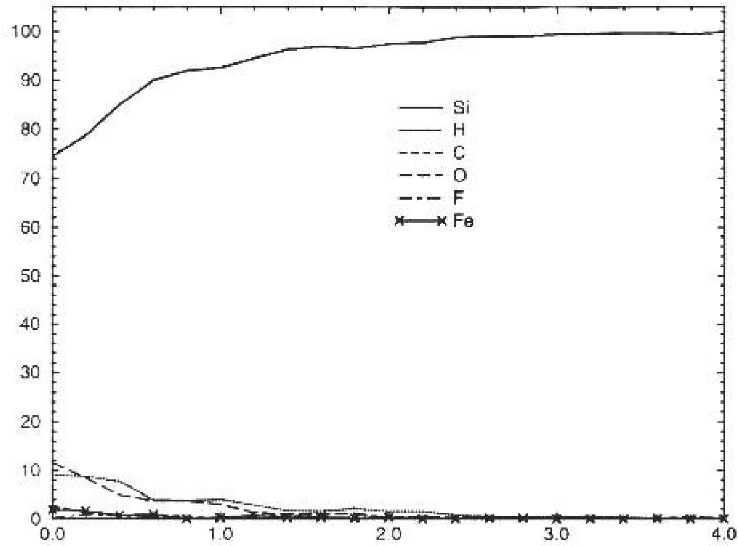

g)

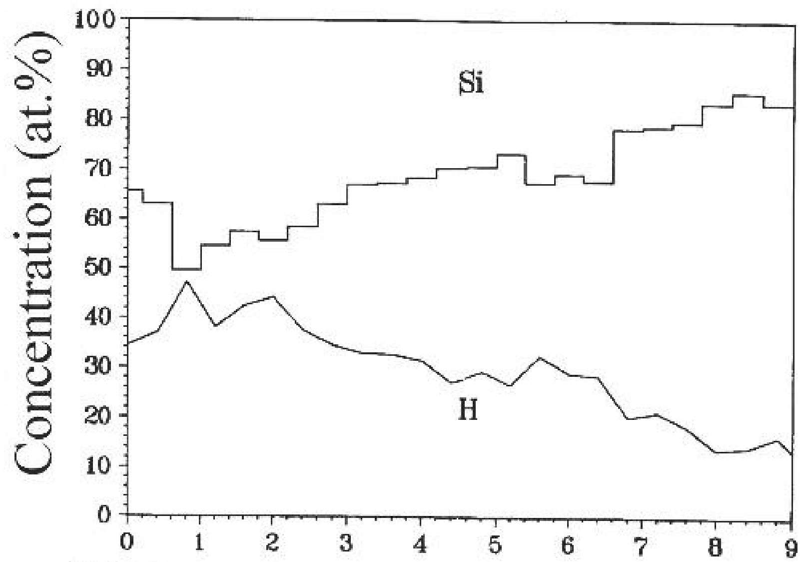

h)

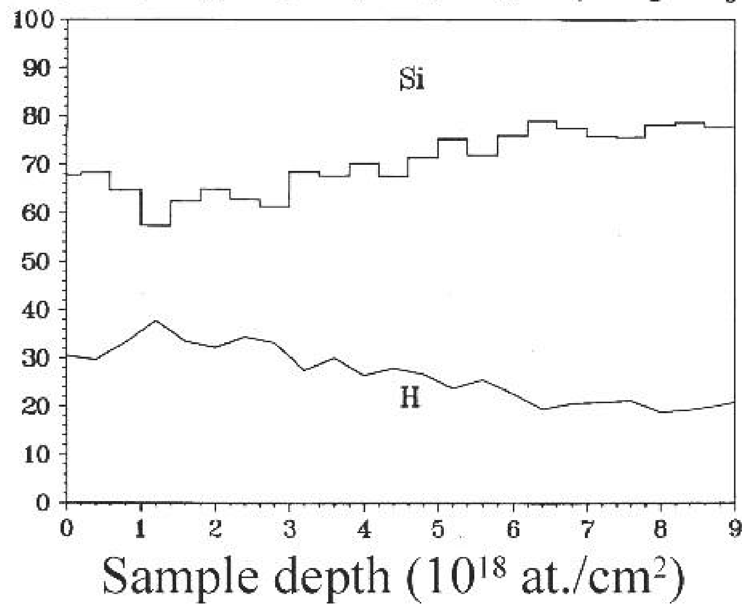

i)

g) concentrations' profile of sample 5 as-prepared;

h) Si and H concentration profiles of as-prepared sample 6;

i) Si and H concentration profiles of as-prepared sample 7.

Sample Nr.	Thickness $x10^{18}$ (at/cm^2)	Si (at. %)	H (at. %)	C (at. %)	O (at. %)	F (at. %)	Fe (at. %)
1	0÷7	88.3±3.6	7.8÷0.3	1.1÷0.2	1.2±0.2	1.5±0.3	-
2	0÷7	89.3±3.7	7.9±0.3	1.2±0.2	0.6±0.2	1.0±0.2	-
3	0÷2.8	69.3±3.5	24.8±1.2	3.9±0.7	1.0±0.4	1.1±0.4	-
3A	surface concentration	72±16	9±2	4±2.4	14±4	-	2±1.4
4	0÷4.2	69.4±1.1	26.4±0.9	2.5±0.7	0.3±0.2	1.6±0.5	-
4A	surface concentration	74±12	9±1.5	2.8±1.7	11.5±2.9	0.5±0.4	2±1.4
5	0÷5	67.9±1.0	28.3±0.8	2.1±0.5	1.0±0.3	0.6±0.2	-
6							
7	0÷4	66.5±3.3	30.7±1.5	2.1±0.5	0.5±0.2	0.7±0.3	-

Tab. 5.1.2: Elemental concentrations of the PS samples.

The results from the scraped off samples are designated in the table as 3A and 4A respectively. For these results, in contrast to the data for the other samples, it is not the volume average concentrations that are given but the elemental concentrations on the above-mentioned newly revealed surface.

5.1.5. Comments

The ERDA results deliver very important information about the distribution of the available elements throughout the depth of the sample. The best depth homogeneity of the elements' concentrations can be seen in thin (about 5 μm) mesoporous samples (fig.5.1.3-b). The ratio of about 8 at.% H to about 91 at.% Si retains its value through the whole measured thickness. The result for the freestanding configuration of the same structure is similar (fig. 5.1.3-a). The deviation of silicon concentration from the above-mentioned values near the surface can be explained as follows. The freestanding sample is measured from its upper face, where the polishing effect takes place. Because of the nature of this effect, an intermediate region accompanying the removal from the substrate exists. This region is formed by an enhanced current density and consequently hydrogen to silicon atom number ratio. In this region, the etching procedure is very intensive and, according to the model of Lehmann and Gösele, [see *Lehmann*] what can be expected is an increasing number of incorporated fluorine atoms. The latter explains the enhanced fluorine concentration in this intermediate region, which influences the average fluorine concentration in the whole sample.

For samples 3, 4 and 5 fig. 5.1.3 c), e), and g), it can also be said that there is a homogeneity to their composition until a certain depth is reached. These samples are

relatively thin (respectively about 1.7, 2.6 and 3.9 μm), which enables the incident ions to penetrate through the whole sample and thus reach the substrate. Together with the constant composition region of the sample, the presence of an intermediate region between the substrate and the sample where the concentrations continuously change from their values in the porous structure to those in the substrate can be seen.

Fig. 5.1.3-h) presents the result from the measuring of sample 6, which was prepared under the same conditions as sample A on Table I in the ref. [*Schuppler*]. It has to be mentioned that because the composition of the reported etching solution is not unambiguously indicated (in the third column of table I - "HF in ethanol" is shown as 20 % but in reality the etching solution consists of HF, ethanol and water and in that sense the water to ethanol ratio is not defined but is important for determining the mechanical properties of the porous structure), we have used a mixture as follows $HF:H_2O:C_2H_5OH=1:1:3$. The porous structure obtained is mechanically very unstable and, since the measuring conditions require the sample to be in a vertical position, a significant amount of the material drops out. In this way, the surface of the sample becomes uneven and unsuitable for a reliable measurement (see section 5.1.2.). Multiple attempts failed to resolve this problem. For this reason, the results obtained can be considered untrustworthy and inappropriate for any reliable comparison. The measurements taken from sample B in table I of the [*Schuppler*] ref. are reproduced in figure 5.1.3-i). All that was said in relation to the ambiguously indicated content of the etching solution for sample A is also valid for this sample: The thickness of the sample used for the ERDA experiment is greater than the penetration depth of the ions. The tendency of the silicon content to increase, and consequently the hydrogen content to decrease, in the region $0 \div 6.4\text{x}10^{18}$ at/cm^2 and the following stabilization of these quantities in the region $6.4 \div 9\text{x}10^{18}$ at/cm^2, are noticeable. A slope in the hydrogen and the silicon content and their ratio, similar to the ERDA results but performed with He^+ ions in the [*Schuppler*] reference, is observed in pictures 5.1.3-h) and 5.1.3-i). This spreads through a region greater than 3 μm and is not typical for the other porous silicon samples. Such a slope can't be explained as a reflection of the structure or as originating from the electrochemical or chemical etching. The only remaining explanation is some peculiarity of the experiment. For this sample, as for the type A sample, the structure is emphatically brittle. Probably as a result of the vertical position for measuring and the resultant formation of an uneven surface as a consequence of the very fragile mechanical structure, the sample is unsuitable for this kind of measurement. Ultimately, in our opinion, the observed slope reflects the measuring conditions

but not a change in the content. Table 5.1.2 shows that, except for Si and H, traces of carbon, oxygen and fluorine are also present immediately after the sample preparation. The results from FTIR measurements of similarly prepared samples exclude any presence of silicon oxide (SiO_x) in the samples shortly (about 2 hours) after the preparation (see section 8.2). In our opinion, the presence of oxygen atoms can be connected to hydroxyl $(-OH)$ or ethanol (C_2H_5O-) groups bound to silicon on the internal surface of the porous structure. Furthermore, residues of water (H_2O) and ethanol (C_2H_5OH), which are components of the etching solution (HF, C_2H_5OH, H_2O), may be captured in the pores. The availability of fluorine can be explained with the dissolution chemistry of silicon as the porous structure is formed [see *Lehmann*]. The fluorine ions F^- are presumably introduced by a nucleophilic attack mechanism at the silicon surface, where they replace the hydrogen. Another probable source is residues of hydrofluoric acid (HF) in the pores. The carbon is, similarly to the oxygen, an ingredient of the ethanol molecules or ethanol groups. Contamination by aliphatic hydrocarbons is also possible. There is data in the literature for the existence of such contamination [see *Grosman*]. The availability of about 3 : 1 carbon to oxygen atomic percent ratio in the results is evidence that such impurity is possible. A value of more than 2 : 1 of the above-mentioned ratio cannot be explained if the alcohol is the only reason for the carbon presence. The Fe contamination observed in samples 3A and 4A is due to the scalpel used for the scraping off of the samples from the substrate. There is, of course, B available as a doping material, but its concentration is of the order of hundredths of one percent and, having in mind the accuracy of the ERDA method, it doesn't have a significant influence on the results. Table 5.1.3 shows the values of the hydrogen to silicon atom number ratio extracted from table 5.1.2 and compared to the values obtained by using the combined gravimetry

Sample Nr.	**H/Si (at.%)**			
	ERDA		**Effusion+ Gravimetry**	**EXAFS [after ref. *Schuppler*]**
	This work	**After ref. *Schuppler***		
1	9		14	
3	36		43	
4	38			
5	42			
6			43	123
7	46(?)	125	42	114

Tab. 5.1.3: Comparison of H/Si atom number ratio values (in %) obtained by different methods for the samples on tab. 5.1.1.

and the thermal effusion and EXAFS methods for identically prepared samples.

A precise comparison of the data from the two experiments, ERDA and the combined gravimetry and thermal effusion, has to consider the distinctive features of each method. The ERDA measurement was carried out at room temperatures, assuring that the samples don't change their composition with respect to the content after the electrochemical preparation till the beginning of the measurement. The situation for thermal effusion at constant temperature is different. As a result of heating to 900 ^{o}C during the measurement, the Si-H bonds are broken and the released hydrogen is gathered in a container with a precisely determined volume. The total gas quantity is considered to be hydrogen and the non-volatile residue, the skeleton, is assumed to consist exclusively of silicon. The additional elements observed in table 5.1.2 generate a necessity to clarify their role and influence on the hydrogen to silicon atom number ratio. In our opinion, most of the oxygen, fluorine and carbon atoms leave the sample in the composition of the molecules of the above-mentioned compounds in the effusion experiment at constant temperature and are gathered with the hydrogen molecules in the measuring volume. In this way, the hydrogen to silicon ratio from the effusion experiment is overestimated. In the table, it can be seen that this overestimation is of the order of about 2 per cent, which lies within the measurement inaccuracy of the effusion method. In the EXAFS results, the hydrogen content is presumably overestimated (by a few%) because of the distinctive feature of this approach, which considers the dangling bonds to be hydrogen atoms (see chapter 6).

5.1.6. Conclusions

- There is a good agreement between the ERDA and the combined gravimetry and thermal effusion data for the mesoporous samples.

- There is a very good agreement between the ERDA and the combined gravimetry and thermal effusion data for the nanoporous samples produced as shown on tab. 5.1.1.

- There is a great discrepancy between the ERDA and the effusion data in this work and ERDA and EXAFS data reported in the Schuppler reference.

- In freshly prepared samples, there is no significant presence of oxygen or oxides.

References

1. *L'Ecuyer* J.L. L'Ecuyer, C. Brassard, C. Cardinal, J. Chabbal, L. Deschenes, J.P. Labrie, B. Terreault, J.G. Martel and R.S. Jacques, J. Appl. Phys. 47, 381

(1976).

2. *Dollinger1* G. Dollinger, A. Bergmaier, T. Faestermann, C.M. Frey, Fresenius J. Anal. Chem. 353, 311 (1995).
3. *Bergmaier1* A. Bergmaier, G. Dollinger, C.M. Frey, Nucl. Instr. and Meth. B 136-138, 638 (1998).
4. *Dollinger2* G. Dollinger, M. Boulouednine, A. Bergmaier, T. Faestermann and C.M. Frey, Nucl. Instrum. And Meth. B 118, 291 (1996).
5. *Frey* C. M. Frey, Thesis (Dissertation), TU Munich (1997).
6. *Bergmaier2* A. Bergmaier, G. Dollinger, C.M. Frey, T. Faestermann, Fresenius J. Anal. Chem. 353, 582 (1995).
7. *Schuppler* S. Schuppler, S.L. Friedman, M.A. Marcus, D.L. Adler, Y.-H. Xie, F.M. Ross, Y.J. Chabal, T.D. Harris, L.E. Brus, W.L. Brown, E.E. Chaban, P.F. Szajowski, S.B. Christman, and P.H. Citrin, Phys. Rev. B 52(7), 4910 (1995).
8. *Lehmann* V. Lehmann and U. Gösele, Appl. Phys. Lett. 58(8), 856 (1991).
9. *Grosman* A. Grosman and C. Ortega, in “properties of Porous Silicon”, EMIS Datareviews Series No.18, edited by Leigh Canham, (INSPEC, The Institution of Electrical Engineers, London, 1997), p.145.

5.2. The “Burning” method

A freestanding type of porous silicon sample has been examined using the highly efficient, fully automatic, vario EL elemental analyzer instrument for determining C, H, N, and S in the original sample. This device operates on the oxidative digestion method.

5.2.1. Principle

The substance to be analyzed is digested through oxidative combustion. The quantitative substance digestion is based on the principal of explosive combustion in an oxygenated helium-atmosphere in a combustion tube at a temperature of approx. $1150\,^{o}C$. Excepting molecular nitrogen, the oxidative combustion of the elements C, H, N, and S produces CO_2, H_2O, NO, NO_2, SO_2, SO_3 as well as volatile halogen compounds if the sample contains halogens. A reduction tube quantitatively reduces the nitrogen oxides and sulphur oxides at $850\ ^{o}C$ to molecular nitrogen and SO_2 while binding excess oxygen. The volatile halogen components are chemically bound by suitable absorbents and thus removed from the gas flow. The remaining gas mixture of helium, CO_2, H_2O, N_2, and SO_2 components is subsequently guided into a separation and measuring system. The components are separated in separation columns in accordance with gas-chromatographic principles. After this, they are separately, one after another, flushed by the carrier gas helium into the measuring module since the thermal conductivity detector (TCD) cannot specifically distinguish between the different components of the gas mixture.

5.2.2. Operation

The technical construction of the elemental analyzer is shown in the tubing scheme on fig. 5.2.1. The sample for digestion is weighted in a tin ‘boat’. The boat is folded into a cube shaped packet, sealed and inserted by means of an automatic sample feeder into the vertical quartz glass combustion tube. Parallel to the sample feeding procedure, the oxygen dosing begins in the ash finger via V4 and the oxygen lance so that the sample drops into a highly oxygenated atmosphere and combusts explosively to form the gas mixture. The oxygen-dosing amount is adjusted on the needle valve of the oxygen flow control. As the oxygen doses can be varied and the combustion times individually selected, quantitative combustion of the sample is also possible with large sample weights (up to $200\ mg$, according to the element content). All connecting tubes leading to the separation system are heated to prevent

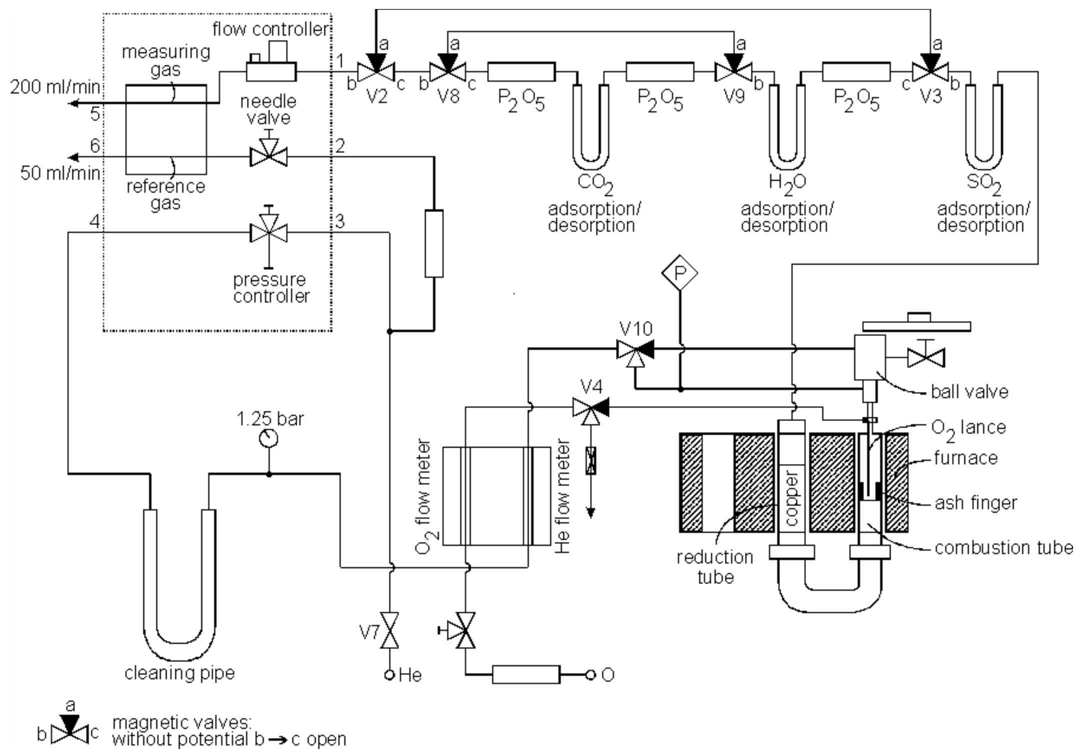

Fig. 5.2.1: Technical construction of the elemental analyzer.

H_2SO_4 being produced from SO_2 and H_2O and to avoid condensation occurring in the tube passages. A copper contact serves as a reduction tube. A suitable absorbent for the volatile halogen compounds is silver wool. The components of the gas mixture are separated in U-shaped separation columns. First, the mixture flows through an adsorption column at 140 ^{o}C. In this column, SO_2 is quantitatively removed. After this, the remaining gas flows through a second adsorption column. In this column, H_2O is quantitatively removed from the gas flow. Finally, the gas mixture consisting of CO_2, N_2 and helium flows through a third adsorption column. In this column, CO_2 is quantitatively removed from the gas flow. Nitrogen, which is unaffected by the adsorption columns, enters the thermal conductivity detector together with the helium carrier gas as first component. When the measurement of the nitrogen content is completed, the adsorption column charged with CO_2 is heated to approx. $130-150\ ^{o}C$ causing the CO_2 to be rapidly desorbed and then flushed with helium into the TCD. After the measurement of the CO_2 content is concluded, the H_2O adsorption column is heated to $150\ ^{o}C$. The H_2O bypasses the CO_2 adsorption column and is then flushed into the TCD. When the H_2O measurement is terminated, the SO_2 column will be heated up from its stand-by temperature $(140\ ^{0}C)$ to $210-220\ ^{0}C$ and the SO_2 will be flushed into the TCD, bypassing all other adsorption columns. After termination of the SO_2 measurement, the SO_2

adsorption column will be cooled down to 140 ^{0}C prior to a new analysis run.

5.2.3. Detection

A thermal conductivity detector (TCD) with improved sensitivity to the carrier gas helium serves as a detection module. The instrument measures differences in the thermal conductivity between one of the selected gases and helium. It consists of two chambers, each equipped with a thermistor. Helium passes through the one chamber at a constant rate of flow (reference flow), while helium and the foreign gas component due to be measured pass through the other chamber (measure flow). The two chambers constitute a measuring thermistor bridge and its electrical imbalance provides a direct gauge of the foreign gas content in the carrier gas. The detector output voltage coming from the thermistor bridge has a certain time variation with one maximum. The following diagram (fig. 5.2.2) shows a typical course of a measuring peak. The integral of this curve is proportional to the quantity of the selected gas. In order to integrate the curve, a voltage-to-frequency converter is used. This transforms the voltage into frequency and the value of the integral is the number of counts summed during the whole desorption process.

The absolute dynamic working range detection limits of the measured elements are presented in table 5.2.1.

5.2.4. Experimental results

Because of its nature, this method is suitable only for investigation of freestanding

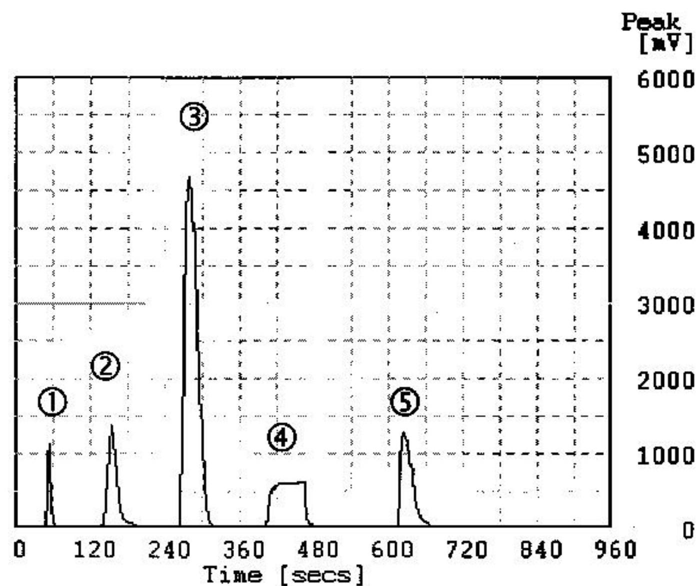

Fig.5.2.2: Typical course of measuring peak: 1.Detector fluctuations during sample feeding; 2.N_2-peak; 3.CO_2-peak; 4.H_2O-peak; 5.SO_2-peak.

Element	Limit [mg]	
	lower	upper
C	<0.0004	30
H	<0.0002	3
N	<0.001	10
O	<0.001	2
S	<0.005	2

Tab. 5.2.1: Absolute dynamic working range detection limits of the measured elements.

samples. Although the nanoporous structures, which we examined, are, in principle, feasible as a freestanding realization, their instability in air makes them inappropriate subjects for this kind of measurement. In contrast to these, the freestanding mesoporous structure is relatively easy to produce and stable when handled in air, thus fulfilling the essential requirements of the method concerning the samples.

Our aim has been to compare the hydrogen content and the hydrogen to silicon atom number ratio obtained by this method, if possible, with the same quantities given by the combined thermal effusion and gravimetric method. A series of three mesoporous samples has been investigated to determine the hydrogen content. All of the samples were composed of p^+ material (substrate resistivity $0.005 \div 0.020\ \Omega cm$), with an etching current density of $50\ mA/cm^2$ in an etching solution of $HF : H_2O : C_2H_5OH = 1:1:2$ in darkness. Only the etching times, and consequently the thickness of the samples, differed, as shown in tab. 5.2.2. The samples were handled following the standard drying procedure (see chapter 2.3.).

Sample Nr.	Etchtime	Thickness (μm)
1	4 min 24 sec	15
2	5 min 51 sec	20
3	7 min 19 sec	25

Tab.5.2.2: Etching time and thickness of the measured samples.

The next table, 5.2.3, presents the determined weight and the calculated atom concentrations for the elements available in significant amounts, to which this method is sensitive.

5.2.5. Comments

As the "burning" method is not sensitive to all elements, which the samples contain, and especially to silicon, it isn't possible to calculate the hydrogen to silicon atom ratio directly from the data obtained. The results delivered by ERDA measurements can be used as a

Sample Nr.	Weight (mg)	H		C	
		Content (mg)	Content (wt. %)	Content (mg)	Content (wt. %)
1	15.0633	0.067	0.4476	0.013	0.0881
2	16.1098	0.081	0.5028	0.009	0.0578
3	11.8432	0.071	0.5995	0.014	0.1206

Tab. 5.2.3: Determined weight and calculated concentrations of the measured elements.

source of the supplementary information, which is required for an estimation of the silicon content. Since these results are in the form of atomic concentrations and it isn't possible to convert the weight concentration of the hydrogen delivered from the "burning" method to atomic concentration because of the lack of information about the type and the quantity of all elements present in the sample, we will follow the next three steps to derive the wanted ratio:

- evaluation of the silicon atomic concentration in the considered samples;
- conversion of all atomic concentrations delivered by ERDA to weight concentrations;
- formation of the hydrogen to silicon weight ratio and its conversion into atomic number ratio.

Samples 1 and 2, presented on table 5.1.1 (see section 5.1.), were prepared under the same conditions as the samples considered here. Otherwise, the atom concentrations data shown in the table are volume averaged to derive the data, which this method delivers, and this makes the comparison plausible. Although the content values of samples 1 and 2 are very similar, we shall use those of the freestanding presentation (sample 1), whose sample was prepared in exactly the same manner as the samples in table 5.2.2. In table 5.1.2, it is seen that, except for the hydrogen and carbon established by the "burning" method, silicon, oxygen, and fluorine are also present.

The following equation expresses the conversion formula from atom % into weight % for a given element A in this porous structure:

$$\mathbf{A}(\mathrm{wt.\%}) = \frac{\mathbf{A}(\mathrm{at.\%})\mathbf{a}}{\mathbf{Si}(\mathrm{at.\%})\mathbf{si} + \mathbf{H}(\mathrm{at.\%})\mathbf{h} + \mathbf{C}(\mathrm{at.\%})\mathbf{c} + \mathbf{O}(\mathrm{at.\%})\mathbf{o} + \mathbf{F}(\mathrm{at.\%})\mathbf{f}} \quad (5.2.1)$$

where $\mathbf{si} = 28.086, \mathbf{h} = 1.008, \mathbf{c} = 12.011, \mathbf{o} = 15.999, \mathbf{f} = 18.998$ are the relative atomic weights of the corresponding elements and $\mathbf{a}$ is the same quantity of the considered element. If we take as a basis the data of sample 1 in table 5.1.2 (see section 5.1.), the calculated concentrations are: silicon – about $97.30\ \mathrm{wt.\%}$, hydrogen – about $0.31\ \mathrm{wt.\%}$, carbon – about $0.52\ \mathrm{wt.\%}$, oxygen – about $0.75\ \mathrm{wt.\%}$ and fluorine – about $1.12\ \mathrm{wt.\%}$.

It can be seen that the calculated weight concentrations obtained by the ERDA method

differ from the values delivered by the "burning" method (see tab. 5.2.3). For hydrogen, the "burning" method gives a higher concentration; up from about $45\,\%$ (sample 1) to about $93\,\%$ (sample 3) and for carbon – a lower concentration of about one quarter (sample 3) to about one ninth (sample 2).

The obtained silicon concentration of $97.3\,\text{wt.\%}$ can be compared with the silicon concentrations converted into weight $\%$ for the nanoporous samples 3, 4 and 5, presented in tab. 5.1.2. The calculations according to eq. 5.2.1 give the values of – $95\,\%$ (sample 3), $95.5\,\%$ (sample 4) and $95.9\,\%$ (sample 5) respectively. The gravimetric method considers the silicon weight concentration to be about $100\,\%$. For the oxygen and fluorine, elements for which the "burning" method isn't sensitive, the summary concentrations are as follows – $1.8\,\text{wt.\%}$ (sample 3), $1.8\,\text{wt.\%}$ (sample 4) and $1.4\,\text{wt.\%}$ (sample 5). For the freestanding mesoporous sample, the last quantity is about $1.9\,\text{wt.\%}$. The ERDA results, like those from the combined effusion and gravimetric methods, manifest a tendency towards silicon content enhancement at a transition from a nanoporous to a mesoporous structure. In conclusion, all available data justify the assumption that the silicon weight concentration is in the interval of $97-98\,\text{wt.\%}$.

The following equation expresses the conversion from weight % to atom number % for the ratio of two elements **A** and **B**

$$\frac{\mathbf{A}(\text{wt.\%})}{\mathbf{B}(\text{wt.\%})}\frac{\mathbf{b}}{\mathbf{a}} = \frac{\mathbf{A}}{\mathbf{B}}(\text{at.\%}), \qquad (5.2.2)$$

where $\mathbf{a}$ and $\mathbf{b}$ are their relative atomic weights respectively.

If we construct the hydrogen to silicon weight $\%$ ratio, supposing a value of 97.5 wt.% for silicon and apply eq. (5.2.2) for the considered samples 1, 2 and 3 (see tab. 5.2.3), it leads to values of about 13 at.%, 14 at.% and 17 at.% respectively for the hydrogen to silicon atom number ratio. The last values correspond very well to the values, which the combined effusion and gravimetric method gives for the samples prepared under the same conditions (see tab. 5.1.3 in section 5.1.2).

5.2.6. Conclusions

- The "burning" method is applicable only for mesoporous freestanding samples.
- It is not possible from the delivered data to determine the hydrogen to silicon atom number ratio directly.
- Assuming a silicon weight concentration of about $97.5\,\text{wt.\%}$ (using ERDA data) for the

considered mesoporous samples, the values for the hydrogen to silicon atom number ratio calculated on the basis of the hydrogen weight concentrations obtained are in very good accordance with the measured values delivered from the combined effusion and gravimetric methods for porous structures prepared under the same conditions.

Chapter 6. EXAFS FOR THE H/SI ATOM RATIO DETERMINATION

6.1. EXAFS analysis: principles and accuracy

Extended X-ray Absorption Fine Structure (EXAFS) is a powerful investigation method that gives as main information the distance from a reference atom to its first order neighbors, the so-called first coordination sphere.

The principle of investigation is the following:

a) The extraction energy of an electron from for example the K-shell to the unbound state (theoretically infinite distance from atom) is independent on the host crystal and therefore well defined. By scanning the X-ray energy around this value, one observes a clear edge in the absorption spectrum.

b) A more detailed i.e. with higher resolution analysis of this absorption spectrum, above the absorption edge, shows some irregular oscillations at the first glance.

c) The origin of these oscillations is linked with quantum interferences of the free electrons extracted by the X-ray photons. The energies in consideration are very small compared with the excitation energies (~10 keV), however, very large compared with usual band gaps in condensed matters (E > 10 eV). There are of interest in these experiment only electrons having a better localization than the distance between two atoms. Therefore their mass is not influenced by the lattice and is $m=m_0$.

d) The free electrons have an additional kinetic energy resulted as difference between the photon X-Ray energy and the extraction energy (absorption edge). Then the momentum and the correspondingly De Broglie wavelength is given by:

$$E_K = \frac{mv^2}{2} = \frac{p^2}{2m} = \frac{\hbar^2 k^2}{2m} \Rightarrow k = \frac{2\pi}{\lambda} = \frac{1}{\hbar}\sqrt{2mE_K} = \frac{1}{\hbar}\sqrt{2m(E_X - E_{abs})}$$

e) Therefore, a useful transformation of the scale is that from energy (E_X) to the k vector. One expects resonances when $kd=n\pi$. Here d is the distance between two atoms and n is an integer. The physical meaning of these resonances comes from the fact that electrons are reflected from the neighbor atoms being at distance d. If this distance is an integer multiple of the electron half wavelength then occurs a resonant multiple reflection that physically means a higher density of charge in the region between the 2 atoms than usual. The consequence of this is a stronger scattering of the X-rays i.e. less transmitted X-ray signal through the sample.

f) Therefore, using the k vector as x-axis and considering simplified only reflections from the first neighbor (only one d), one expects a periodic oscillation of the X-ray transmitted

signal. The Fourier transform of this oscillation will give unambiguously a sharp maximum at the distance *d* in the real space.

g) Two things alter the perfect periodicity of the signal.

g.1) The electrons collide partial inelastically with the neighbor atoms, losing a part of their kinetic energy. This leads to a small change of the wavelength, or, in terms of a resonance, they change their phase out of π. Therefore, a resonance is not infinitely sharp. The total distance traveled by the electron back and forth until the wave doesn't add constructively anymore (the sum of dephasing is π/2) is called in this context mean free path λ. The magnitude λ is hence associated with the quality factor of the resonance: $Q = \frac{\lambda}{d} = \frac{1}{\Gamma}$. Γd is the full width half maximum of the resonance. In the absence of the resonant multiple scattering between two atoms, the electrons travel through the lattice suffering many partially inelastic collisions until they lose completely their energy and are absorbed. In the field of X-ray interaction with the condensed matter, this is the general definition of the mean free path. This magnitude depends on the initial kinetic energy of electrons and is directly measurable. For EXAFS estimations, it is usually this later value of mean free path taken and considered as approximately the same with that defined before.

g.2) The transmitted X-ray signal is modulated by a sum of many resonances given by all the atoms present in the X-ray beam. The distance between two atoms is not always the same. Temperature i.e. lattice vibrations shift the center of single resonances. This does not influence so much the width but the intensity of the total resonance. Quantitatively this change in intensity is given by the Debye-Waller-factor: $\exp\left(-\frac{k_B T G^2}{M\omega^2}\right)$. Here *G* is a reciprocal lattice vector, *M* the mass of the atom and ω the vibration frequency; optical phonon frequency being a suitable reference value. In terms of EXAFS by constant temperature, the *k* vector for different resonances is just a reciprocal lattice vector. Therefore the Debye-Waller-factor is expressed simplified as: $\exp\left(-2\sigma^2 k^2\right)$. In conclusion, σ expresses the disorder in the lattice. Especially for the case of amorphous or porous materials, the disorder may have a different origin than that induced by temperature. Just this is the point of our critical analysis. In the moment when we count the intensity of the Fourier transformed EXAFS peak and not only its position, then a special consideration has to be given to all possible lattice distortions.

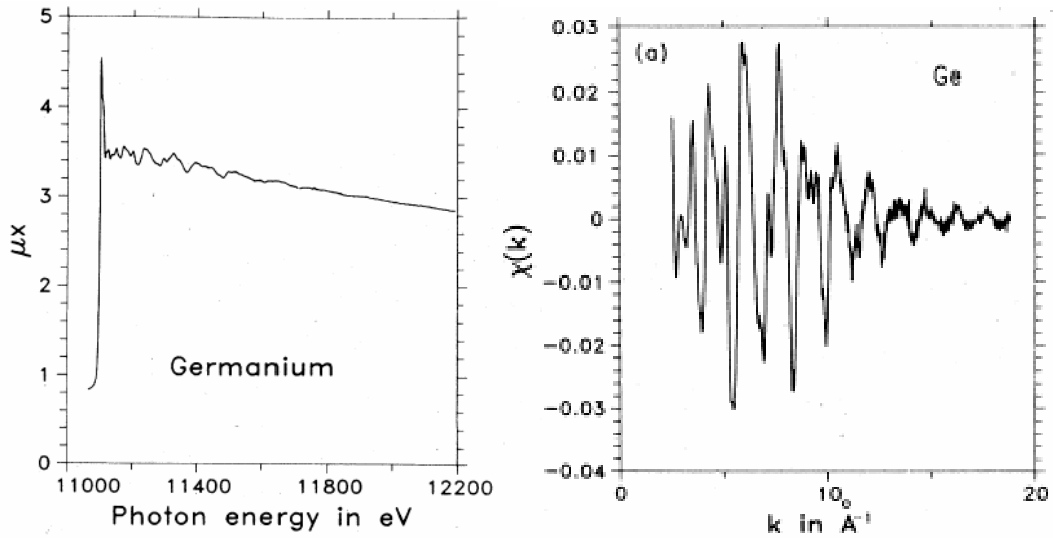

Fig.6.1: Absorption spectrum of (100) Ge at 100 K (left). Modulation part of the absorption as a function of *k* vector (right) [after *Lee*].

6.2. Data processing. Mean number of neighbor atoms.

Let's consider the example of X-ray absorption in germanium presented in fig.6.1.- left. Above approx. 11 keV it appears a stronger absorption due to extraction of electrons from the K-shell. After this edge it is an oscillatory variation of the signal. If one subtracts the background given through extrapolation by the straight line from the right side of the graphic and stets the zero energy the edge energy, one can replot the modulation of the absorption as a function of *k* vector as described in the previous section, (see fig.6.1.- right). Already in this picture, one can see the periodicity of the signal and also the quasi exponential decay of the envelope. An exponential decay will contribute to an enlargement of the peak in the Fourier transform. This may alter the peak position as well. It was found a suitable empirical rule that compensate partially the decay, namely by multiplying the signal with k^3.

The transformed modulation spectrum and the corresponding Fourier transform are shown in fig.6.2. The main message of fig.6.2- right is the position of the peak at ~2.1 Å, telling that atoms situated on the first coordinate sphere are 2.1 Å far from the central atom. The lattice constant of Ge is 5.66 Å. Therefore, the radius of the first coordinate sphere should be $\frac{1}{4}\sqrt{3}\cdot 5.66 = 2.45$ Å. The discrepancy comes mainly from the partial inelastic scattering of electrons on atoms.

Let us consider now the meaning of the intensity of the peak centered at 2.1 Å. There are *two* numbers behind this peak: (1) the *density* of Ge atoms that gives the amplitude of the background (fig.6.1- left, the smooth variation) and (2) the *number* of Ge-Ge *pairs* relative to the number of Ge atoms. In order to make a fair comparison between bulk, amorphous and

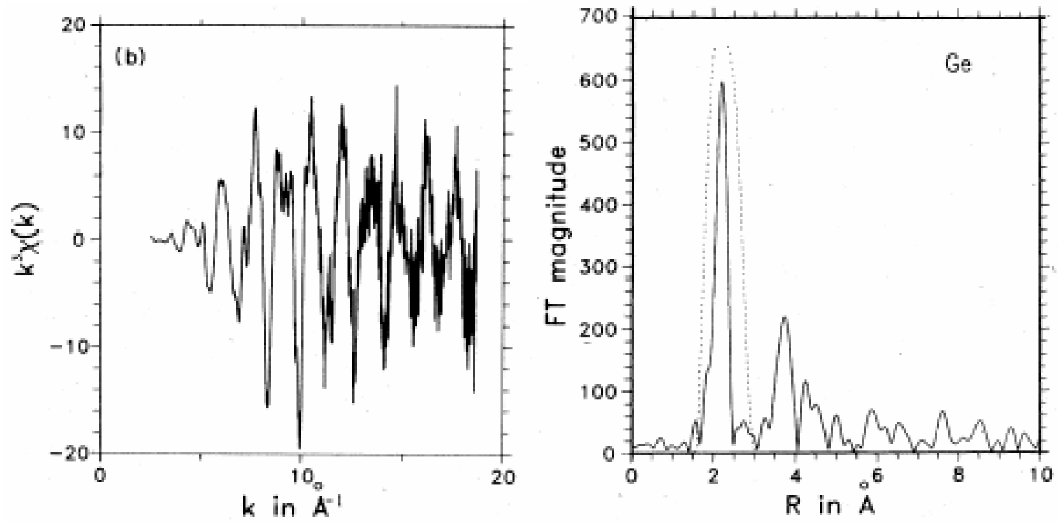

Fig.6.2: Transformed modulation spectrum by multiplication with k^3 (left) and its Fourier transform (right) [after *Lee*].

porous materials, one has to *rescale* first the background (and consequently the oscillatory part) to the level of the bulk. In this case, a smaller intensity of the peak for a porous material or more precise the ratio of the peak intensity of porous to that of bulk material means quantitatively a smaller number of Ge-Ge bindings relative to *the same density* of atoms.

6.3. Case of bulk, amorphous and porous silicon

Schuppler *et al*. studied in detail with help of EXAFS the hydrogen content in porous silicon and, as result, the size dependence of the photoluminescence. The raw data as presented in the paper of Schuppler [see *Schuppler*] are shown in fig.6.3-left. A homemade extraction of the modulation part multiplicated by k^2 as indicated by Schuppler (not k^3 like for Ge) appears in fig.6.3-right. The Fourier transform of the variations in fig.6.3-right are presented in fig.6.4-left.

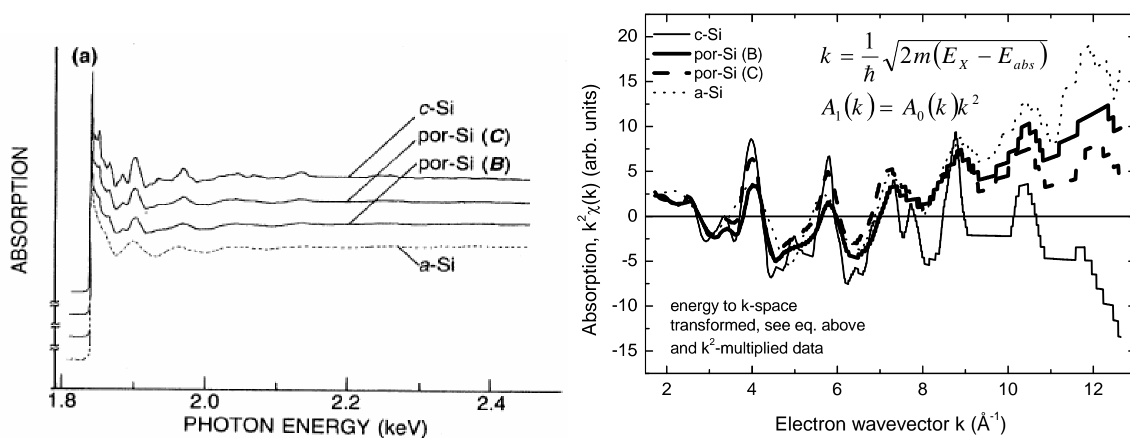

Fig.6.3: Absorption spectrum at K edge of bulk, porous and amorphous Si at 77 K (left). Modulation part of the absorption as a function of k vector after multiplication with k^2 (right) [after *Schuppler*].

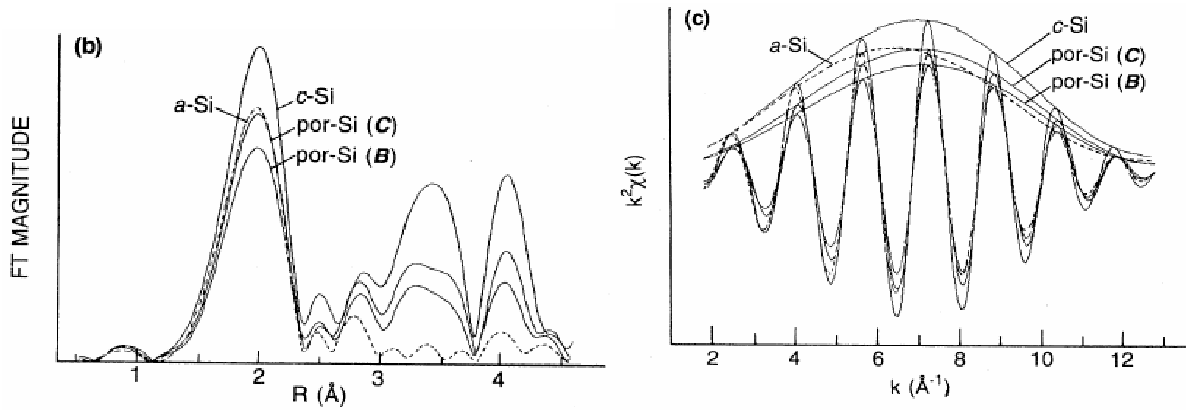

Fig.6.4:(left) Fourier transform of the spectra presented in fig.6.3-right. Back Fourier transformation of a window between approx 1.5 Å and 2.5 Å (right) [after *Schuppler*].

At this point one has to draw the attention of the reader. The authors [Schuppler *et al.*] ignore completely the resolution of the Fourier transform, namely $\Delta k \times \Delta R \geq 1/2$. To be more precise, the equality exits only for a Gaussian variation, however, for a rectangular window the product exceeds 2! The investigated energy range is from 1.85 until 2.5 keV. To this corresponds a variation of the *k*-vector from zero until 12 Å^{-1}. The range 0-2 Å^{-1} contains additional contributions (see NEXAFS, the same paper) and therefore is not considered. For a Δk=10 Å^{-1} and a rectangular window, one get an uncertainty of ΔR=0.2 Å. Therefore, the small oscillations, easy visible for a-Si in fig.6.4-left, are artifacts! The peaks at 2.5 Å, 2.8 Å or at 4.4 Å are *not linked* to some coordination spheres. The authors should have used the Fast Fourier Transform (FFT) algorithm that gives a minimum of points, strictly linked to the physically available information.

The authors are doing even the second step. They consider the *shape* of the peak at about *R*=2.0 Å as accurate, they chose a window between 1.5 and 2.5 Å and compute the back transform. In order to understand the purpose of this action one has to have in mind the Lorentz curve and its Fourier transform, i.e. an exponentially damped oscillation. The FWHM of the resonance curve gives the exponential decay rate. The resolution of the back transformation is given by Δk=2 / ΔR≈1 Å^{-1}. This means that the amplitude of each maximum might be affected by this resolution. Regarding again the fig.6.4-left it is hard to distinguish a change of the FWHM for a-Si (amorphous) or por-Si (porous) relative to c-Si (crystalline / bulk), especially having in mind the discussed accuracy and artifacts. The authors draw an envelope of the oscillations presented in fig.6.4-right and they conclude that only the signal from amorphous silicon decays quicker i.e. there is a bigger coefficient σ or, physically expressed, disorder exists only in amorphous silicon. The fig.6.4-right brings to the authors the key information in interpretation of the porous silicon data, namely σ is *the same* like in bulk silicon, based on the argument that the both envelopes have the maximum at the same

position. Consequently, the silicon atoms being on the surface of porous silicon and having one till three hydrogen bonds should sit at *exactly the same position* like in bulk.

Based on this tacitly done statement they conclude that the hydrogen concentration is huge and consequently the size of the particle is much smaller than expected. The determined ratio hydrogen / silicon content is approx. 3 times higher than in the present work. In sample B for example the average number of Si-Si bonds is $\overline{N}_{Si} = 4 \times \frac{I_{por\ Si\ B}}{I_{c-Si}} = 2.86$ instead of 4. Therefore, in average *each* silicon atom (from bulk *and* surface) is bound to 4 - 2.86 = 1.14 hydrogen atoms. The present work showed that samples produced in the same conditions like in the cited paper that presumably have nanoparticles with the same size, have hydrogen to silicon ratio of only 0.42.

6.4. Influence of the surface reconstruction on the EXAFS signal.

In order to explain the discrepancy between these two results we consider that the Si-Si bonds to the surface atoms are distorted due to charge redistribution. Hydrogen is more electropositive than Si (it accepts easier an electron than Si can give) therefore the density of charge in the Si-H bond is higher than in the Si-Si bond. The consequence of this redistribution is that the remaining Si-Si bonds are shorter. A similar effect has the Si-Si bridge (double bond) in the case of the surface reconstruction of crystalline Si. Macroscpically regarded it appears a superficial tension. The consequence of this bond length redistribution is the reduction of the EXAFS signal.

The principle of summation in our simulation is shown in fig.6.5. In case of a perfect, bulk lattice (fig.6.5-a), all the bonds have the length R_0. Each bond represents a resonance with the same width; because they are centred at the *same* R_0, finally each bond will contribute with one unit to the EXAFS sum signal. On contrary, a distorted lattice (fig.6.5- b) means resonances placed at different positions near R_0. A bond will contribute with *less* than one unit to the EXAFS sum signal.

In our model [see *Leinweber*] we consider nanoparticles with a spherical shape. For simplicity, the centre of the sphere is one point of the lattice. Surface atoms are those which have at least one cut bond. Due to the etching process, each cut Si-Si bond is transformed into a Si-H bond. Si-Si double bonds require a higher formation energy. Tab.6.1. shows the correspondence between different diameters of nanoparticles, the content of Si atoms and the number of simple, double and triple terminations.

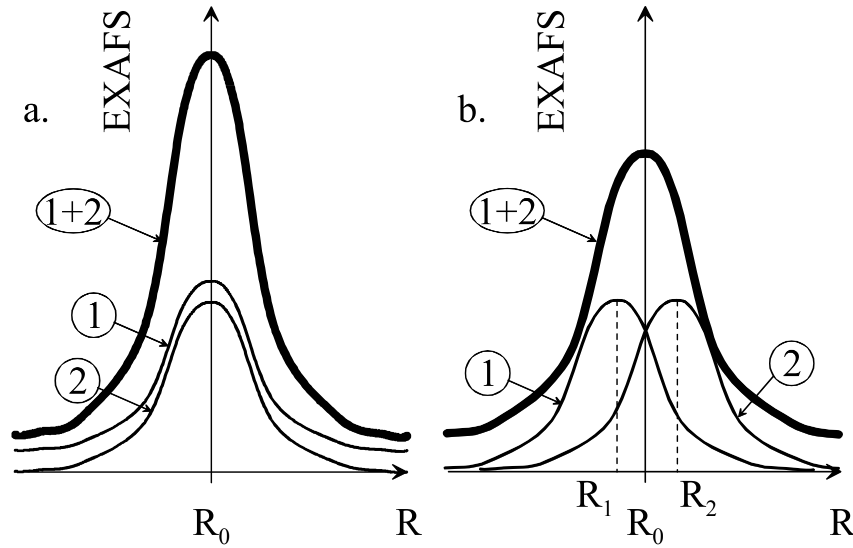

Fig.6.5: Addition of EXAFS resonances in a crystalline lattice (a). Addition of EXAFS resonances in disordered lattices (b).

The example that is the closest to the “sample B” of Schuppler and “sample 7” of this work is that of 30 Å diameter nanoparticles. Each of such nanoparticles have totally 300 hydrogen atoms, 705 silicon atoms. 228 Si atoms are at the surface. 156 have one H bond, 72 have two H bonds, and 0 have 3 H bonds. Totally, there are 1560 bonds, from which 300 Si-H bonds and 1260 Si-Si bonds. From these, 486 Si-Si bonds are toward a surface silicon atom and are expected to have a changed length.

The random way of bond distortion is described in fig.6.6. Each atom having at least a cut bond (i.e. a Si-H bond) is a surface atom and it is supposed to be displaced. The new position is on a semisphere oriented toward the centre of the nanoparticle. The radius is given by a Gaussian distribution with the mean value αR_0 and the mean square deviation also αR_0. R_0 is the length of the Si-Si bond in bulk crystals, $R_0 = \frac{1}{4}\sqrt{3}\cdot 5.43 = 2.35$ Å. (To remark that the

Diameter (Å)	Surface Si atoms			Nr of Si atoms N_{Si}	ratios	
	SiH	SiH_2	SiH_3		N_H/N_{Si}	N_{Si}/N_H
10	12	12	0	29	1.24	0.80
20	52	24	16	191	0.77	1.30
30	156	72	0	705	0.42	2.38
40	244	156	24	1707	0.37	2.72

Tab.6.1: Numbers of Si atoms, Si-H bonds, and hydrogen-to-silicon-ratio for different diameters of nanoparticles.

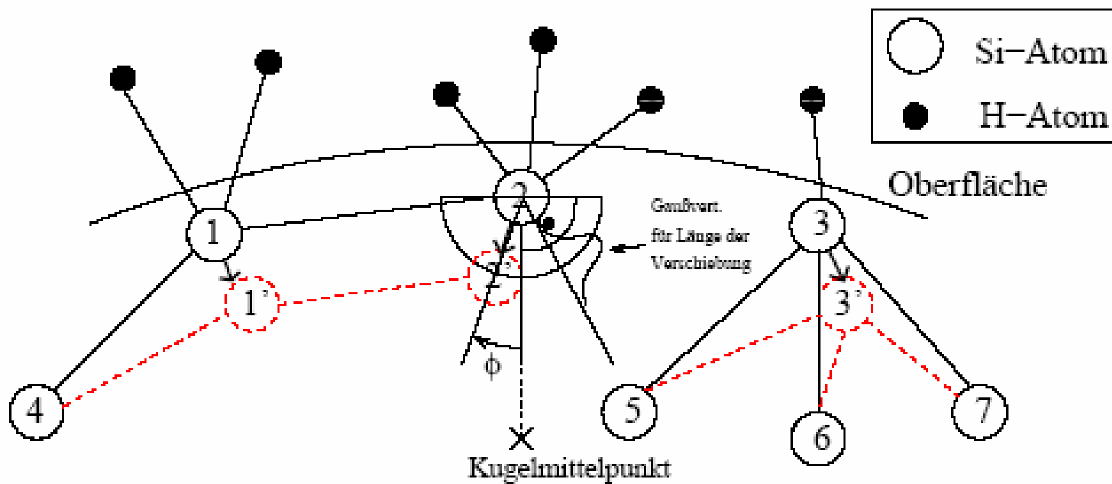

Fig.6.6: Displacement of the surface silicon atoms.

measured EXAFS peak is centred at 2.0 Å instead of 2.35 Å. The error has the same origin like for Ge.) The new position of each surface Si atom determines changed lengths of the bonds. The random deviation of these bond lengths is presented in fig.6.7-top for one particular case, where α=0.15. In order to make statistics for the bond length (α was linked to the random *position* of the atoms) we made a histogram of these bonds and we determined the mean square deviation, σ of their length. This number is slightly smaller than α, $\sigma \approx 0.1$ for $\alpha = 0.15$, see fig.6.7- bottom.

The width of each single resonance is given by the mean free path λ. Fig.6.8-top shows an example for $\lambda = R_0 / 0.15$=15.67 Å i.e. $\Gamma = R_0 / \lambda = 0.15$. This means a FWHM of the resonance of $\Gamma\ R_0 = 0.35$ Å. Fig.6.8-bottom shows again the cited Fourier transform of the EXAFS signal as presented by Schuppler (see fig.6.4-left). The peak is obviously not Lorentzian. We tried to decompose the peak corresponding to the first coordination sphere, marked with red, in a minimum number of Lorentz curves (green). The FWHM of each is between 0.07 and 0.22 Å, in all cases being smaller (more favourable) than in the chosen example. The Fig.6.8-top shows 3 cases: the EXAFS signal for a bulk and single crystal of Si (black), the signal of porous silicon as ideal cut from a bulk (red), and the real porous material with the same number of Si-H bonds as in the previous case, however, with distorted bonds and displaced atoms.

Fig.6.9. shows an overview of the EXAFS intensity for different mean free paths and distortion coefficients σ. The limit σ=0 corresponds to the ideal case in which the EXAFS signal gives directly the correct hydrogen to silicon ratio. The value 2.86 is the detected EXAFS intensity for nanoparticles with this size. The asymptotic limit 2.25 corresponds to the case of total distortion in which the bonds to the surface Si atoms have no contribution to the EXAFS intensity. One can see that for a mean square deviation of 15 % of the bond length

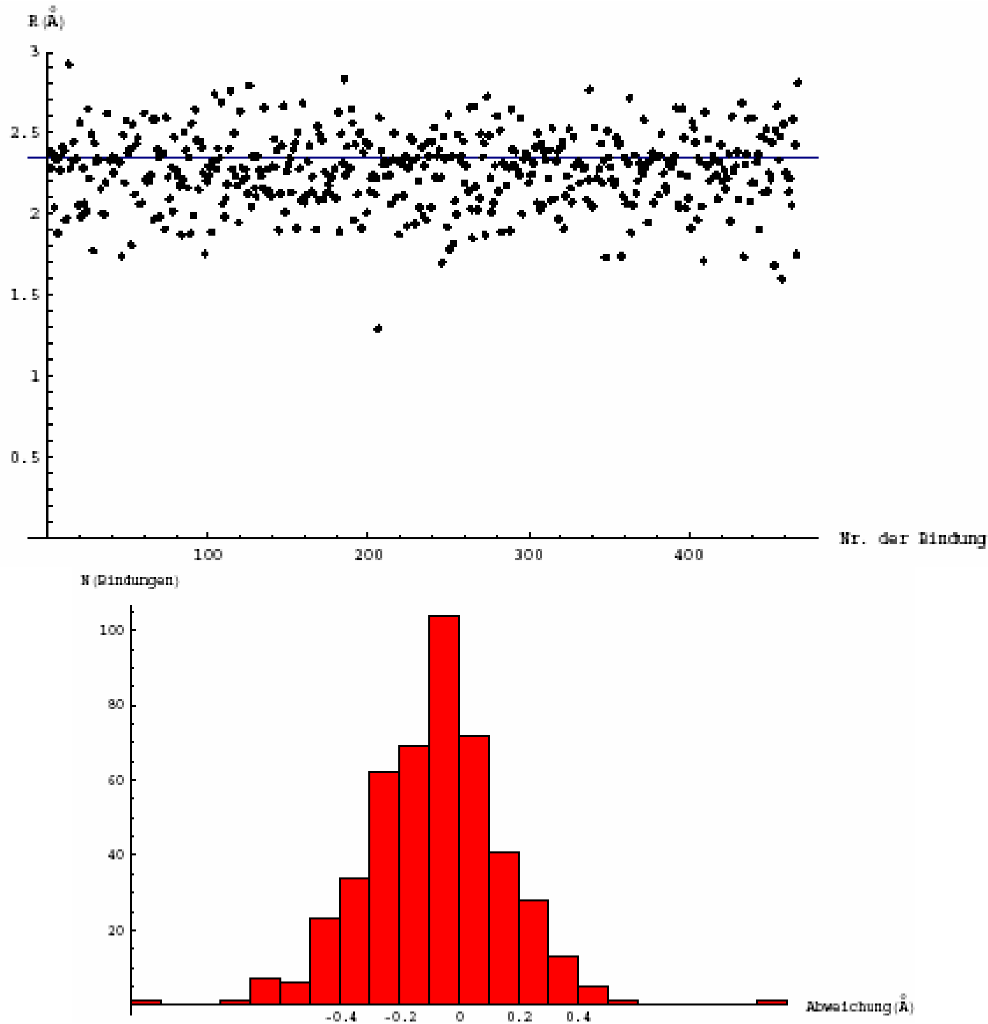

Fig.6.7: Random values of each of of the 486 bonds toward surface Si atoms for α = 0.15 (top). Histogram of the *changed* bonds (bottom). They are in average shorter (mean value = $R_{med} - R_0 < 0$) and the mean square deviation is σ ≈ 0.1.

and a mean free path of ~16 Å (Γ=0.15), both physically realistic values, one can reproduce the measured EXAFS intensity in spite of a hydrogen to silicon ratio of 0.42.

6.5. Conclusions

-EXAFS measurements give only a qualitative answer of to the ratio H / Si in porous silicon.

-Even the distance to the nearest neighbour is altered by inelastic scattering.

-Distortion of the surface bonds may influence dramatically the EXAFS intensity, although the inner part of the nanoparticle is still crystalline.

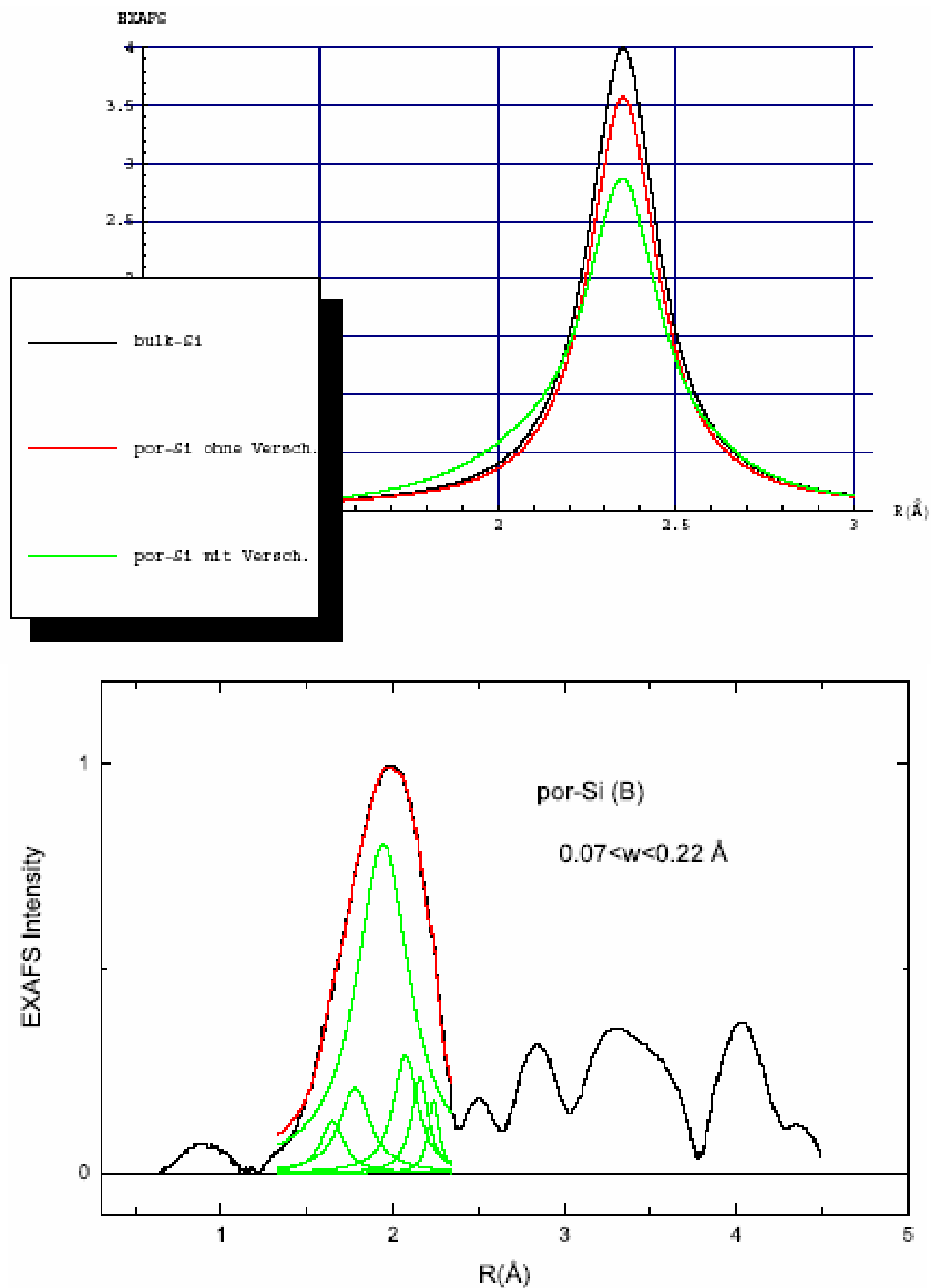

Fig.6.8: (top) EXAFS resonance for bulk (black) and porous silicon with (green) and without (red) distortion of the surface bonds (bottom).

References

1. *Lee* P.A. Lee, P.H. Citrin, P. Eisenberger, and B.M. Kincaid, Rev. Mod. Phys. **53**(4), 769 (1981).
2. *Schuppler* S. Schuppler, S.L. Friedman, M.A. Marcus, D.L. Adler, Y.-H. Xie, F.M. Ross, Y.J. Chabal, T.D. Harris, L.E. Brus, W.L. Brown, E.E. Chaban, P.F. Szajowski, S.B. Christman, and P.H. Citrin, Phys. Rev.B **52**(7), 4910 (1995).
3. *Leinweber* M. Leinweber, Project TUM, 2004.

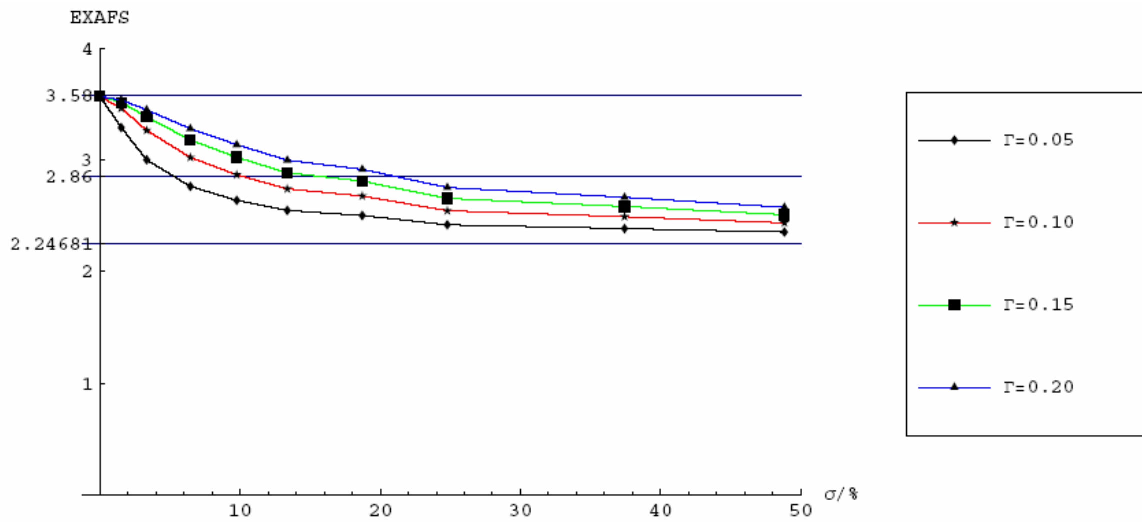

Fig.6.9: Variation of the EXAFS intensity as a function of mean free path ($\lambda = R_0 / \Gamma$) and distortion coefficient σ.

Chapter 7. THE RELATIONSHIP BETWEEN LUMINESCENCE AND THE H/SI ATOM NUMBER RATIO

The optical properties of porous silicon, and especially its photoluminescence, have made this medium of interest to investigators. It is known from the literature [see e.g. *Koch*] that efficient luminescence from porous silicon structures occurs in the near infrared (IR) region, in the whole visible range and in the near ultra-violet (UV) region. This broad range of emission energies arises from clearly distinct luminescence bands. The IR band is weak at room temperature but becomes stronger at cryogenic temperatures. Its origin seems to be related to dangling bonds. The blue band is observed only in oxidized samples. For the current consideration, the visible luminescence is of greatest importance because it is due to exciton relaxation and gives the possibility that the band gap width of the porous structure might eventually be evaluated from the position of the luminescence maximum in this spectral region.

The aim of our investigations is to establish a correlation between the hydrogen to silicon atom number ratio and the position of the visible luminescence peak for the porous silicon samples under consideration. This position has been chosen as a universal basis for the comparison of porous structures, which have been produced under different conditions by different research groups.

7.1. Experimental conditions

The luminescent behaviour of the samples was studied on a Perkin Elmer LS 50B Luminescence Spectrometer at room temperature in the visible region with an excitation wavelength of 350 nm and at 1.4 K temperature in the near infrared region on appropriate equipment for luminescence experiments in the optical laboratory of our institute. The resolution was 2 nm (for the region around 600 nm, this corresponds to about 0.01 eV). The samples were properly handled and measured immediately after their preparation in order to avoid oxidation (see section 2.3.).

7.2. Experimental results

The luminescent properties of almost all samples discussed in section 4.3., arranged into groups after being produced in the same manner, have been investigated. The following fig. 7.1 gives the experimental results for the dependence of the luminescence peak position

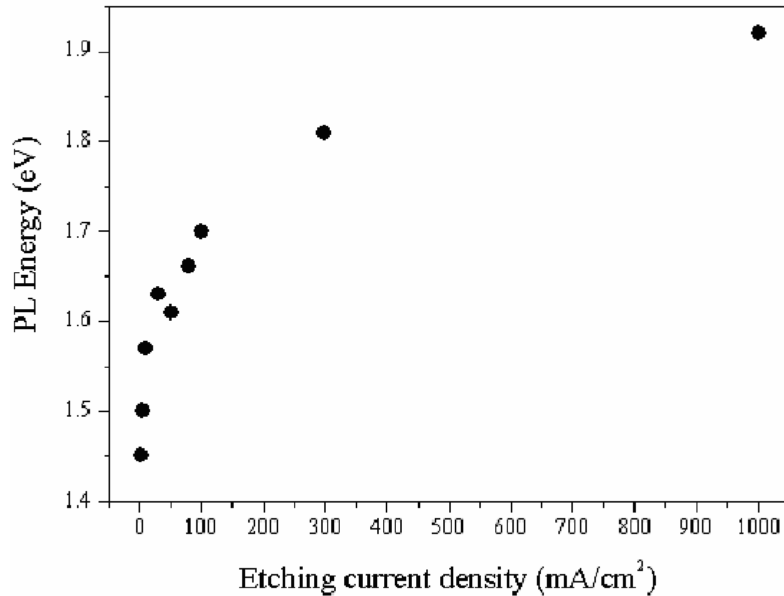

Fig.7.1: Position of the luminescence peak vs. etch-current density.

versus the etching current density.

The considered position depends very strongly on the substrate doping; at least when it concerns the difference between porous structures produced on highly and moderately doped substrate material. Fig. 7.2 shows the luminescence curves for a sample produced on a p+ substrate (resistivity $5\ \mathrm{m\Omega cm}$) by a $50\ \mathrm{mA/cm^2}$ etching current density and with a standard etching solution (see section 2.3.) measured at $T = 1.4\ \mathrm{K}$ and a sample produced on a moderately doped p^- substrate (resistivity $5\ \Omega\mathrm{cm}$) by the same etching solution and $1\ \mathrm{mA/cm^2}$ etching current but measured at room temperature.

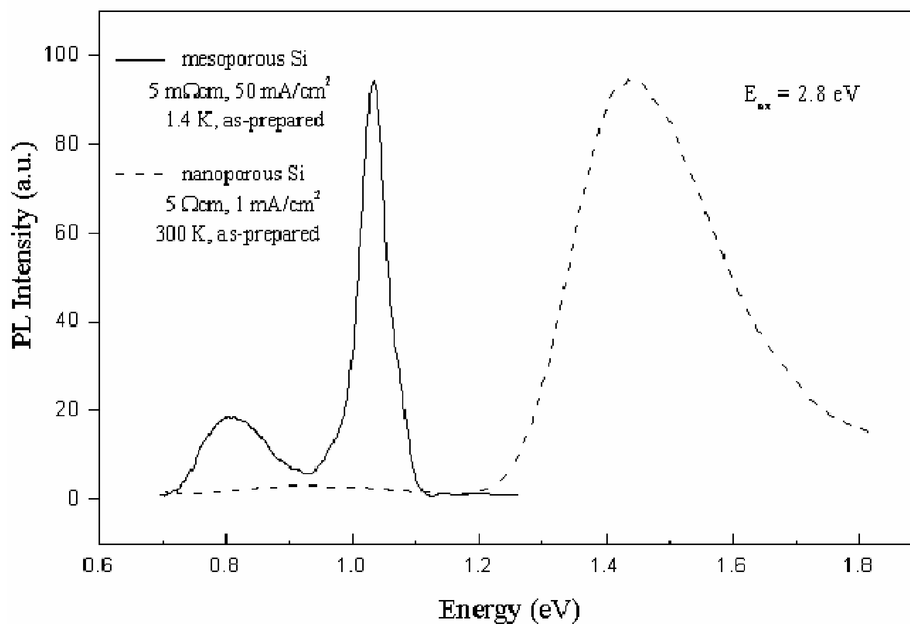

Fig.7.2: Comparison between luminescent curves of meso- and nanoporous structures.

The luminescent results from the `post-etching´-series obtained at room temperature have shown no shift of the luminescence peak. In our case, its position was the same as the one shown on fig. 7.2 for the nanoporous material.

The blue shift of the luminescence for samples produced under illumination by using a set of low-pass filters is illustrated on fig.7.3. The dependence of the luminescence peak on the minimum wavelength of the incident light, determined by the utilized filter, is clearly seen.

The influence of oxidation on the luminescence peak position is illustrated on fig.7.4.

7.3. Comments

The results from the series with differing etching current densities have shown a tendency towards a higher energy shift of the luminescence peak position with the increase of current density. As a whole, this result is in accordance with reports in the literature [see *Lehmann, Muschik, Mehra*] but there are discrepancies concerning some of the concrete values. The first two cited authors investigated samples, which were produced under conditions comparable to those for our samples, and this justifies the comparison. These authors considered a wide interval of current densities commented upon below. In our work, that interval was determined by the condition that the produced samples be suitable for effusion measurements. Because of this, the utilized current densities comprise values that mainly lie between

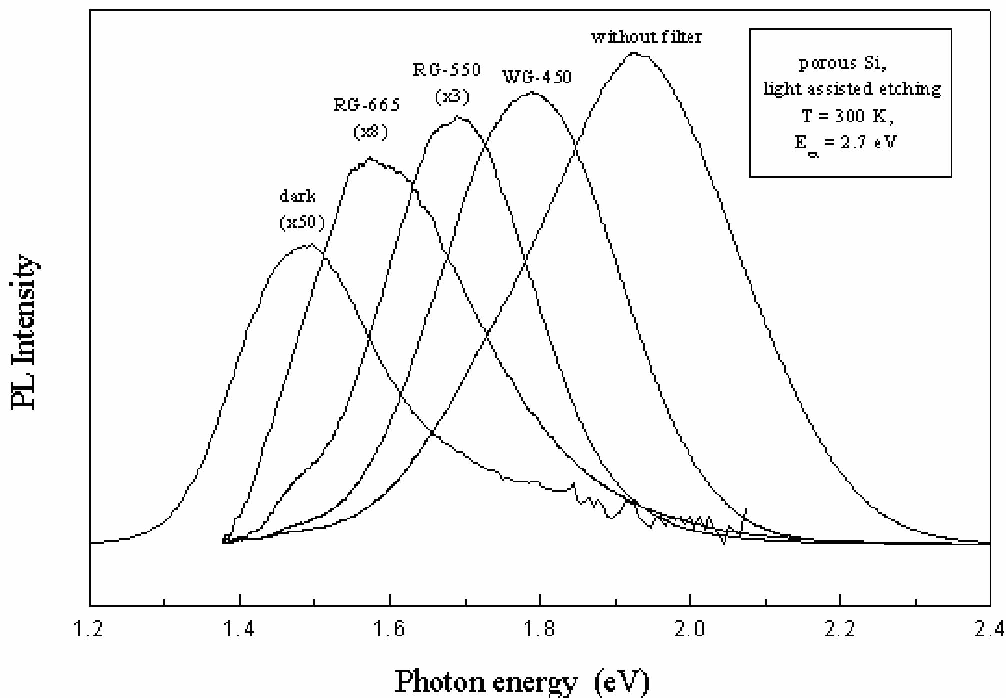

Fig.7.3: Blue shift of the luminescence in samples, produced under illumination by using different low-pass filters.

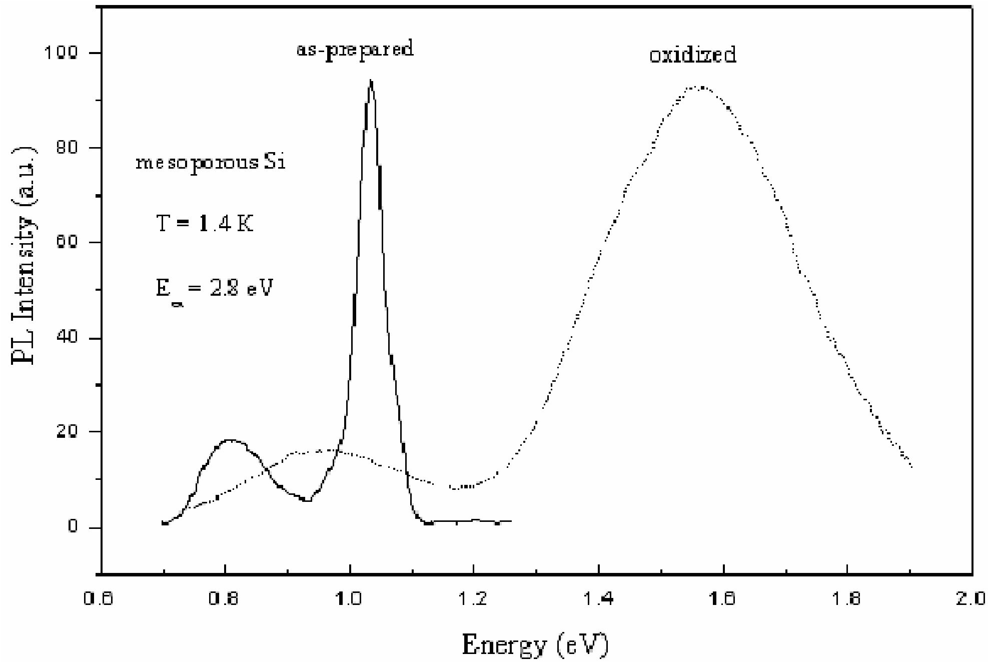

Fig.7.4: Influence of oxidation on the position of the luminescence peak.

1 mA/cm^2 and 300 mA/cm^2; the one exception being a value at 1000 mA/cm^2. In the *Muschik* ref., etching current densities in the interval from 50 to 2000 mA/cm^2 were examined and the corresponding positions of the luminescence peak on the two boundaries were found to be about 1.65 eV and about 2.2 eV respectively. The first value corresponds very well to the considered position for the porous structure in the current work produced with the same etching current density. For the structures obtained with 300 mAcm^{-2} etching current density, our result is about 1.8 eV while the [*Muschik*] ref. presented a slightly higher value of about 1.9 eV. At 1000 mA/cm^2, the discrepancy is more distinct. Our sample shows a luminescence peak of about 1.8 eV compared to about 2.15 eV in the cited work. In the [*Lehmann*] reference, the interval from about 50 to 1000 mA/cm^2 is presented. The reported results are: at 50 mA/cm^2 etching current density, the luminescence peak lies between 1.6 and 1.7 eV ; at 100 mA/cm^2, in the same interval but at a slightly higher energy level than in the previous case; at 300 mA/cm^2, at about 1.9 eV; at 1000 mA/cm^2, at a level marginally above 2.1 eV. Our result at 300 mA/cm^2 etching current density lies at an energy level about 0.1 eV lower and at 1000 mA/cm^2 about 0.25 eV lower than the reported values in both considered references.

In the third cited work, the preparation conditions are different as compared to those in the current work and the considered interval of current densities is too narrow to allow a

reasonable comparison but the blue shift of the luminescence peak can also be indisputably seen. In general, all considered results assert the statement that there is a blue shift of the luminescence peak for an increase of etching current density. The growing value of the H/Si atom number ratio with an enhancement of the etching current density is illustrated in section 4.3.1. Relating this fact to the results obtained in the current chapter, an experimentally established connection between the luminescence peak position and the H/Si atom number ratio can be asserted. The correlation can be expressed as a blue shift of the luminescence peak with a rise of the H/Si atom number ratio values.

The dependence of the luminescence peak position on the substrate resistivity is very clearly expressed. An electrochemical etching on p^+ material with a standard etching solution (see section 2.3.) and etching current of 50 mA/cm^2 in darkness forms a typical mesoporous structure. Because of the very low luminescence efficiency in this material, the luminescence can only be measured at low temperatures (1.4 K in our case). All our efforts to obtain a mesoporous structure on a p^- material with very low etching current densities failed. In these attempts, an interval of about $0.35\ \mathrm{eV}$ (from about $1.08\ \mathrm{eV}$ to about $1.45\ \mathrm{eV}$) within which there are no luminescence peaks present occurs. The same "empty interval" has been observed in the results from the combined thermal effusion and gravimetric measurements for the hydrogen to silicon atom number ratio (see section 4.3.2). This prompts the idea that a smooth transition between the meso- and the micro-porous type of structure is not possible on p^- substrate. For a theoretical explanation of this phenomenon, formation mechanism theories have to be invoked. However, this discussion is not a substantial concern of this work. We can only mention that, for the transition to a mesoporous structure, the low hole concentration in a p^- material cannot be compensated for by changing other structure-determining parameters in the considered boundaries.

It should be noted that not all possibilities for varying the production parameters in our manufacturing procedure were exhausted. For example, we utilized mainly p^- substrates and a standard etching solution (see section 2.3) while p^+ substrate and other etching solution concentrations were utilized only within particular limits. Later experiments [see *Kovalev*] in which the etching solution concentration and doping levels were varied as well as the etching current density show an essential broadening of the potentialities for changing porous structure properties including luminescence. The proper selection of etching solution and etching current density on p^+ substrates enables structures whose luminescent peak lies in the above-mentioned empty interval to be produced and ultimately the whole region from about

$1.08\ \text{eV}$ to about $2.2\ \text{eV}$ to be covered.

The relatively small luminescence peak at about $0.8\ \text{eV}$ (see fig.7.2) is connected with the availability of dangling bonds on the skeleton surface. This is expressed by the appearance of energetic levels at about the middle of the band gap. Radiative electron transitions from the conduction band to these levels or from them to the valence band cause the observed luminescence.

Relating the results from the combined gravimetry and thermal effusion measurements and those in the current chapter, a distinct interconnection of the luminescence peak position with the H/Si atom number ratio values can be established. The determined correlation coincides with the one obtained by means of the etching current density change.

The samples from the "post-etching" series show a fixed immutable position of the luminescence peak for all of them independent of the time for which they lay in the etching solution after switching off of the current source. In our case, this position was at about $1.45\ \text{eV}$. This latter is in accordance with what is observed in the combined thermal effusion and gravimetric measurements and the lack of a tendency in the corresponding hydrogen to silicon atom number ratio values (see section 4.3.3). A possible explanation for this phenomenon is given in section 4.4. In the literature, such a shift is reported for samples prepared on p^+ substrate.

The clearest results come from the series of samples produced under light-assisted anodization. Fig. 7.3 presents the gradual shift of the luminescence to higher energies with the decrease of the minimum wavelength of incident illumination on the sample. Such a tendency in the incident illumination leads to an enhancement of the values for the H/Si atom number ratio, as the results from the combined gravimetry and thermal effusion methods show (see section 4.3.4.). Hence, the already known correlation of the luminescence peak position with the H/Si atom number ratio can be confirmed in that the greater the values of the H/Si atom number ratio, the larger the luminescence peak shift to higher energies is.

All obtained results are in favour of the presence of the above-commented on luminescence peak being interconnected with the H/Si atom number ratio. Small differences exist between the actual values obtained in the current work and those reported in the literature. The observed luminescence peak "blue shift" can be considered as due to band gap widening with the decrease of the skeleton building particle size and it gives strong support to the "quantum size" theory.

In addition, the growing intensity of the luminescence with the "blue shift" is remarkable. In our opinion, with a shift of the particle size distribution peak to smaller values, an

increasing number of particles reach the size at which the "quantum size" effect appears and these contribute to the luminescence.

The change in the position of the luminescence peak of one arbitrarily chosen freshly prepared sample before and after modification by being exposed to air at ambient temperature for a few days is presented in fig. 7.4. In our case, the oxidation, which took place, caused a shift of the luminescence peak to higher energies. The literature provides contradictory information about the direction of the shift. Undisputed is the fact that oxidation influences the luminescence. We want to illustrate and emphasize the importance of measuring the unoxidized sample in order to meet the objectives of this work.

7.4. Conclusions

- The luminescence properties of a variety of samples with different production parameters have been investigated and an interconnection between the luminescence peak position and the values of the H/Si atom number ratio has been established. The larger the values of the H/Si atom number ratio are, the larger the luminescence peak shift to higher energies is.

- The luminescence peaks lie in the interval from about 1.08 eV to about 1.93 eV.

- Samples produced under illumination through low-pass filters show that the luminescence peaks fill the interval from about 1.46 eV to about 1.94 eV. The intensity of the luminescence increases with the shift of the luminescence peak to higher energies.

- The measured samples manifest a strong dependence on the substrate doping, which leads to the appearance of an "empty interval" between about 1.08 eV, obtained for samples on p^+ substrate, and about 1.46 eV, the lower limit obtained for samples on p^- substrate. The presence of this interval is associated with the transition from a nano- to a mesoporous type structure, the principle employment of p^- material as a substrate and the impossibility of the low hole concentration being compensated for by changing the other structure-determining parameters within the considered boundaries. Later reports in the literature reveal that, by widening the preparation conditions, this region can also be filled.

- The oxidation of the sample influences the position of the luminescence peak.

References

1. *Koch* F. Koch, Mat. Res. Soc. Proc. **298**, 319 (1993).

2. *Lehmann* V. Lehmann, B. Jobst, Th. Muschik, A. Kux and V. Petrova-Koch, Jpn. J. Appl. Phys. **32**, 2095 (1993).

3. *Muschik* Thomas Muschik, Dissertation, TU Muenchen (1993).

4. *Mehra* R.M. Mehra, Vivechana Agarval, V.K. Jain, P.C. Mathur, Thin Solid Films **315**, 281-185 (1998).

5. *Kovalev* D. Kovalev, H. Heckler, G. Polisski, and F. Koch, phys. stat. sol. (b) **215**, 871 (1999).

Chapter 8. INTERNAL SURFACE CHARACTERIZATION OF THE POROUS SILICON STRUCTURE

8.1. The Effusion of Hydrogen as Temperature is Ramped for a Characterization of the Internal Porous Silicon Structure Surface

An important step on the way to particle size estimation is to correctly identify the internal surface coverage. The experimentally obtained number of hydrogen atoms N_H can be translated into area for further volume to area ratio determination only if the density of H atoms per unit area is known. In other words, if it is presumed that the internal surface is H terminated, it is important to know the type of the hydride coverage and the relation between the presented mono-, di- and trihydride bonds. Measuring effusion of hydrogen as temperature is ramped provides a suitable method for the clarification of such problems. Additionally, this method enables the precision of the alternative effusion realization – at a constant temperature - to be enhanced.

8.1.1. Typical Effusion Spectra of Freshly-prepared Porous Silicon

On fig. 8.1.1 are shown three spectra of the hydrogen effusion rate versus temperature for samples prepared at different current densities but under otherwise identical production conditions, as described in section 4.3.1. Two strongly expressed peaks are evident at about 400 ^{o}C and 500 ^{o}C and there is a third peak at a lower temperature, which is less distinct by more than one order of magnitude. There even exist samples in whose desorption curves the third peak is not present at all (see tab. 8.1.1). This is probably because the released gas quantity is below the sensitivity threshold of the mass-spectrometer. The position of the third peak is also poorly defined and varies within a wide interval. It has been discovered that this interval is from about 230 ^{o}C to about 360 ^{o}C for the samples investigated by us. The exact positions of the peaks depend on the heating rate but the structure of the desorption rate curve is characteristic for the available bond types. The three-peak desorption curve structure described is typical for the porous silicon samples investigated and it indicates the existence of three different activation energies. It has to be mentioned that the peaks are designated according to the standards accepted in the literature. The first peak is the high temperature peak, the second is the intermediate peak and the third one is the smallest peak at the lowest

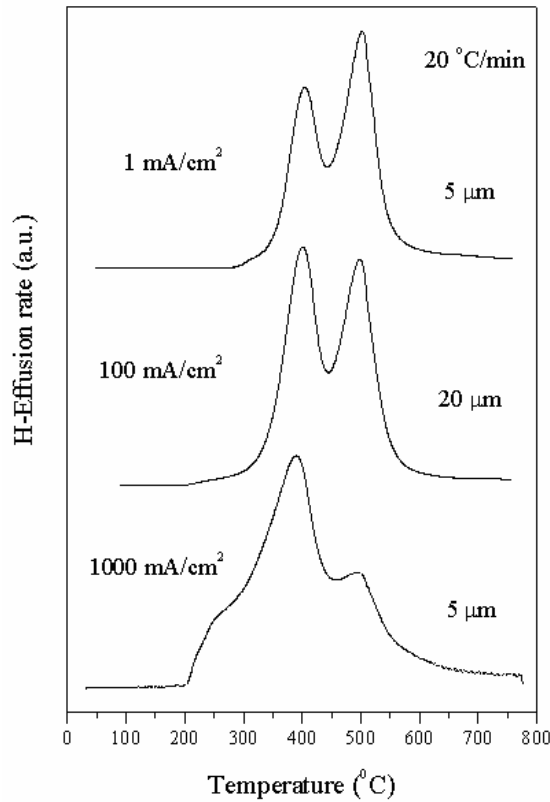

Fig.8.1.1: Comparison of H-effusion spectra from samples produced at different etch-current densities.

temperature.

8.1.2. Experimental Results

A variety of porous silicon structures were extensively investigated to determine the existence or otherwise of some tendency in the surface coverage to change as the production parameters are varied. Many samples, prepared at different etch-current densities lying in the interval $1 \div 300\ \text{mA/cm}^2$, were measured. Over this interval, the mechanical stability of the

No.	Etch-current density [mA/cm2]	Peak 3 (SiH_3)		Peak 2 (SiH_2)		Peak 1 (SiH)		SiH_2/ SiH
		Position (°C)	Relative area (%)	Position (°C)	Relative area (%)	Position (°C)	Relative area (%)	
1	1			407.52	46.64	496.47	53.36	0.4370
2	1	311.3	0.10	405.70	42.40	498.98	57.50	0.3687
3	5			409.76	41.87	498.12	58.12	0.3602
4	5	253.9	0.06	405.24	47.48	496.11	52.46	0.4525
5	10	357.7	1.77	406.16	44.79	498.08	53.44	0.4191
6	30	317.6	0.10	405.52	48.30	499.45	51.50	0.4689
7	50	278.7	0.10	404.42	50.70	496.88	49.20	0.5152
8	100	234.0	0.20	404.00	52.30	494.26	47.50	0.5505
9	100	243.5	0.15	399.11	52.46	497.15	47.39	0.5535
10	300	243.2	0.10	400.75	53.30	495.86	46.60	0.5719

Tab.8.1.1: Relative areas under the H-desorption curve peaks of samples produced at different etching current densities.

structure changes considerably. The observed presence of three peaks in the measured curve makes deconvolution by means of Gauss-functions feasible so that the features of each peak may be characterized separately. Because of the signal record specific properties described in chapter 3.2.2, the area enclosed under each peak is proportional to the number of the hydrogen-silicon bonds with the corresponding activation energies. Consequently, the relative areas under the three peaks can be used as a standard for the relative numbers of the corresponding bonds. Tab. 8.1.1 presents the results obtained by such an analysis. The relative increase of the second peak area compared to that of the first peak with etch-current density enhancement is conspicuous. It is hard to be fouind any tendency in the relative area of the third peak but this can be explained by the extremely small values.

A similar behavior of the ratio of the second peak area relative to that one of the first peak can be established for a series with an alteration of the substrate resistivity. On fig. 8.1.2, it can be seen that the higher the resisitivity, the greater the considered ratio is.

A series of effusion experiments parallel to the infrared transmission measurements for an

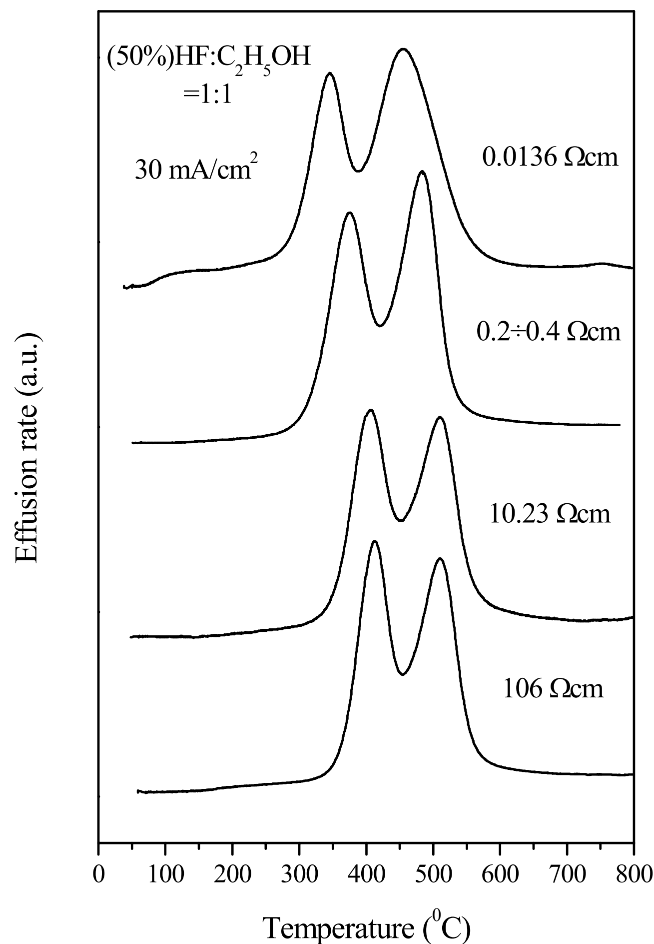

Fig.8.1.2: Comparison of H-effusion spectra from samples produced on substrates of different resistivities.

assignment of the features in the infrared spectrum has been performed and the results are described in chapter 8.2.

The following experiment was performed to answer the question of what the partial pressure of hydrogen is with respect to the total pressure of the gas released during the constant temperature effusion measurement. Normally, it is the effusion rate of one selected component of the gas, the hydrogen molecule in our case that is observed. For this purpose, the mass-spectrometer is fixed on the corresponding mass (or m/e). There is a possibility for the device to run the whole spectrum of masses. If the time for one run is synchronized with the ramp of the temperature in a suitable way, we can obtain the effusion rates of all measurable masses at a quasi-constant temperature. Taking such a spectrum at selected equidistant values of the temperature (e.g. 20 °C), one derives a set by which the complete gas desorption in the whole temperature interval can be traced. On fig. 8.1.3, the spectrum of all measurable masses at 260 °C for a sample produced at 50 mA/cm^2 etching current density and 1 Ωcm substrate resistivity is presented. From each spectrum, we obtain one point for a distinct m/e value (the maximum of the corresponding signal) and, from the set of all such points, we can construct a desorption curve for each of the gas components appearing. In contrast to the continuous spectrum usually obtained, this chart consists of a succession of

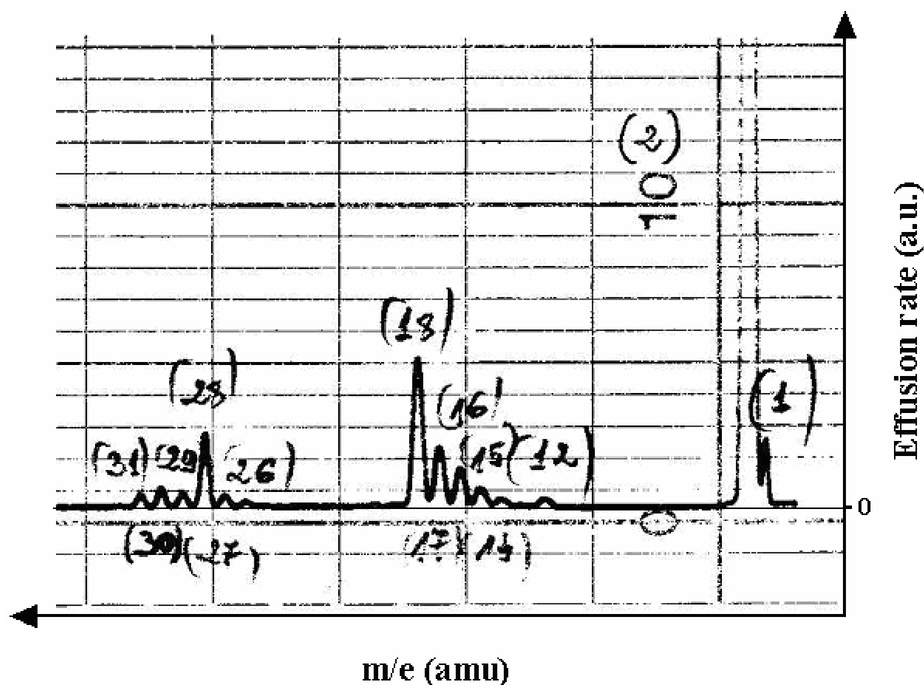

Fig.8.1.3: The spectrum of all measurable masses (the mass of the ion, m, divided by its electrical charge, e) at 260 °C for a sample produced at 50 mA/cm^2 etching current density and 1 Ωcm substrate resistivity.

points equidistant on the temperature scale. By interpolating in an appropriate manner (e.g. linking neighbouring points with a straight line) one can produce a continuous effusion curve. This is illustrated for mass 1 on fig. 8.1.4. The integral of this curve expresses the entire quantity (partial pressure) of the corresponding gas component, which is measured by the mass-spectrometer. By comparing the results for all attending masses, one can determine the relative fraction of every distinct component from the total detected gas quantity (total gas pressure). The results obtained from our experiment are presented in tab. 8.1.2. The different gas components in the table are denoted with numbers and are not identified. The exact identification of every component was not an aim of this work, although for most of the components it is possible to distinguish the molecules (e.g. mass 2 is H_2). Having in mind the content of the samples as determined from other experiments (e.g. ERDA – see chapter 5.1.4), it is possible to speculate about the identity of the components. 17 different masses appear in the considered interval from $40\ ^{o}C$ to $900\ ^{o}C$. They can be arranged into three groups.

The first group consists of masses $1 \div 3$. At least the first two members of the group are associated with the hydrogen molecule – correspondingly double and, probably, with single charged hydrogen atoms. The strongest signal belongs to mass 2, which is a single charged H_2. The second group comprises the masses $12 \div 20$, which are connected with different ions originating from the etching solution (e.g. mass $18 - H_2O^+$, mass $20 - HF^+$).

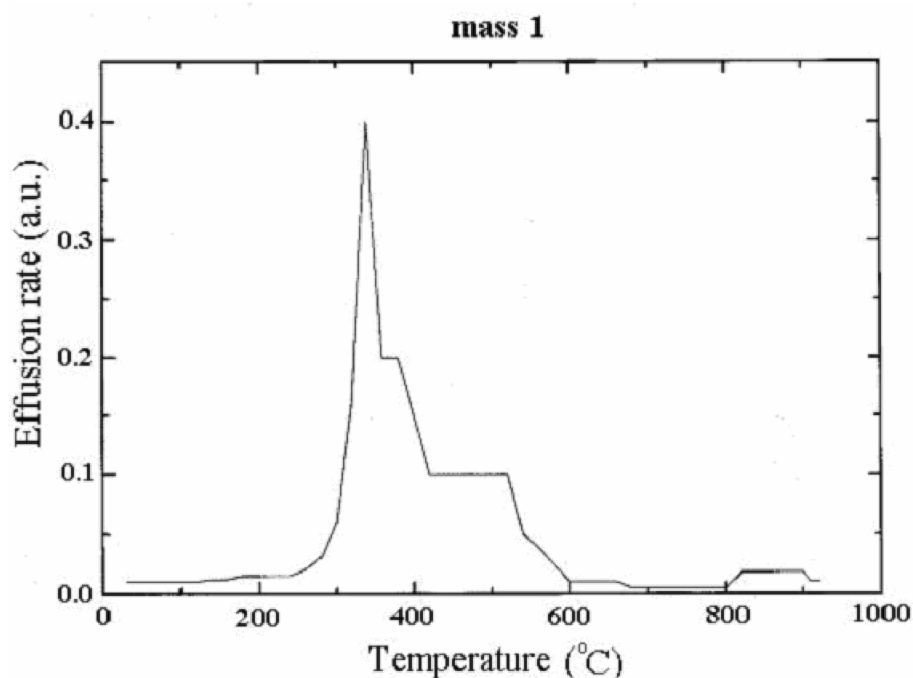

Fig.8.1.4: Constructed effusion spectrum for mass 1.

Mass No.	Area [a.u.]	Participation in the total pressure [%]
1	44.65	0.40
2	10153.86	96.33
3	79.20	0.75
12	1.40	0.01
14	4.92	0.05
15	12.59	0.12
16	13.91	0.13
17	14.01	0.13
18	42.59	0.40
19	0.78	0.01
20	0.17	0.00
26	5.77	0.05
27	28.17	0.27
28	63.70	0.60
29	23.12	0.20
30	33.49	0.30
31	18.18	0.17

Tab.8.1.2: Relative fractions of the gas components in the total gas pressure.

The third group comprises masses $26 \div 31$. In our opinion, this group is also due to etching solution derivatives (e.g. mass $29 - C_2H_5^+$).

From the data presented in table 8.1.2, it is seen that the H_2 partial pressure comprises more than $96\ \%$ of the total pressure of the gas released as a result of the desorption process.

It has to be mentioned that the measurement was performed in an open system with a permanently operating ion-getter pump. Because of this, the detected quantity of a distinct gas component is not identical to the gas quantity released from the sample but is proportional to it.

For a correct comparison of the gas quantities (partial pressures), two further important factors, the exhaustion rates of the ion-getter pump and the sensitivity of the mass spectrometer to the different gases (see sec. 3.2.), have to be considered. The exhaustion rate of hydrogen is the highest in relation to the other expected effusion gases (see tab. 3.2.1, chapter 3.2.), which means that a relatively small part of the entire quantity of H_2 released during the effusion process is detected. The entire sensitivity of the mass spectrometer for hydrogen is the smallest in relation to the other expected desorption gasses (see tab. 3.2.3, sec. 3.2.).

Bearing in mind these arguments, the reported number of $96\ \%$ for the H_2 participation in the total gas quantity has to be considered as the lower limit for this value.

8.1.3. Comments

For the purposes of the current work, it is important the following questions be answered:

- The presence of both main peaks must be explained and their assignment verified;
- The orientation and ordering of the internal surface must be derived;
- The order of the desorption kinetics must be estimated.

For an analysis of the desorption curves, we invoke the results obtained in section 8.2 and employ infrared spectroscopy in parallel. One of the main results from this is the determination that a homogeneous orientation (and, connected with this, the presence of some specific bond type or types) of the internal porous silicon surface after sample preparation is not to be expected. Consequently, it is improbable that the high-temperature peak is connected only with a distinct reconstruction during the effusion process of this presumably homogeneously oriented internal surface. Assuming that all crystal orientations are present on the internal surface after porous structure preparation, the only plausible possibility left is that the two peaks originate from a breaking of $Si-H$ and $Si-H_2$ bonds, respectively. Some local reconstruction during the effusion process must not be excluded, but it cannot be decisive for the form of the desorption curve.

Such an assertion, based on the infrared spectroscopy results, is in accordance with data in the literature on thermal effusion of hydrogen from Si surfaces [ref. *Gupta*, *Koehler*, *Zoubir*], where the low-temperature peak is identified as connected with dihydride (SiH_2) and the high-temperature peak as connected with monohydride (SiH). This conclusion is substantiated by theoretical calculations of the silicon-hydrogen bond energies (larger for the monohydride) for SiH and SiH_2 surface spaces [see e.g. *Ciraci1*] as well as by thermal desorption experimental results for a variety of degrees of surface coverage on Si(111) 7x7 [see *Koehler*] or on Si(001) (2x1) [see *Wise*, *Raschke1*, *Gokhale*]. At a low grade of surface coverage, only the high-temperature peak originating from the monohydride is present.

We have tried to obtain additional information from the experimental desorption curves using an integral method for the extraction of the kinetic desorption parameters described in sec. 3.1.4. and developed by Chan et all. [see *Chan*]. This approach has been applied on a series of experimental curves for porous structures produced at different etch-current densities. Only the first two peaks have been considered because they are much more distinct than the third peak. The results are presented in tab. 8.1.3.

Etch-current density [mA/cm^2]	II peak				I peak			
	Half-width [^{o}C]	Desorption kinetics order	Activation energy- E_d^1 [eV]	Pre-exponential factor- ν_{01} [s^{-1}]	Half-width [^{o}C]	Desorption kinetics order	Activation energy- E_d^2 [eV]	Preexponential factor- ν_{02} [s^{-1}]
1	≈ 66	I	0.53	4.42x10^5	≈ 68	I	0.84	3.67x10^6
5	≈ 66	I	0.54	6.39x10^5	≈ 62	I	0.94	4.78x10^7
10	≈ 62	I	0.58	2.13x10^6	≈ 66	I	0.89	1.23x10^7
50	≈ 58	I	0.60	2.95x10^6	≈ 75	I	0.81	2.11x10^6
100	≈ 66	I	0.54	6.41x10^5	≈ 70	I	0.85	4.96x10^6
300	≈ 74	I	0.48	9.09x10^4	≈ 80	I	0.80	1.62x10^6

Tab.8.1.3: Results from applying the Chan et al. method [see *Chan*] to a series of porous samples produced at different etch-current densities.

For a comparison with the data in the literature, we have used several sources: thermal effusion measurements of amorphous silicon films, flat and vicinal monocrystalline silicon surfaces and porous silicon. In the hydrogen effusion of amorphous silicon films, the two-peak structure of the desorption curve is also observed but in a comparison with our samples it is conspicuous that the half-width of the low-temperature peak is about double that usually reported. The enhanced half-width of the high-temperature peak is still more distinct [see *Beyer*]. In the work of Fuchs et al. [see *Fuchs*], a comparative picture of the desorption curves from amorphous silicon and porous silicon sample, without information about its production parameters, treatment or type of structure, is shown. In this picture, the half-width of the high-temperature peaks for the two considered structures are approximately equal. We have obtained a similar form of the curve only with mesoporous samples [see *Hofmann*, *Meyer*]. For thick, (about $100\,\mu m$ and thicker) freestanding mesoporous samples, (fig. 8.1.5), we have observed the appearance of a “shoulder” positioned near the main high-temperature peak between 550 and $600\ ^oC$. This discrepancy has not been extensively investigated because such thick samples were rarely used for our measurements. Another reason for not studying this feature is that the shoulder doesn’t appear with thin mesoporous samples on a substrate and the mesoporous structure itself is not particularly important for the quantum size effect theory. Because of the lack of information, however, it is difficult for us to speculate on the causes of such a distortion of the curve. This does not stop us suggesting two further possibilities additional to proposals in the literature [see *Fuchs*] that some of the hydrogen has diffused into the Si skeleton or is bound in a way similar to α-Si:H. The thickness of the sample for the hydrogen atoms released deep in the sample’s volume has, in relation to the

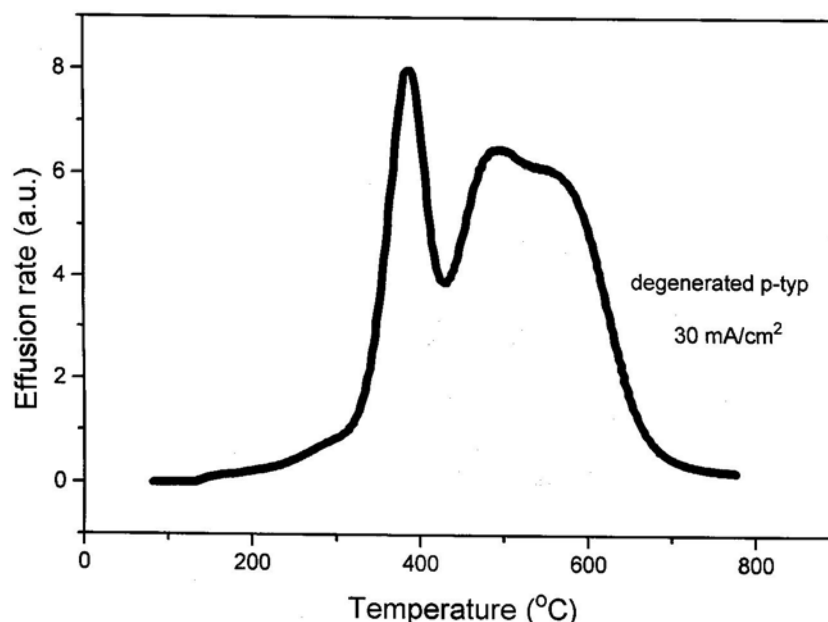

Fig.8.1.5: Effusion spectrum of thick (about 100 μm) freestanding mesoporous structure.

detected signal, an influence similar to that of the diffusion of these atoms in the α-Si:H structure. This means that, independently of the existing pores, the released hydrogen atom needs a certain time to reach the surface of the sample. Detection by the mass-spectrometer is delayed with respect to the moment of the bond breaking. It is effectively observed as a signal shift towards the higher temperature because of the temperature ramping. It is also possible that the electro-polishing procedure plays some role.

It can be generalized that the significant difference in the half-widths between the nanoporous and amorphous thermal effusion spectral peaks shows that the internal surface of the skeleton cannot be disordered to the same degree that one would expect in amorphous silicon.

Other authors [see *Zoubir*] have published porous silicon effusion curves which are very similar to ours concerning the peak positions and their half-widths.

The characteristics of our desorption curves vis-à-vis the positions of the two peaks and their half-widths are comparable with those which we found in the literature for flat and vicinal well-oriented monocrystalline silicon surfaces. Raschke and Höfer [see *Raschke1, Raschke2*] investigated the surface kinetics of hydrogen adsorbed on vicinal Si(001) surfaces inclined towards the $[110]$ direction by different angles and, respectively, step densities. These studies showed traces (heating rate ≈ 3 K/s) of a step-saturated, fully monohydride and partially dihydride covered Si(001) $5.5^0 \rightarrow [110]$ misoriented surface. This curve contains two peaks, corresponding to H_2 originating from mono- and dihydrides. As can be expected, the

first peak is much higher than the second peak. The positions of the two peaks are at about 700 K and about 800 K for the low- and high-temperature peaks respectively and the half-widths of the peaks are approximately $50 \div 70\ ^{o}C$. It is remarkable that, although the hydrogen binding energy at the steps is higher than on the terraces, we see only one monohydride peak. Gokhale et al. [see *Gokhale*] presented hydrogen desorption curves from Si(001)-(2x1) for various exposures to atomic H at $640\ K$ and a heating rate of $5\ K/s$. It is not indicated whether the saturation coverage is shown. All traces display one peak at about $800\ K$ - the position of the monohydride originated H_2. Schulze et al. [see *Schulze*] presented typical desorption curves from saturation coverage of a cleaved Si (111) surface at a heating rate of $6.6\ K/s$. The average angle of inclination is less than 1^0, which means low step densities. The curve exhibits two more distinctive and one less distinctive peak. The positions of the two main peaks are shifted to higher temperatures in comparison with our curves, which is caused by the higher heating rate. The half-widths of the two peaks are nearly the same as those of our curves. The height of and the area under the high-temperature peak are about three times larger than those of the low-temperature one. Koehler et al. [see *Koehler*] showed a spectrum for a hydrogen desorption from $Si(111)\ 7x7$ for a different initial surface coverage (heating rate $8.8\ K/s$). Only the high temperature peak of the monohydride is observed at coverage, which is smaller than half of the saturation coverage. This peak continues to grow and the low-temperature peak appears at higher coverage. At saturation coverage, the ratio between the two peak areas is consistent with the results in the work of Schulze and Henzler [see *Schulze*]. Wise et al. [see *Wise*] presented a comparison of hydrogen desorption kinetics from $Si(111)\ 7x7$ and $Si(100)\ 2x1$ surfaces. The study focused on H_2 desorption from the high-temperature peak associated with monohydride species. The angle of inclination with respect to the Si(111) plane was $\alpha = 0 \pm 0.25^0$ and for Si(100) is not indicated. In contradiction to previous publications [see *Koehler* and *Schulze*], the presented spectra for the two surfaces exhibit only one peak, caused by the preliminary annealing to $656\ K$ for 30 sec. The authors concluded that the comparable desorption activation energies indicate similar $Si - H$ bond strengths on both surfaces.

The only publication which we know of concerning the thermal effusion of porous silicon in detail, is that of Gupta et al. [see *Gupta*]. The authors derived their conclusions regarding $Si(100)$ orientation of the internal surface mainly from infrared measurements. They traced the integrated absorbance of specific modes as a function of time at different temperatures. In our opinion, such an approach does not give unambiguous results because it is not completely

clear whether the considered modes are mixed (see section 8.2). Gupta et al. [see *Gupta*] predicted the hydrogen temperature programmed desorption (TPD) signal. They also recognized that this spectrum is "nearly identical to the measured TPD spectrum of hydrogen on $Si(111)7x7$ obtained at saturation coverage..." and also "... nearly equivalent to the TPD spectrum of hydrogen on $Si(100)2x1$ obtained at saturation coverage...". In this we see an acknowledgment that there is no direct evidence from thermal effusion experiments that the internal surface has any preferential orientation.

We think that all commented upon results, supplemented with the almost equal height of the two main peaks (see tab. 8.1.1), show that many orientations probably appear on the surface, which confirms the results from the transmission infrared measurements. It is also possible that there aren't any developed orientations at all (see section 8.2.). These statements are not provable precisely by means of thermal effusion and infrared spectroscopy but, in any case, neither method provides information that these assertions are wrong.

Recent publications [see *Raschke3*] claim that, "despite over 40 years intensive investigations, one of the most fundamental quantities characterizing that absorption system, the $Si-H$ bond energy E_{Si-H} ,, even on well defined single crystal surfaces, is not well known". Neither estimates based on the bond energies in silanes nor of *ab initio* calculations are helpful. The results vary widely depending on the theoretical approach $(E_{Si-H} = 2.9 - 3.7\ eV)$. An attempt to clarify the problem [see *Raschke3*] by comparing the different values for $Si(111)7x7$ and $Si(001)2x1$ with hydrogen bonding in silanes and Si clusters has indicated that the local structural environment of the bonding Si atoms sensitively influences the $Si-H$ bond strength.

Nevertheless, the activation energies obtained for the investigated series and presented in tab. 8.1.3. differ so much from the theoretical predictions that it places doubt on the reliability of the results. The method used is an integral approach and is useful only when the desorption parameters are not coverage dependent (see section 3.1.). This condition is clearly not fulfilled in our case.

Additionally, the suppositions about the internal surface orientation in porous silicon makes groundless any attempt to determine the binding energies for the monohydrides or for the dihydrides. In contrast to the case for well-defined surfaces, it is not clear what the value obtained for porous silicon might indicate other than some kind of indefinable averaging.

Having in mind the presented considerations, the determination of the kinetic parameters in porous silicon is a nonproductive task.

Gupta et al. [see *Gupta*] reported a second-order desorption kinetics for the silicon dihydride species as a new observation in contradiction with some older studies. Such a possibility is confirmed by a theoretical work on the Si(001)-(1x1) and Si(001)-(2x1) surfaces [see *Ciraci2*]. It is asserted that the desorbing H_2 molecule was formed by a recombinatory desorption of two hydrogen atoms from two adjacent silicon dihydride species, which means a second order desorption. For the monohydride species also, second-order kinetics is anticipated where two adjacent silicon monohydride species must recombine in order to form H_2.

Answering questions about the desorption order would help to determine whether, for example, the high-temperature peak results only from initial monohydrides or there is a component which is due to the transformation of the initial dihydrides during the effusion process leading to an appearance of secondary monohydride bonds. In other words, whether, by the integration of both the low-temperature and the high-temperature peaks and the construction of their ratio, the initial relative population distribution can be obtained.

Two different mechanisms have been proposed for the hydrogen desorption from dihydride species on the $Si(100)$ surface [see *Flowers*]. The **first** is a recombinative desorption of two hydrogen atoms from adjacent silicon dihydride species, which presents the conversion of two dihydride species to a doubly occupied dimer and requires second order kinetics. With further enhancement of the temperature, the remaining hydrogen atoms would be released as monohydrides. They would present an additional component to the initial monohydrides for the high-temperature peak. The **second** is the self-associated desorption of two hydrogen atoms on a single silicon atom and predicts first-order kinetics for the dihydride desorption. In our opinion, if we accept the first kinetic mechanism for the desorption traces; it would mean that the first peak always has to be larger than the second. But, we have enough desorption spectra (see figs. 8.1.1 and 8.1.2) where the first peak is essentially smaller than the second one. This argument justifies the assumption that, in porous silicon, the second mechanism is probably valid.

It is noticeable that our results (see tab. 8.1.3) for all samples and for each one of the two different bonds produced first order desorption kinetics.

It has to be mentioned that there are extreme contradictions in the literature. Shane et al. [see *Shane*] considered that “long range surface structure (where “long range” refers to distances on the order of the silicon lattice spacing) did not play an important role in the (recombinative desorption) dynamics”. Raschke and Höfer [see *Raschke2*] remarked that “the rearrangement of substrate atoms from their ideal lattice positions plays a crucial role in the ...

reaction mechanism”.

8.1.4. Conclusions

In our opinion, the whole above-presented information leads to the following conclusions:

- The low-temperature main peak of the desorption curve originates from dihydrides and the high-temperature main peak originates from monohydrides. For a series produced with different etching current densities, the ratio of the area under the second peak to the area under the first increases with the enhancement of the current density. For a series produced with different substrate resistivities, the ratio of the area under the second peak to the area under the first increases with the enhancement of the substrate resistivity. In both cases the larger the values of the H/Si atom number ratio are (and therefore the larger the luminescence peak shift to higher energies), the larger the SiH_2/SiH number is.

- The thermal effusion results didn't allow us to claim that the internal Si surface is only (100) or (111) oriented.

- The half-width values of the two main peaks and their roughly equal heights reveal that the surface is a combination of differently oriented plains rather than amorphous.

- It is not possible to distinguish whether the monohydride peak originates from $\mathrm{Si}(100)\,2\mathrm{x}1$ or from $\mathrm{Si}(111)\,7\mathrm{x}7$.

- It is not possible to make any deduction about whether there is a reconstruction at all and, if so, what its type is.

- Because of the surface complexity, it is not reasonable for activation energy determination to be promoted to a goal of this investigation.

- The dihydride desorption mechanism in porous silicon structures cannot be entirely second order.

- With the constant temperature effusion measurement, the partial pressure of H_2 comprises more than $96\,\%$ of the total gas pressure released as a result of the desorption process.

References

1. *Gupta* P. Gupta, V.L. Colvin, and S.M. George, Phys. Rev. B **37**, 8234 (1987).
2. *Koehler* B.G. Koehler, C.H. Mak, D.A. Arthur, P.A. Coon, and S.M. George, J. Chem. Phys. **89** (3), 1709 (1988).
3. *Zoubir* N. Hadj Zoubir, M, Vergnat, T. Delatour, and Ph. De Donato, Appl. Phys. Lett. **65** (1), 82 (1994).

4. *Ciraci1* S. Ciraci, R. Butz, E.M. Oelling and H. Wagner, Phys. Rev. B **30**, 711 (1984).
5. *Wise* M.L. Wise, B.G. Koehler, P. Gupta, P.A. Coon and S.M. George, Surf. Sci. **258**, 166 (1991).
6. *Raschke1* M.B. Raschke and U. Höfer, Phys. Rev. B **59** (4), 2783 (1998).
7. *Gokhale* Shubha Gokhale, Andreas Fink, Peter Trischberger, Karl Eberle, and Wolf Widra, J. Vac. Sci. Technol. A **19** (2), 1 (2001).
8. *Chan* C.-M. Chan, R. Aris and W.H. Weinberg, Appl. Surf. Sci. **1**, 360 (1978).
9. *Beyer* W. Beyer, in "Tetrahedally-Bonded Amorphous Semiconductors", D. Adler and H. Fritzsche, eds. Plenum Press, New York (1985), p.129.
10. *Fuchs* H.D. Fuchs, M. Stutzmann, M.S. Brandt, M. Rosenbauer, J. Weber, A.Breitschwerdt, P. Deak, and M. Cardona, Phys. Rev. B **48** (11), 8172 (1993).
11. *Hofmann* D.M. Hofmann, B.K. Meyer, P. Christmann, T. Wimbauer, W. Stadler, A. Nikolov, A. Scharmann, and A. Hofstätter, Materials Science Forum **196-201**, 1673 (1995).
12. *Meyer* B.K. Meyer, D.M. Hofmann, P. Christmann, W. Stadler, A. Nikolov, A. Scharmann, and A. Hofstaetter, Mat. Res. Soc. Symp. Proc. **358**, 453 (1995).
13. *Raschke2* M.B. Raschke, U. Höfer, Appl. Phys. B **68**, 649 (1999).
14. *Schulze* G. Schulze and M. Henzler, Surf. Sci. **124**, 336 (1983).
15. *Raschke3* M. B. Raschke, U. Höfer, Phys. Rev. B **63,** 201303-1(R) (2001).
16. *Ciraci2* S. Ciraci and Inder P. Batra, Surf. Sci. **178**, 178 (1986).
17. *Flowers* Michael C. Flowers, Nevile B.H. Jonathan, Young Liu, and Alan Morris, J. Chem. Phys. **99** (9), 7038 (1993).
18. *Shane* Stacey Shane, Kurt W. Kolasinski, and Richard N. Zare, J. Chem. Phys. **97** (5), 3704 (1992).

8.2. Transmission infrared measurements for a characterization of the internal porous silicon surface structure

Infrared (IR) vibrational spectroscopy is based on the ability of a certain group of atoms (a molecule) to absorb incident illumination at specific wavenumbers. The absorbed radiation is converted into energy in the form of molecular vibrations. This resonance absorption gives rise to the appearance of characteristic peaks (bands) in the corresponding absorption spectrum. The wavenumbers are characteristic for the available chemical bonds.

A system of N atoms assumed to be a molecule has a total of $Z = 3N$ degrees of freedom corresponding to the space coordinates of each atom in the molecule. In a structurally nonlinear molecule, 3 of these degrees are rotational, 3 are translational and the remaining $Z = 3N - 6$ are the fundamental vibrations. In a linear molecule, 2 degrees are rotational, 3 are translational and therefore the number of fundamental vibrations is $Z = 3N - 5$. This quantity actually represents the maximum number of possible bands within the spectrum. It is important to note that in order to be IR active, a vibration must cause a change in the dipole moment of the molecule and the larger this change is, the stronger is the intensity of the corresponding band. In fact, the number of observed bands differs from Z. In case that (a) some of the vibrations are degenerate (have coincident vibrational frequencies) or (b) because of their dipole constancy, the bonds are IR-inactive or (c) when at lower resolution, depending on the apparatus, a band cannot be recognized, the number of observed bands is smaller than Z. When combinations of vibrations (a combination of two or more vibrations) or overtone bands (connected with transitions from the ground to states higher than the first excited states) appear, the number of observed bands can be greater than Z.

There are two types of molecular vibrations: stretching and deformation. The first type corresponds to atomic motions, which lead to a change of the bond lengths; the second type arises with vibrations that cause changes of the bond angles.

A harmonic oscillator represents the stretching vibration in a diatomic molecule. The following formula has been derived from the Hooke's low:

$$k = \frac{1}{2\pi c}\sqrt{\frac{f(m_1 + m_2)}{m_1 m_2}} \tag{8.2.1}$$

where k is the wave number (cm^{-1}),

m_1 and m_2 are the masses of atoms 1 and 2, respectively (g),

c is the velocity of the light (cm/s), and

f is the force constant of the bond (dyne/cm).

Chemisorption of an N-atom species on a solid may involve a major rearrangement of the bonding pattern and hence a significant change in some or all of the vibrational frequencies.

An infrared spectrum may be presented in two ways – in transmission or in absorption. In the first case, the percent transmittance $T\,\% = \frac{I}{I_0} x100$ is plotted on the Y-axis, where I and I_0 are the intensities of the transmitted and the incident illumination respectively. In the second case, absorbance is used:

$$A = \log_{10}(I_0/I) = \log_{10}(1/T) = \varepsilon c l \qquad (8.2.2)$$

where ε is the decimal absorption,

c is the concentration of the absorbing species, and

l is the thickness of the sample.

In this presentation, the direct proportionality between the absorbance of an absorbing species and concentration offers important advantages.

Involving transmission infrared spectroscopy allows the clarification of two very important questions, which are connected with the current work to be pursued.

As is known from the literature, the internal surface of the porous silicon is covered by hydrogen. In view of the aim of this work, it is of primary importance to determine the type and distribution of the presented Si-H bonds. In parallel with effusion measurements as the temperature is ramped, the experimental method described addresses our **first** goal of gaining information about the surface coverage of the porous silicon skeleton. Preparations of deuterium-terminated porous silicon have also been utilized and proven useful in determining the vibrational assignments.

A **second** aim of our work is to be able to observe the process of changes within our samples. After their fabrication but before introduction into the effusion installation, the freshly prepared structures were exposed to the ambient atmosphere for about 30 min. Approximately this time is required for the completion of other measurements such as luminescence and infrared spectroscopy which help to characterize the sample. It naturally comes into question whether the sample preserves its original characteristics during this time.

It has to be mentioned that, because of their huge intrinsic area and the correspondingly large number of bonds, the porous silicon structures are especially suitable for the application of infrared spectroscopy.

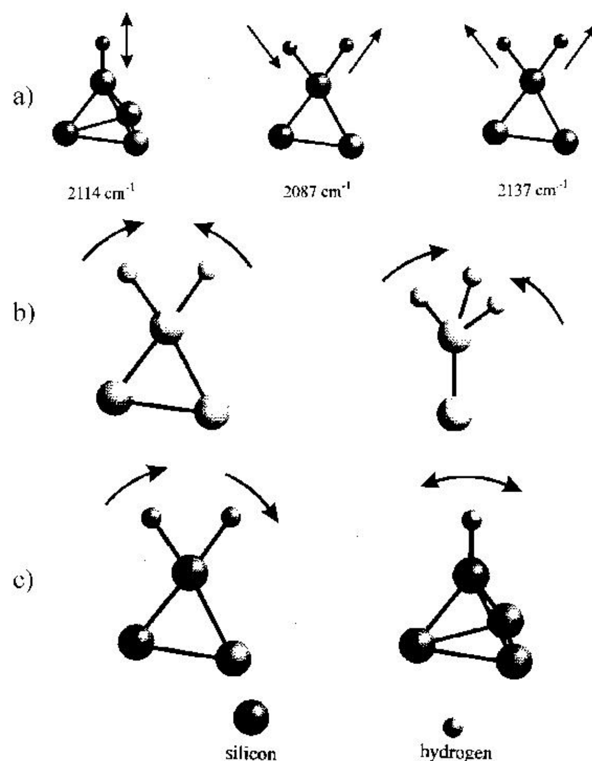

Fig. 8.2.1: Sketches of Si-H: a) stretching modes; b) scissor modes; c) wagging modes;[after *Theiß*].

In view of the above-mentioned aims of the study, the most important bonds to be investigated are the Si-H, Si-O and O-Si-H. In the following figures, the possible vibrational modes for the Si-H bond (fig. 8.2.1) and the different ways in which oxygen may be present in the silicon back bonds (fig. 8.2.2) are presented. For some of the modes, the oxygen atom positions in porous silicon as reported in the cited publication are given. In principal, these positions are expected to be different in comparison with those for the same atom groups lying on a smooth monocrystalline silicon surface because of the influence of the local environment.

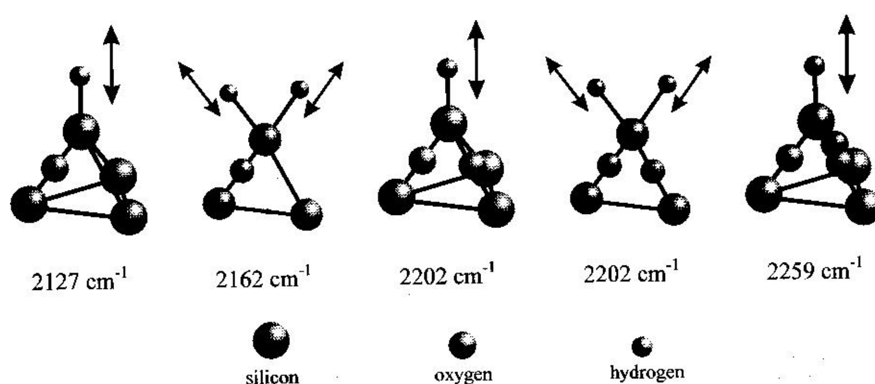

Fig. 8.2.2: Si-H stretching modes modified by the presence of oxygen atoms in the silicon backbonds [after *Theiß*].

8.2.1. Experimental conditions

The porous silicon was prepared in darkness or under various illumination conditions on back-implanted p-substrate ($1-5\ \Omega\text{cm}$ resistivity) with $HF:H_2O:C_2H_5OH=1:1:2$ etching solution. The etching current density was selected to be $1\ \text{mA/cm}^2$ because of the relatively high mechanical stability of the corresponding porous structure. This mechanical stability is required in view of the chemical treatment the samples undergo following thermal effusion.

For deuterium-terminated porous silicon as components of the etching solution, we used DF, D_2O (99.8 %, Merck Sharp & Dohme), and ethanol-d_6 (Cambridge Isotope Laboratories). DF was produced by the reaction of deuterated sulphuric acid with calcium fluoride which was trapped using dry ice. This method was applied by the group of Prof. Schmidtbauer from the chemical department of TUM.

A Perkin-Elmer 1760X Fourier-transform spectrometer with a resolution of $4\ \text{cm}^{-1}$ was used for the investigation. The sample was fastened to an Al holder and illuminated through a 3 mm diameter hole. After inserting the sample into the measuring chamber, the latter is hermetically sealed and filled with an inert gas. For samples lying on a substrate, a piece of

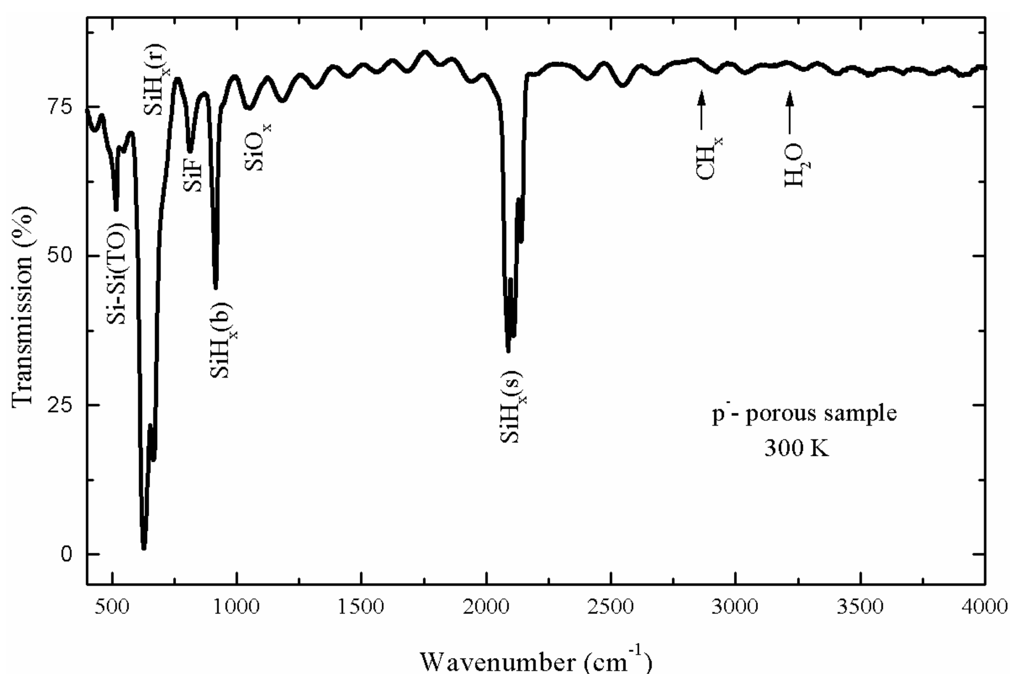

Fig. 8.2.3: Typical spectrum of a freshly prepared microporous sample.

the same wafer is used to obtain a referent measurement. This allows the avoidance of substrate and environmental influences on the investigated spectra. The division of the measured spectra on the referent leads to the desired result. For freestanding samples, the referent measurement was performed through the inert gas alone. The measuring interval was from $400\ cm^{-1}$ to $4000\ cm^{-1}$.

8.2.2. Typical infrared transmission spectrum for freshly prepared porous silicon

Fig. 8.2.3 shows a typical spectrum for a freshly prepared microporous sample when properly treated after preparation (see section 2.3). The available vibrational bands are indicated according to data in the literature. Most of the attendant vibrational modes will be further commented upon closely in conformity with the aims of the current work.

8.2.3. Experimental results

In fig. 8.2.4, samples with different degrees of deuteration on the internal surface are compared and a tendency for an alteration of the characteristic vibrational bands is observed.

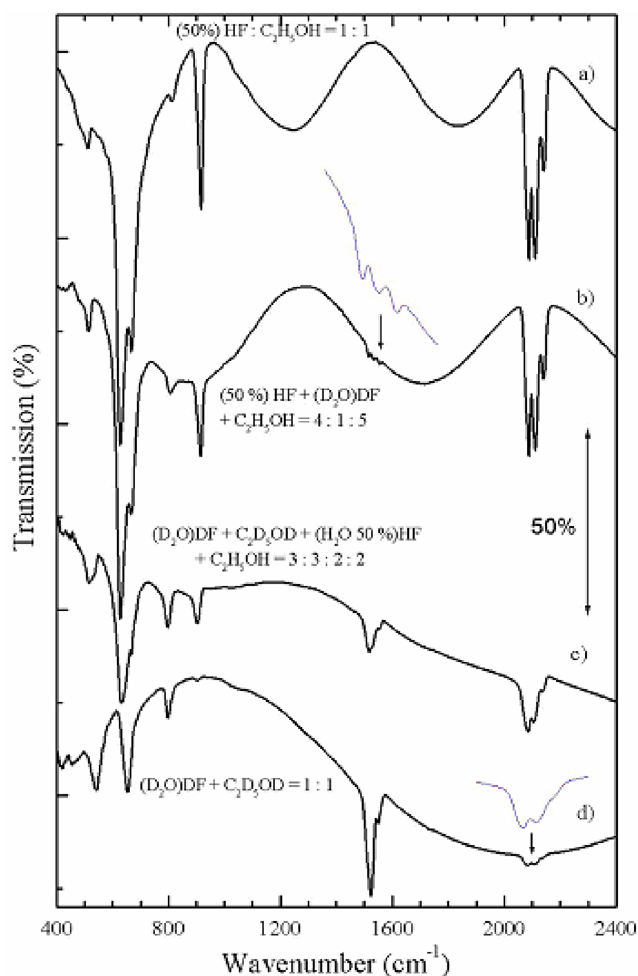

Fig. 8.2.4: Comparison between samples with a different degree of internal surface deuteration.

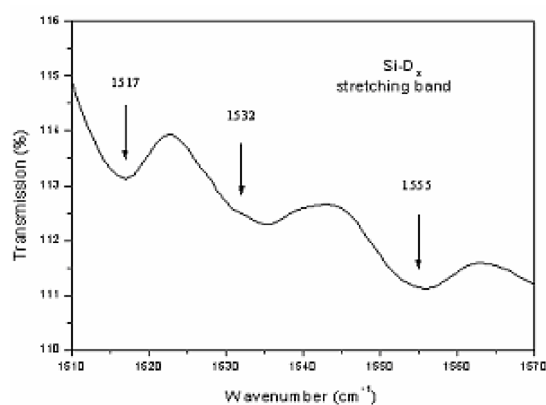

Fig.8.2.4-e): Si-D$_x$ stretching band of the curve in Fig. 8.2.4-b).

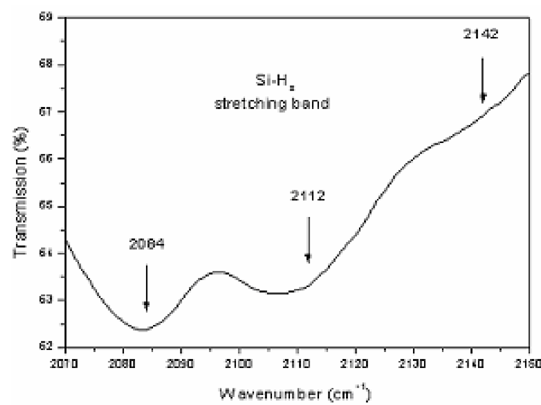

Fig.8.2.4-f): Si-H$_x$ stretching band of the curve in Fig. 8.2.4-d).

Fig. 8.2.4-a) presents the normal porous silicon sample with a fully hydrogen-terminated internal surface, determined by using a standard etching solution. Figures 8.2.4-b) and 8.2.4-c) depict partially deuterated spectra and fig. 8.2.4-d) shows a spectrum of almost fully deuterated porous silicon. For the production of such samples, an etching solution comprising a mixture of HF, DF, H_2O, D_2O, C_2H_5OH and C_2D_5OD was used with concentrations indicated on the corresponding pictures. On fig. 8.2.4-e) and fig. 8.2.4-f) are depicted the Si-D$_x$ and Si-H$_x$ stretching regions of the curves from fig. 8.2.4-b) and fig. 8.2.4-d), respectively.

The next figure (see fig. 8.2.5) presents infrared results from samples handled by the specific technique of combining the thermal effusion with a following dip in DF/D_2O solution. This method was utilized as a source of additional information about the species present and their assignments.

A series of effusion experiments were performed on identically prepared samples at $20\ ^{o}C/min$ ramp of the temperature in a high vacuum chamber. The increase of the temperature for each sample was halted at a different value in the interval from $325\ ^{o}C$ to $550\ ^{o}C$ with a $25\ ^{o}C$ step. The sample was then held at its final temperature for about $5\ min$. (The duration of $5\ min$ was empirically chosen such that at the end of this period the effusion signal decreases by two orders of magnitude.) After the porous silicon has been cooled, the sample is refreshed in a DF/D_2O solution to 'freeze in' the status of the hydrogen termination and to remove the oxidation so that an infrared spectrum can finally be obtained. In fig. 8.2.5, the resultant spectra at selected temperatures are depicted.

The reproducibility of the initial spectrum after such a treatment is confirmed by a comparison of two infrared spectra. The first one was obtained from a porous silicon sample immediately after preparation. The second one was measured after effusion at $400\ ^{o}C$ and following refreshment with the etching solution. This result is not presented here.

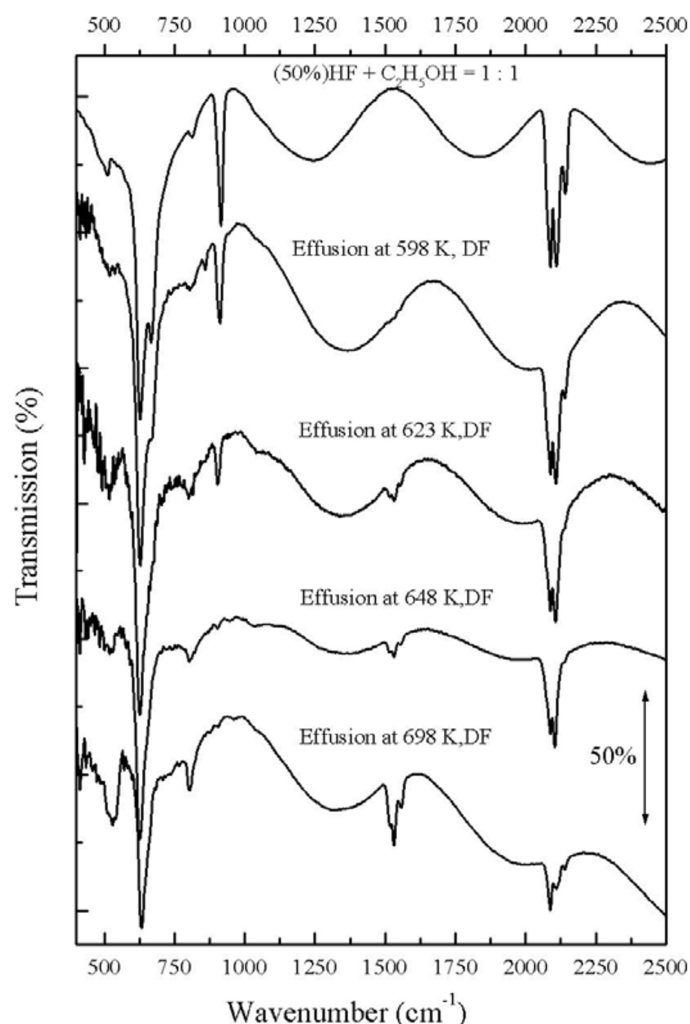

Fig. 8.2.5: Comparison between samples, handled by a combination of the thermal effusion with a following dip in DF/D_2O solution.

Infrared spectra for samples produced under illumination through different filters (RG-550 and WG-450) (see section 2.3.) are shown in fig. 8.2.6. The aim of these measurements was to obtain information on how the coverage of the internal surface changes with increases in the surface to volume ratio of the particles building the porous structure skeleton (see chapter 9). Additionally, these measurements allow the absence of samples' oxidation to be substantiated and, on the basis of this, further vibrational modes can be assigned.

The infrared spectroscopy is also used as a control for the appropriateness of the chosen handling procedure with a view to a preservation of the original properties of the porous structure. As has already been mentioned, the duration of the period from the production of the sample to its placement into the effusion installation is about 30-40 min. In fig. 8.2.7, the absence of an oxidation process in a nanoporous sample produced with 1 mA/cm^2 etching current density and other standard parameters, properly dried (see section 2.3.) and left in air for at least 150 min after preparation is presented.

An expected result is presented in fig. 8.2.8. This shows that a sample exposure of about

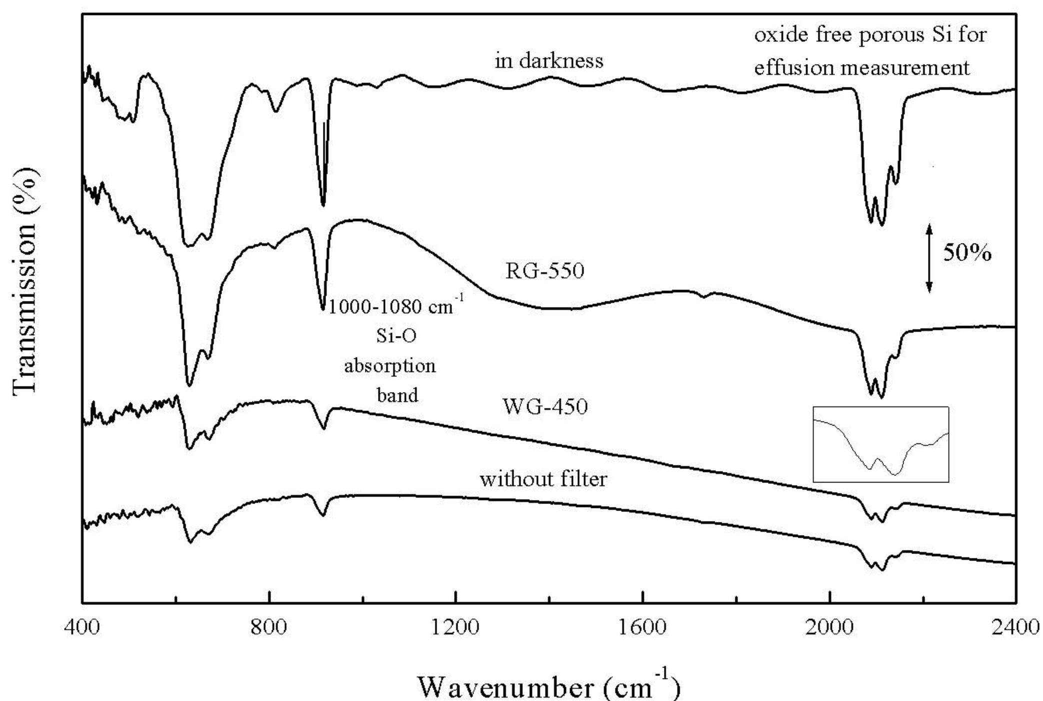

Fig. 8.2.6: Comparison between infrared spectra of samples, produced under illumination through different filters (RG-550, WG-450).

30 min in air followed by about 30 min under low vacuum and subsequently relatively long staying of 20 hours under high vacuum $\left(\sim 10^{-8}\ \text{Torr}\right)$ before beginning the thermal effusion process doesn't lead to any oxidation.

The oxidation caused by a rinse of the porous sample in ethanol immediately after preparation is illustrated on fig. 8.2.9.

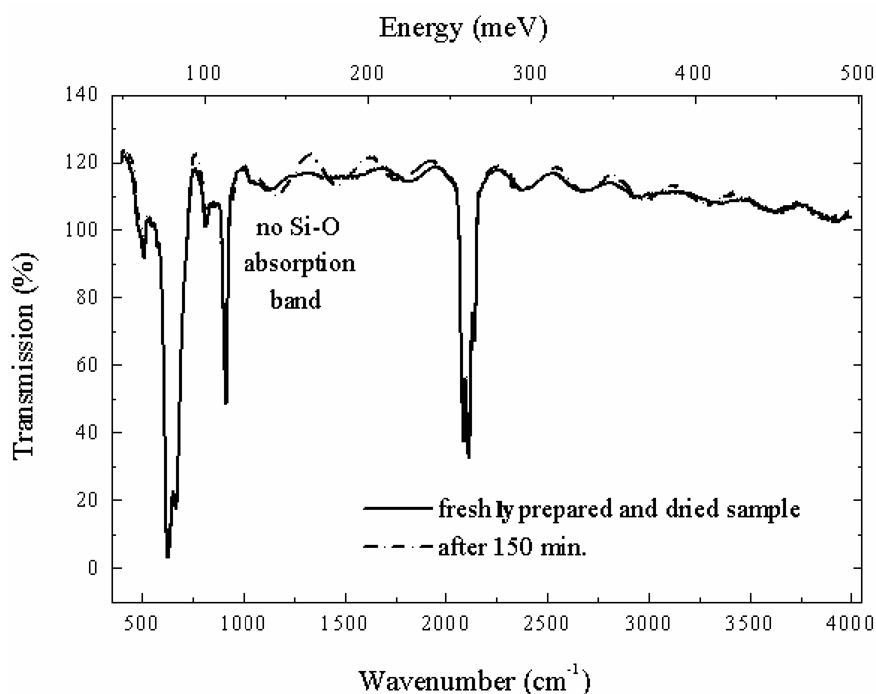

Fig. 8.2.7: Oxide-free sample 150 min after preparation and correct treatment.

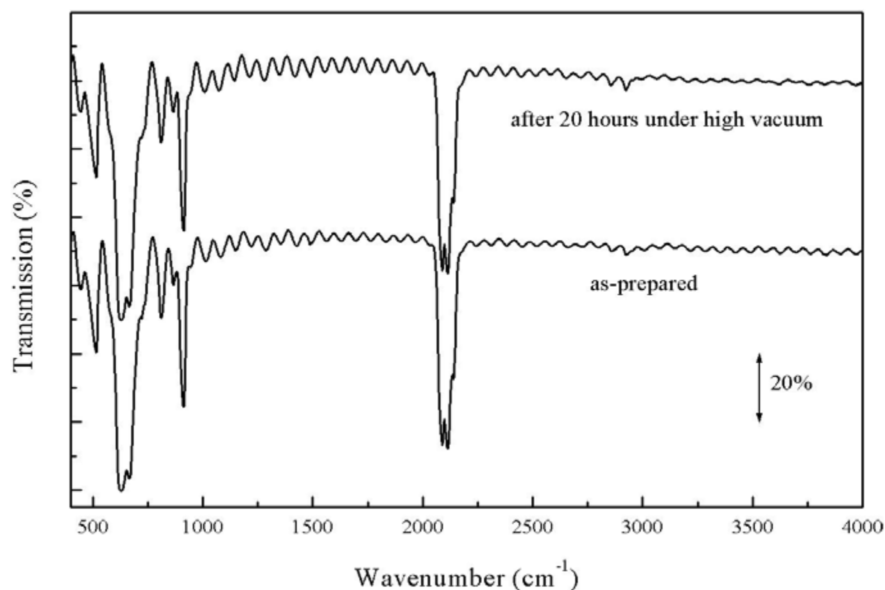

Fig. 8.2.8: Evidence for an oxide-free sample after 20 hours remaining under high vacuum.

The infrared spectroscopy can also be helpful in clarifying the question of whether the whole hydrogen quantity leaves the sample after the thermal effusion. Fig. 8.2.10 shows two spectra of a freestanding mesoporous sample taken immediately after preparation and after the effusion procedure respectively.

8.2.4. Comments

In order to assign the vibrational absorption features, we will compare our results to those

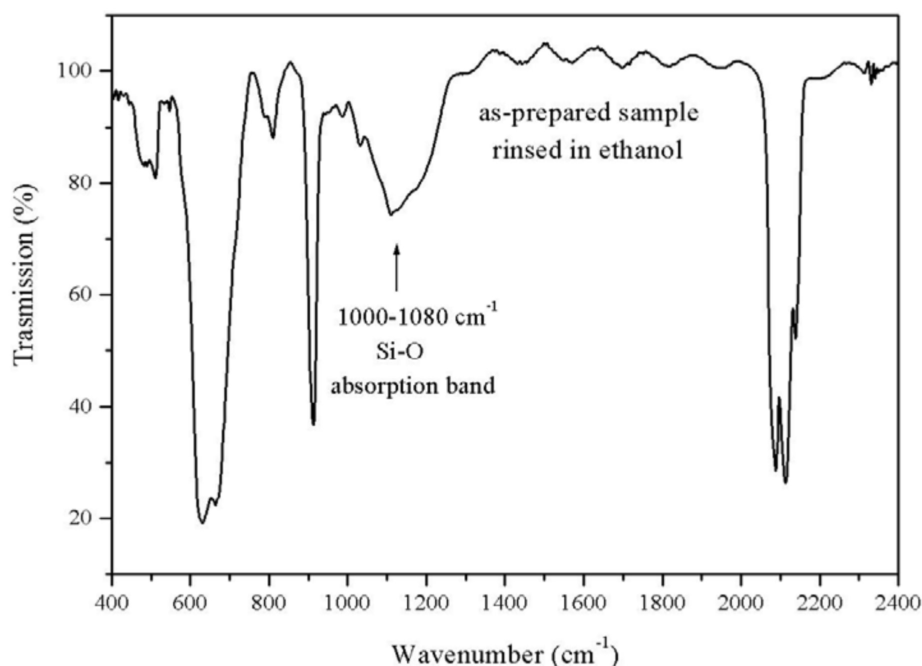

Fig. 8.2.9: Oxidation caused by rinsing of an as-prepared sample in ethanol.

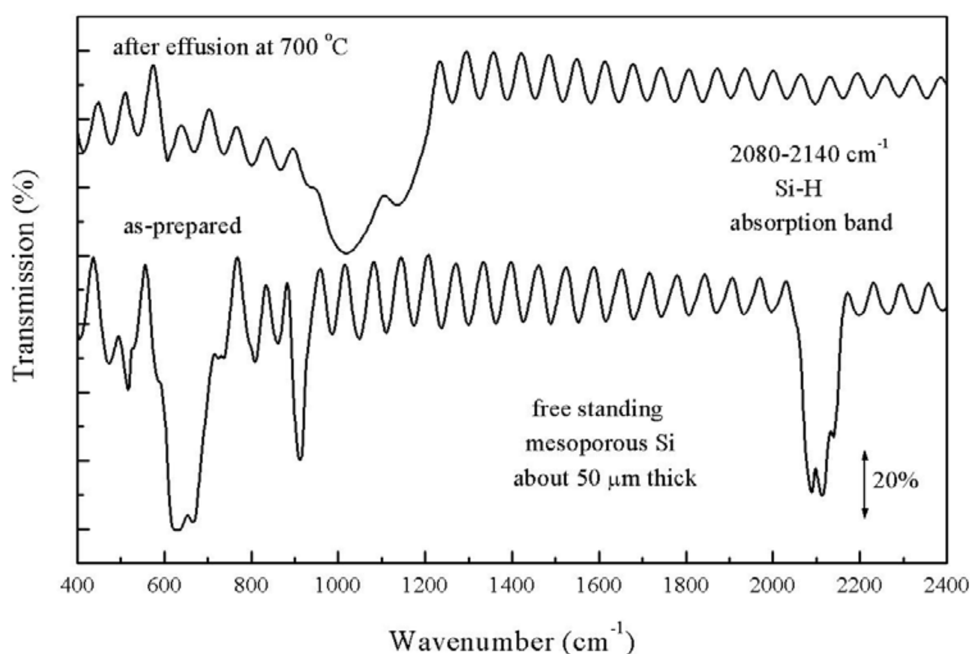

Fig. 8.2.10: Comparison of as-prepared and completely hydrogen-free after effusion at 700 °C mesoporous sample

obtained for porous silicon by *ab initio* calculations for model clusters and previously reported experimental results for amorphous silicon, porous silicon and for flat and stepped, variously oriented silicon surfaces. For the *ab initio* method used in our case, it is essential that the behaviour of a certain group of atoms is studied as a molecule but the arrangement of that group with respect to the crystal and its influence on the vibrational frequencies is not taken into account. Not every feature in the whole spectrum will be commented upon but only those, which are directly connected with the aim of the current work.

It has to be mentioned that the problem of hydrogen chemisorbed on silicon is complicated and the data in the literature is very controversial.

We strove to determine what kinds of species were present by first examining the silicon-hydrogen stretching vibrations band. By preparing porous silicon, which contains predominately deuterium and a small amount of hydrogen, we can isolate Si-H stretching vibrations. We have found 3 peaks in the Si-H stretching region, as can be seen in the area near 2100 cm^{-1} in fig. 8.2.4-d) and fig. 8.2.4-f). In an experiment where there is only a small amount of deuterium, we found the corresponding isolated silicon-deuterium stretches and this is shown in the expanded scale near 1500 cm^{-1} in fig. 8.2.4-b) and fig. 8.2.4-e). This gives us 3 pairs of stretching vibrational frequencies with the approximately correct Si-H/Si-D hydrogen-deuterium isotopic ratio $\sqrt{\frac{\mu_{Si-D}}{\mu_{Si-H}}} = 1.39$, where μ is the reduction mass of the $Si-H(D)$ group: $2084/1517 = 1.37$, $2112/1532 = 1.38$, and $2142/1555 = 1.38$. This result can be considered as a proof that it is a matter of stretching vibrations and that the band is

correctly assigned. In this way, we concur with the conclusions of Beckmann [see *Beckmann*] and the results from *ab initio* calculations [see *Burrows*, *Chabal1*]. It has to be emphasized that in the whole literature on porous silicon or hydrogen terminated silicon surfaces such an assignment is undisputed. More complicated and controversial is the question of how to correlate the silicon-hydrogen species to particular stretching vibrations. To obtain information on this, we need to consider the other vibrational motions and the 'hydrogen effusion-DF dip' experiments.

Recent *ab initio* calculations [see *Ogata*] can guide us with approximate peak positions for the strongest infrared absorption features both of the stretching band and of the other vibrational modes between 400 and 1000 cm^{-1}. The calculations give: SiH bend at 689 cm^{-1}, SiH_2 scissors at 915 cm^{-1}, SiH_2 wag at 737 cm^{-1}, SiH_3 d-deformation at 930 cm^{-1}, SiH_3 s-deformation at 894 cm^{-1}, SiH stretching at 2092 cm^{-1}, SiH_2 stretching for both symmetric and asymmetric modes at 2110 cm^{-1} and SiH_3 s-stretching at 2131 cm^{-1} and d-stretching at 2129 cm^{-1}.

The 'hydrogen effusion-DF/D_2O dip' experiment is a second source of additional information. We expect the Si-H species to be the most stable with respect to temperature annealing and the peaks at 2088 and 626 cm^{-1} do indeed remain the longest in the effusion series which links them, as shown in fig. 8.2.5. There exists an opinion based on an early investigation of single-crystal silicon [see *Collins*] that the 626 cm^{-1} peak could originate from a Si-Si stretching vibration. The infrared spectrum in fig. 8.2.4-d), obtained for a fast completely deuterium-terminated sample does not contain this peak, which is at variance with such a contention. Theory also opposes the opinion since vibrations of the silicon lattice are not accompanied by a polarization. Other authors [see *Harwood*, *Gupta1*] attribute it to a Si-H bending mode. This supposition strengthens the statement that the peak at 2088 cm^{-1} is also due to monohydride species.

We expect that, as the SiH_3 species are the least stable with respect to temperature (see section 8.1), their vibrational mode will be the first to vanish from the stretching region as the effusion temperature is increased. This presumption, the theoretical *ab initio* calculations and the experimental fact that the bluest of the stretching vibrations have already started to disappear in the 598 K experiment, guide us to assign the peak at 2141 cm^{-1} to the SiH_3 asymmetric or (and) symmetric stretching vibrations. The last assumption leaves us with the middle peak containing the SiH_2 symmetric or (and) asymmetric stretching frequencies. According to the *ab initio* calculation, these should be obtained degenerate at 2110 cm^{-1}.

A cause for concern in our explanation of the infrared spectra is the effusion experiment at

648 K, where the presumed SiH_2 "scissors" peak at about 905 cm^{-1} (calculated to be at 915 cm^{-1}) has almost vanished while the SiH_2 stretching peak remains very strong. A closer examination of the last peak shows that it is red shifted to 2104 cm^{-1}. We also note that there is broad absorption between 1000 and 1100 cm^{-1}, indicating that oxygen contamination is present. It is known [see *Theiß*] that oxygen atoms attack the backbonds of the first silicon layer instead of breaking the more stable Si-H bonds. As a result, such oxygen can shift the Si-H stretch to the blue [see *Kato*], so we attribute this extra intensity in the dihydride-stretching region to oxygen induced blue shift of the Si-H stretch. The reason for the presence of such oxygen contamination is rooted in the impossibility of the dip in DF/D_2O (or $(50\ \%)HF$) solution to completely remove the oxide from the porous structure. The oxidation takes place when the sample comes into contact with air after the effusion process. In our approach, such contact is an unavoidable drawback. There are authors [see *Gupta1*, *Mueller*] who have carried out a similar thermal annealing experiment. This experiment differs from our investigation inasmuch as the sample lies in a high vacuum (~10^{-8} Torr) permanently and the infrared measurements are performed under these vacuum conditions. Such a variant of the experiment has the advantage that the sample never oxidizes through the annealing and the following cooling. The authors present data, which shows that after annealing at a high temperature (from about 650 K to about 780 K) the only peak remaining is that at about 2111 cm^{-1}, or the central peak. This last information reinforces the statement that this peak originates from monohydrides. The reason two completely contradictory results can be obtained from two such similar experiments (ours and the alternative considered) lies, in our opinion, in the handling of the samples. In both cited publications, samples, which are rinsed in ethanol after preparation (see fig. 8.2.9), were investigated. The spectra presented as typical for freshly prepared porous silicon in these publications showed, in our opinion, that the samples were oxidized as a consequence of the rinse. On the other hand, it is accepted in the literature [see *Kato*, *Gupta2, Fuchs*] that the oxygen back bonding of silicon causes a shift in the stretching modes of the hydrides to higher values. There is a discrepancy in the reported values [see *Kato*, *Fuchs*] concerning the positions of the shifted vibration frequencies. In the case that the value of 2127 cm^{-1} is valid (see fig. 8.2.2), it is possible that the only remaining peak could originate not from normal monohydrides but from oxygen back-bonded monohydrides. The latter indirectly supports the assignment of the peak at 2088 cm^{-1} as an original monohydride. To conclude, we emphasize that in both similar experiments oxidized porous structures are investigated. However, the oxidation takes place at different stages of the study. The discrepancies in assignment of the peaks are founded on the different degrees

of oxidation – merely contamination in the first case but a nearly complete oxidation of the skeleton surface in the second.

Further work must be done at higher resolution in order to determine the positions of the symmetric and asymmetric stretches of SiH_3. In our measurements (see fig. 8.2.5), this unresolved peak correlates with the presumed SiH_2 scissors mode at about 905 cm^{-1}. Both peaks decrease as the effusion temperature increases which indicates the participation of a SiH_3 d-deformation mode (calculated to be at 930 cm^{-1}) component in the peak at 905 cm^{-1}. It is conceivable that the last peak also correlates with the second peak of the stretching band but is not evident because the dihydride stretch is covered by the stretch of the oxygen back-bonded monohydride, thus rendering it impossible to follow its behaviour. There are authors [see *Gupta1*] who associate the third peak of the considered band at about 2141 cm^{-1} with the first one at about 2088 cm^{-1} and assign them as dihydride s-stretch and a-stretch, respectively. Such an interpretation is connected with the results from the above-commented upon annealing experiment. Theiß [see *Theiß*] agrees with the possibility that the third peak can be attached to the trihydride stretch but also supposes that the observed feature is likely to be a mixture of dihydride and trihydride stretches. Furthermore, it is not completely comprehensible why the third peak at about 2041 cm^{-1} is available even after effusion at 698 K. The SiH_3 s-deformation mode at 894 cm^{-1} predicted by the *ab initio* calculations, which should be strongly infrared active and consequently useful for solving the problem, has not been observed.

The peak at about 655 cm^{-1} is obviously temperature dependent and is already barely recognizable even after thermal effusion at 623 K. This peak is also dependent on the isotopic substitution and its intensity decreases with increasing deuterium participation. In the sample prepared with DF and d-ethanol, it is completely absent. Moreover, the correlation with the peak at about 905 cm^{-1} is obvious, which justifies the assumption that it originates from dihydrides or from trihydrides. The *ab initio* calculation gives the value of 737 cm^{-1} for the dihydride wagging mode and other authors [see *Theiß*, *Fuchs*] find the same dihydride deformation vibrational mode at 660 cm^{-1} and 640 cm^{-1} respectively. The nearest peak, which *ab initio* calculation predicts for trihydride, is the rocking deformation mode at 556 cm^{-1} but this is only very weakly infrared active and consequently drops out as a competitor.

The feature existing in the spectra of a freshly prepared sample at about 800 cm^{-1} couldn't be identified on the basis of the *ab initio* calculation and the literature on porous silicon is also not of service [see *Ogata*, *Fuchs*]. For the aim of this work, it is important that this feature be present in all spectra and that it be almost unaffected at the higher temperatures utilized or by

the isotopic substitution. This is in controversy with the only publication [see *Demichelis*] where a feature at $805\,cm^{-1}$ is assigned as SiH_3-bending mode. This consideration as well as data in the literature concerning silicon bonds [see *Pretsch*] is an indication that it is possibly a matter of Si-F stretching vibrations. The problem needs further clarification.

In our opinion, it would be useful to perform an experiment combining the advantages of the oxide-free sample handling after preparation and thermal effusion and infrared measurements in a high vacuum. We do not have suitable equipment for such an experiment.

The large number of publications from Chabal and coworkers [see e.g. *Chabal2*, *Chabal3*, *Chabal4, Jacob1, Chabal5, Jacob2*] on hydrogen chemisorbed on flat and stepped variously oriented silicon surfaces can be also used for guidance. They assert that for different surface orientations the stretching band can generally be divided into three parts. The region from about 2070 to about 2095 cm^{-1} contains peaks arising from monohydrides, the features in the region from about 2100 to about 2120 cm^{-1} are connected with dihydrides and the region from about 2130 to about 2135 cm^{-1} is attached to trihydrides. The authors [see *Jacob1*] are of the opinion that "to optimize the chances of proper interpretation, an effort has to be made to prepare surfaces that are microscopically as homogeneous as possible (given an overall macroscopic orientation)". Further, they deem there to be ". . . a higher probability for samples with high step densities than for flat samples to have metastable, strained structures due to various interactions (steric constraints, variations in backbond lengths, etc.…). Such interactions may cause large frequency shifts for the interacting species, complicating the assignments." We take the view that these citations express, with great accuracy, the complexity of the problem of feature assignment in porous silicon. The stepped surfaces and the different reconstructions are characterized by changing the positions and the relative intensities of the already known peaks or causing the appearance of new ones.

Because of the irregular structure of the internal porous silicon surface (see below) and the local environmental influence, deviations from the above-presented values are not unexpected.

It is indicative that there are authors [see *Theiß*, *Frohnhoff*] who, in various publications, show an evolution concerning their understanding of feature assignments in the stretching band. In the first cited work, a model based on Gauss-distributed harmonic oscillators is presented. This approach is applied to generate the dielectric function of the freshly prepared porous silicon by using the reflectance spectrum and a parameter fitting. It has to be emphasized that it is possible only to characterize the features by this method but not to assign them.

In view of all presented considerations, it is clear that only the existence of three areas in the stretching vibration region can be accepted unconditionally. Nevertheless, for the current work, this region plays a certain role. In our opinion, it is clear that, in the situation presented, the problem still awaits a complete solution.

The infrared spectroscopy enables the whole procedure connected with the effusion measurement to be evaluated. First, it opens up the possibility of investigating the important problem associated with the presence of oxide in the porous silicon structure. As already mentioned, oxidation of the sample shifts the luminescence peak position (see section 7.2). An oxidation of the internal surface can also influence the thermal effusion results. Therefore, it is of primary importance that the oxidation process be avoided for an adequate characterization of the porous structure to be derived.

The results presented (fig. 8.2.7) for the oxidation process of a sample stored in air at room temperature and normal humidity shows that for duration of at least 1 hour (with a reserve for an increased moisture content) the samples remain free of oxide.

Additionally to the air storage, there is also a relatively short time (about 30 min) of storage at low vacuum in the effusion installation and a necessarily longer time (greater than 12 hours) at high vacuum. The period at low vacuum can exert only a moderate influence on the oxidation. A sample, which undergoes the whole cycle before the actual effusion measurement, is compared with a freshly prepared sample to confirm that it remains free of oxide (fig. 8.2.8).

Making use of infrared spectroscopy also contributes to the ability of the treatment of the sample after preparation to be characterized. The effect of the rinse with alcohol immediately after preparation is shown in fig. 8.2.9. The appearance of a distinctly expressed band in the region $1000 \div 1100$ cm^{-1} proves there is strong oxidation. Therefore, for experiments in which the oxidation of the porous structure is harmful, the rinse must be avoided. As an alternative, the procedure described in section 2.3 can be used.

All these considerations support the conviction that the samples remain free of oxide until the actual effusion measurement.

Another aspect of the effusion experiment is evident from fig. 8.2.10. The comparison presented between the infrared spectrum of a freshly prepared sample and the spectrum of the same sample after thermal effusion at 700 ^{o}C clearly depicts the absence of any feature in the Si-H stretching region for the second case. This is evidence that the whole quantity of hydrogen has been released from the sample in the observed experiment.

The infrared spectroscopy can be helpful in investigating the skeleton surface orientation

and disorder. Many authors [see *Gupta1*, *Schuppler*] maintain the opinion that this surface is (100)2x1 (or equivalent (010) and (001)) oriented and correspondingly reconstructed. The justification for this hypothesis is the similarity between the infrared spectra of a silicon surface so oriented and of the porous silicon internal surface and the given thermodynamic explanation for why the hydrogenated Si(100) would be favoured during the porous-silicon formation process. Schuppler et al. [see *Schuppler*] take the view that the appearance of (110) or (111) orientations would exhibit peaks in the Si-H stretching region which are mainly associated with SiH species. In our view, this is more valid for a mesoporous structure, where the particles are larger and the internal surface has a relatively small density of steps per unit area. With the reduction of particle size, the number of the Si atoms, which lie on edges and at corners, grows. The investigations of Chabal et al. [see *Chabal1, Jacob3*] on stepped surfaces show that even at (111) orientation, where the flat surface is terminated exclusively by monohydrides, the infrared spectrum is strongly influenced by the steps. In the stretching region, three peaks with comparable magnitudes appear. When the distance between the edges becomes of the order of two or three interatomic distances (≈ 5-6 Å), which is normal for particles with a diameter of about 30-40 Å, it is difficult to speak about the occurrence of oriented planes. Additionally, the interaction between the edges enhances the disorder. At higher etching-current densities (and correspondingly stronger external electrical fields) it is conceivable that the thermodynamic restrictions, which demand the appearance of certain planes, are less pronounced. In our opinion, any statement concerning certain reconstructions is doubtful if every orientation is possible. Besides, the structures are not experimentally distinguishable if all orientations appear on the surface or the etching process attacks the Si atoms completely randomly and the etching procedure leaves behind a surface without any long-range order. Figuratively, it may be pictured as a bend of the surface and can effectively be described as a curved surface. The change of the radius of the surface curvature can be evaluated from the ratio of the monohydrides to the dihydrides (see chapter 9).

Because of the complicated form of the internal surface, a certain disorder in the orientation of the bonds with respect to the surface, which will influence the characteristic vibrational frequency, is to be expected. The latter is because there are bonds with different vicinity, which determines the local electrical field and ultimately the characteristic frequency. The works of Lucovsky et al. [see *Lucovsky*] and Cardona [see *Shanks*, *Cardona*] on amorphous silicon are helpful in estimating the level of the disorder. In the presented infrared spectra, it is noticeable that the half-width of the observed features, e.g. in the stretching region, has a value of about 100 cm^{-1}. Both for crystalline material and for porous

silicon, this value is about 20 cm^{-1}. Furthermore, for the monohydride stretching mode, the presence of a peak at about 2000 cm^{-1}, which is absent in the spectrum of the porous silicon material, is reported. These two experimental facts show that the disorder of the surface is not comparable with that of the amorphous material but is considerably smaller.

An additional possibility for examining the features assignment and to obtain information about the correlation between the different hydrides on the skeleton surface gives the series shown in fig. 8.2.6. Here, the infrared spectra of as-prepared samples produced under illumination are presented. Both the maximum position of their luminescence spectra (see fig. 7.3) and their effusion data (see section 4.3.4) differ significantly. We have also tried to find some manifestation of these features in their infrared spectra. The observed triplet in the $Si\text{-}H_x$ stretching region is unambiguous proof of the presence of hydrogen in the porous silicon. The triplet can be deconvoluted and the areas under the peaks obtained can be determined and compared. It is expedient to convert the transmittance into absorbance (see eq. 8.2.2) in view of its proportionality to the concentration of absorbing bonds. Because of the inhomogeneous random distribution of the bonds caused by the complex form of the skeleton surface, we assume a Gauss form for the absorbance features. The plausibility of such a supposition is also confirmed by the very good fit obtained from a deconvolution of some of the experimental curve features by Gauss functions. Our attempt to perform a deconvolution, which resolved the three evident peaks, did not give sufficiently satisfactory results. Careful observation reveals a shoulder on the low frequency side of the composite waveform, which suggests a further significant peak. As can be seen from the agreement between the measured waveform and the composite of a four gaussian-distribution peak deconvolution illustrated in figure 8.2.11, a four peak deconvolution is much more successful. The example shown is for a sample illuminated through a 550nm wavelength cut-off low pass filter and the fit can be seen to be almost perfect.

An unambiguous assignment of the peaks obtained didn’t succeed. The result shows that two of the peaks, at about 2082 and about 2111 cm^{-1} respectively, are more clearly pronounced than the other two. We will concentrate first on those two peaks, which, with a great probability, characterize different hydrogen bonds independently of their less than unambiguous assignment. Having in mind the received concept for the skeleton surface orientation, the number of mono- and dihydrides strongly dominates that of the trihydrides, which can appear only on the corners. Because of this, it is natural to connect the two peaks with mono- and dihydride, although it is not absolutely certain whether the modes are pure or are a superposition of different modes. To compare the areas lying under the peaks, the ratio

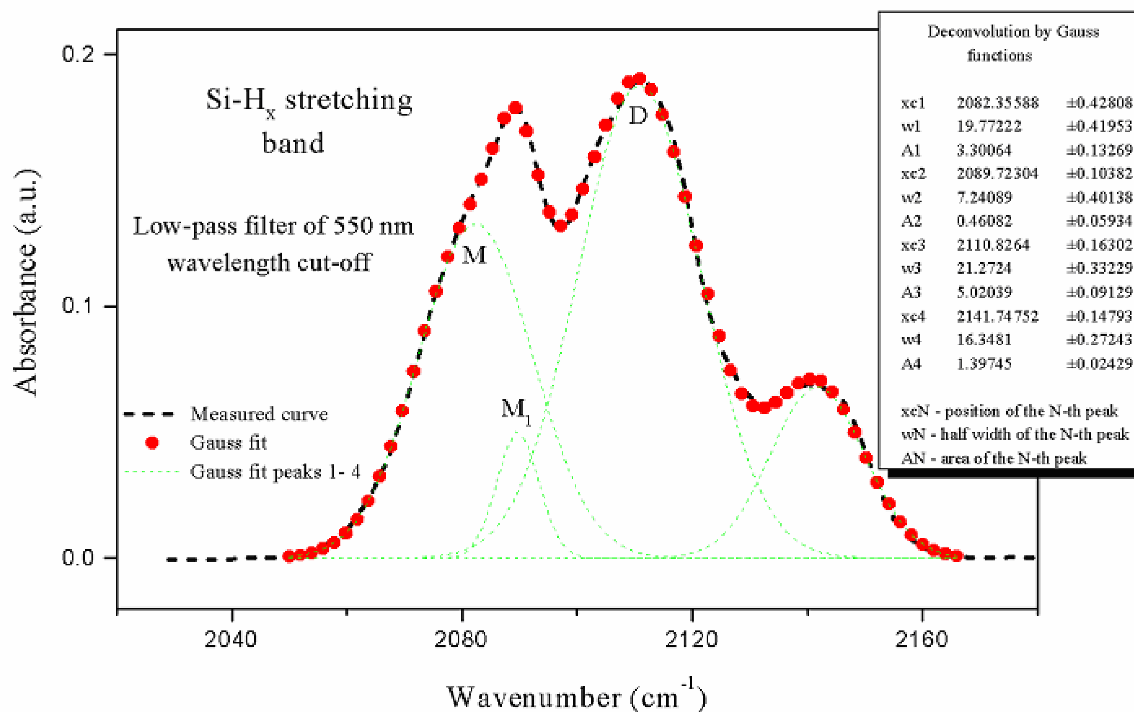

Fig. 8.2.11: Illustration of the stretching band deconvolution for the sample prepared under light-assisted anodization through low-pass a filter with a wavelength cut-off at 550 nm. (M – peak at 2082 cm^{-1}, M$_1$ – at 2089 cm^{-1}, D – at 2111 cm^{-1})

S_M/S_D is formed, where $S_{M(D)}$ is the area under the peak at about 2082 (2111) cm^{-1} (see fig. 8.2.11).

It can be shown (see eq. 8.2.2) that the area considered is directly proportional to the product of the matrix element characteristic of each transition (maximum) squared and the absorbing bond concentration. The different thicknesses of the samples do not matter since the vibrational modes being compared belong to one and the same curve. Consequently, the ratio S_M/S_D is proportional to the ratio of the corresponding matrix elements squared multiplied by the ratio of the absorbing bond concentrations. This ratio can be formed for each infrared spectrum in the series considered. It is plausible to assume that the ratios of the two matrix elements in all spectra in this series are equal. Applying such an assumption, the comparison between the S_M/S_D ratios for all curves of the series is actually a comparison between the concentration ratios of the two bond types for each sample. In other words, if the values of the S_M/S_D ratios for two curves of the considered series differ, the difference is due only to a change in the correlation between the two bond types.

Having in mind these considerations, it is plausible to follow the behaviour of the ratio S_M/S_D in the investigated series (table 8.2.1). The results from an analogous study by the thermal effusion method justify the expectation of a clear evolution in the direction of an enhancement or a decrease of the ratio values (see tab.8.1.1). In our case, the tendency is

variable. From sample A (see the designations in tab.8.2.1) to sample B, a decrease of the value is seen and for the last two samples (C and D) it remains constant and higher than that of the first samples. A possible explanation for this could be that one of the two peaks represent not pure mode but a mixture of modes and the considered areas cannot be used as a measure of the correlation between the two bond types in the different samples.

Another possibility for comparing different hydrides is to look at the correspondence between the pair of peaks at about 915 cm^{-1} and about 2082 cm^{-1}. The first of these peaks is chosen as representative of the dihydride and the second is presumed to be the monohydride stretch. Designating by S_S, the area under the peak at about 915 cm^{-1} for the ratio S_S/S_M, an increase from sample A to sample B and then a decrease to sample D is obtained. In other words, once again, no clear tendency can be viewed. A possible explanation for this observation is the increased role of the surface reconstruction in samples C and D. In case of a surface reconstruction in reality takes place a process of transformation of a certain number of dihydrides to monohydride-like bonds (dimers). A manifestation of such a reconstruction could be the small peak M_1 in the deconvolution of the stretching band. If we assume that the small peak at about 2089 cm^{-1} is due to these monohydride-like bonds, then the ratio S_S/S_{M_1} must express the manner in which the concentration of the unreconstructed bonds relates to that of the reconstructed bonds. One basis for such a supposition is the results of Chabal's group [see *Burrows, Chabal1, Dumas*, *Jacob1*], according to which, the peak of the unreconstructed monohydrides occupies almost the same position irrespective whether the bonds are on (100) or (111) surfaces. The absorption peak of the reconstructed monohydrides also lies in the monohydride region but is shifted a few cm^{-1} higher with respect to the position of the unreconstructed monohydride. What we observe is an increase of the

Area ratio	Sample			
	Dark (A)	**RG-550 (B)**	**WG-450 (C)**	**Without filter (D)**
S_M/S_D	0.71	0.66	1.02	1.02
S_S/S_M	0.85	1.44	0.86	0.72
S_S/S_{M_1}	6.00	10.33	10.28	7.02
S_S/S_D	0.60	0.95	0.88	0.61

Tab. 8.2.1: Areas ratio of the characteristic infrared peaks for the "light-assisted " series: S_M - area under the peak at about 2084 cm^{-1}, S_D - area under the peak at about 2111 cm^{-1}, S_S - area under the peak at about 915 cm^{-1}, S_{M_1} - area under the peak at about 2088 cm^{-1}.

considered ratio from sample A to sample B, conservation of the value nearly persistent to sample C and then a decrease to sample D. Again a clear tendency is not present. It is evident that an unambiguous explanation is difficult to find and that the peak at about 915 cm^{-1} is most probably the result of a mixture of different modes.

A test for the regularity of the peak assignment is to observe the ratio S_S/S_D. If the two corresponding peaks originated from dihydride absorption alone, then the considered ratio should be constant for all of the samples. It should be equal to the quadratic ratio of the two matrix elements characterizing the energetic transitions occurring for the scissors motion and the stretching motion respectively. What we observe is an increase from sample A to sample B, a small decrease to sample C and a further decrease to sample D. All values lie in the region of about ±25% with respect to the average value. One possible reason could be that the two considered peaks, or at least one of them, are associated not only with dihydrides but are also mixed with other components, e.g. trihydride s-deformation mode for the peak at about 915 cm^{-1}. The contribution of these components to the considered area is different for each sample.

On other hand, if the assignment is correct and both considered peaks are associated only with dihydrides, the areas ratio could be a measure for the change of the matrix elements ratio. The only cause, in our opinion, for such a change could be the different surface to volume ratio of the skeleton in the various samples and the associated local environment of the bonds (see tab. 4.4. and section 9.1.). From sample A to sample D, the change of the quadratic matrix element ratio has no fixed direction, whereas the surface to volume ratio increases according to the effusion data. The different ways in which the quadratic matrix element ratio and the surface to volume ratio change lend more support the hypothesis of mixed modes.

The analysis of the “light-assisted” series could be additionally complicated if one bears in mind the following considerations. W. Theiß [see *Theiß1*] is of the opinion that the interpretation of the absorbance being proportional to the concentration of the absorbing species is correct only if the reflectivity of sample and reference are the same and no interference patterns occur.

The meaning of the above-presented study is to illustrate the problems connected with interpretation of the infrared data for porous silicon structures. By making an attempt at a quantitative characterization, we show the limitations of this method at the present state of affairs. The absence of a clear tendency in the infrared data for the considered series, in contrast to the effusion and luminescence data, is indirect evidence of the complicated

influence of the complex internal surface of porous silicon on the hydride vibrational frequencies. This supports the hypothesis for mixed vibrational modes, which makes their assignment difficult.

8.2.5. Conclusions

- Independently of the improved conditions for investigating unoxidized porous structures, their infrared transmission spectra remain incompletely understood and need further research.
- It is not clear whether the observed modes are single or mixed due to the influence of the complex internal surface over the vibrational frequencies.
- The samples investigated by us were free of oxide.
- At least 2 hours after preparation, the properly treated as-prepared samples remain free of oxide in air.
- There is no evidence that the internal surface is perfect or homogeneously oriented.
- The disorder of the surface is not comparable with that of amorphous material but is considerably smaller.
- It is not experimentally distinguishable whether all orientations appear on the surface or the etching process attacks the Si atoms completely randomly and the etching procedure leaves behind a surface without any long-range order.
- Figuratively, a bend of the skeleton surface is imaginable and can effectively be described as a curved surface.

References

1. *Theiß* W. Theiß, Surface Science Reports **29**, 91 (1997).
2. *Beckmann* K.H. Beckmann, Surf. Sci. **3**, 314 (1965).
3. *Burrows* V. A. Burrows, Y.J. Chabal, G.S. Higashi, K. Raghavachari, and S.B. Christmann, Appl. Phys. Lett. **53**, 998 (1988).
4. *Chabal1* Y.J. Chabal, G.S. Higashi, K. Radhavachari, and V. A. Burrows, J. Vac. Sci. Technol. A 7, 2104 (1989).
5. *Ogata* Yukio Ogata, Hiroyuki Niki, Tetsuo Sakka, and Matae Iwasaki, J. Electrochem. Soc. **142** (1), 195 (1995).
6. *Collins* R.J. Collins and H.Y. Fan, Phys. Rev. **93**, 674 (1954).
7. *Harwood* P.B. Harwood and G. P. Thomas, in Materials Issues in Silicon Integrated Circuit Processing, Mat. Res. Soc. Symp. Proc. **71**, Pittsburgh, 1986.
8. *Gupta1* P. Gupta, V.L. Colvin, and S.M. George, Phys. Rev. B **37** (14), 8234 (1987).

9. *Kato* Y. Kato, T. Ito and A. Hiraki, Jpn. J. Appl. Phys. **27** (8), 1406 (1988).

10. *Mueller* Frank D. Mueller, Dissertation am Physik-Department der Technischen Universitaet, Muenchen (1993).

11. *Gupta2* P. Gupta, A. C. Dillon, A. C. Bracker, and S.M. George, Surf. Sci. **245**, 360 (1991).

12. *Fuchs* H.D. Fuchs, M. Stutzmann, M.S. Brandt, M. Rosenbauer, J. Weber, A. Breitschwerdt, P. Deak, and M. Cardona, Phys. Rev. B **48** (11), 8172 (1993).

13. *Demichelis* F. Demichelis, G. Crovini, G.F. Pirri, E. Tresso, A. Rubino, G. Nobile, E. Terzini, and G. Conte, Mat. Res. Soc. Symp. Proc. **297**, Pittsburg, (1993)

14. *Pretch* in “Tabelen zur Strukturaufklärung organischer Verbindungen mit spektrosko- pischen Methoden“, Pretsch, Clerk, Seibl, Simon , Springer-Verlag, Berlin Heidelberg New York, 1976, p.I255.

15. *Chabal2* Y.J. Chabal and Krischnan Raghavachari, Phys. Rev. Lett. **53**(3), 282 (1984).

16. *Chabal3* Phys. Rev. B **28** (8), 4472 (1983).

17. *Chabal4* J. Vac. Sci. Technol. A **3** (3), 1448 (1985).

18. *Jacob1* P. Jacob and Y.J. Chabal, J. Chem. Phys. **95**(4), 2897 (1991).

19. *Chabal5* Y.J. Chabal, Journal of Molecular Structure **292**, 65 (1993).

20. *Jacob2* P. Jacob, Y.J. Chabal and Krishnan Raghavachari, Journal of Electron Spectroscopy and Related Phenomena **64/65**, 59 (1993).

21. *Frohnhoff* St. Fronhoff, R. Arens-Fischer, T. Heinrich, J. Fricke, M. Arntzen, W. Theiß, Thin Solid Films **255**, 115 (1995).

22. *Schuppler* S. Schuppler, S.L. Friedman, M.A. Marcus, D.L. Adler, Y.-H. Xie, F.M. Ross, Y.J. Chabal, T.D. Harris, L.E. Brus, W.L. Brown, E.E. Chaban, P.F. Szajowski, S.B. Christman, and P.H. Citrin, Phys. Rev. B **52**(7), 4910 (1995).

23. *Jacob3* P. Jacob, Y.J. Chabal, Krishnan Raghavachari, and S.B. Christman, Phys. Rev. B **47**(11), 6839 (1992).

24. *Lucovsky* G. Lucovski, R.J. Nemanich, and L.C. Knights, Phys. Rev. B **19** (4), 2064 (1978).

25. *Shanks* H. Shanks, C. J. Fang, L. Ley, M. Cardona, F.J. Demond, and S. Kalbitzer, phys. Stat. Sol. (b) **100**, 43 (1980).

26. *Cardona* M. Cardona, phys. Stat. Sol.(b) **118**, 463 (1983).

27. *Dumas* P. Dumas, J.Y. Chabal and P. Jacob, Surf. Sci. **269/270**, 867 (1992).

28. *Theiß1* W. Theiß, in: Porous Silicon Science and Technology, Eds. J.-C. Vial and J. Derrien (Springer, Berlin/Les Editions de Physique, France, 1995) p. 189.

Chapter 9. DIMENSIONS OF THE PARTICLES FORMING THE SKELETON

9.1. Determination of Particle Size from the Experimental Data

It is a long and uncertain path from the experimental determination of the N_H/N_{Si} ratio to an estimation of particle size. One important step on the route is necessarily speculative. The main method utilized, thermal desorption at a constant temperature and gravimetry coupled with the supplementary methods of ERDA, "burning" and EXAFS, delivers information about the hydrogen to silicon atom number ratio. The variety of methods used helps to make the experimental results more reliable.

Based on its single crystal structure and knowledge of the weight of the skeleton, one can obtain the skeletal volume in the following manner. The gravimetric method, through the weight, also gives the entire number of the silicon atoms, N_{Si}, in the porous structure (see section 4.1). The lattice constant of the silicon monocrystal is $a_{Si} = 5.43095\ \text{Å} \approx 5.43x10^{-10}\,\text{m} = 5.43x10^{-8}\ \text{cm}$ [see *Sze*]. $V_{uc} \approx 160.187x10^{-24}\ \text{cm}^3$ is the volume of the unit cell. Assuming the lattice to be composed of a three-dimensional net of unit cells and bearing in mind that the unit cell of the Si crystal is face-centered cubic, the following calculation can be made for the Si atoms pertaining to the unit cell:

$$2\left(8x\frac{1}{8}+6x\frac{1}{2}\right)=8 \tag{9.1}$$

where 8 is the number of atoms at the corners, 6 the number on the walls and 2 is the number of the basis atoms. Introducing the elementary volume, V_e, which corresponds to each lattice atom and is also cubic, we obtain $V_e \approx 20x10^{-24}\ \text{cm}^3$. Having the total number of Si atoms, N_{Si}, one can calculate the entire volume of the skeleton:

$$V = N_{Si}V_e\,. \tag{9.2}$$

The number, N_H, of hydrogen atoms delivered by thermal effusion at a constant temperature (see section 3.2.3.) can be translated into an area only if the density of H atoms per unit area is known. The type of hydride coverage has a substantial impact on the calculation of the area under consideration. The thermal effusion as the temperature is ramped and the infrared transmission measurements give information about the orientation, and ultimately the population, of the internal porous structure's surface structures . In our opinion, the results from each method can be interpreted in two ways, which are not experimentally

distinguishable. Either all orientations appear on the surface or the etching process attacks the Si atoms completely randomly and the etching procedure leaves behind a surface without any long-range order.

The results from the thermal effusion experiment as the temperature is ramped have shown approximately equal numbers of hydrogen atoms, which inhabit mono- and dihydride bonds (see tab. 8.1.1). This contention is a rough approximation and gives a ratio of mono- to dihydride bonds of roughly 2. If we accept the first hypothesis that the surface is a combination of differently oriented plains, it is necessary for a calculation of the internal surface to be performed to know what average area for all orientations per bond can be attributed to the mono- and dihydride, respectively. The difficulty in solving such a problem can be illustrated, for instance, by a comparison of (111) and (110) planes respectively. On both perfectly oriented planes, only monohydrides are present. In the case of (111) orientation, every monohydride corresponds to Am = 12,768 Å^2 while in the case of (110), Am1 = 10,424 Å^2. There is no experimental information about the correlation of the two orientations on the skeleton surface. One possible compromise to escape the deadlock is to consider the internal surface as composed only of (111) (and equivalent) and (100) (and equivalent) planes. The first orientation is representative for the monohydrides and the second for the dihydrides. The correlation between the areas of the differently oriented planes is determined from the experimentally obtained ratio of the mono- to dihydride bonds and the corresponding areas per bond for the two types of bonds and selected orientations. In the case of (100) planes, the area per dihydride bond is Ad = 14,74245 Å^2. In accordance with the accepted rough approximation for the mono- to dihydride bond number ratio, the surface area of the skeleton can be expressed as:

$$S = \frac{N_H Am}{2} + \frac{N_H Ad}{4} = \frac{N_H}{2}\left(Am + \frac{Ad}{2}\right). \tag{9.3}$$

For the surface area to volume ratio of the skeleton,

$$\begin{aligned} \frac{S}{V} &= \frac{N_H}{N_{Si}} \frac{1}{2V_e}\left(Am + \frac{Ad}{2}\right) \approx \\ &\approx 0.5 \frac{N_H}{N_{Si}} \quad \left[\text{Å}^{-1}\right] \end{aligned} \tag{9.4}$$

is valid.

This ratio could be converted into a linear dimension for the particles only if their shape were known. We consider the shape of the internal surface to be extremely complicated. An acceptable model of the porous structure skeleton represents it as consisting of interconnected particles. The shape of these particles is responsible for the shape of the internal surface. Conversely, the adopted shape of the internal surface requires an appropriate choice of these particles. This choice, in its turn, determines a set of independent parameters, which characterize the skeleton. It is expedient that the number of these parameters be minimised. It has to be mentioned that none of the methods we use gives direct information about the particles' shape. In conformity with the possible interpretations of the results from the thermal effusion and transmission infrared spectroscopy measurements, we propose two forms of the particles forming the skeleton. Having in mind the adopted compromise on determining the surface area, the particle configuration, presented on fig. 9.1, corresponds very well to the concept that different orientations appear on the surface. The bounding surface of the body consists of six identical {100}-oriented quadrates and eight uniform {111}-oriented irregular hexagons. Each of the quadrates has an area of $A_4 = x^2$ inhabited by dihydrides. The area of one irregular hexagon is populated by monohydrides and is equal to $A_6 = \left(-4x^2 + 2xy\sqrt{2} + y^2\right)\frac{\sqrt{3}}{8}$. The accepted rough approximation for the mono- to dihydride bond number ratio leads to the dependence $y \approx 2.05x$. Elementary stereometric calculations give $S_{14} \approx 3.9y^2$ for the bounding surface of the 14-wall body and $V_{14} \approx 0.64y^3$ for its volume. Finally, for the surface area to volume ratio of the selected particle form, we obtain:

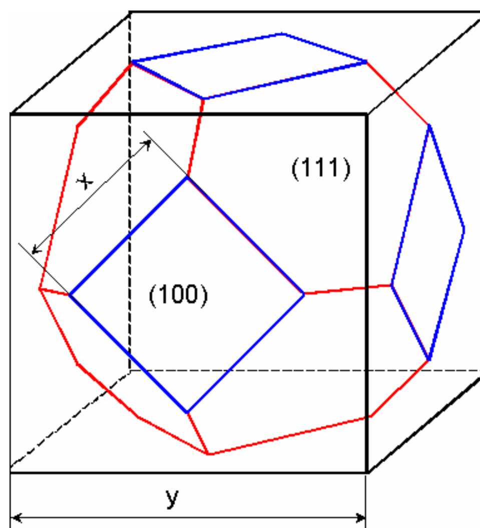

Fig. 9.1: 14-wall body as building element of the skeleton

$$\frac{S_{14}}{V_{14}} \approx \frac{6.1}{y} \tag{9.5}$$

We can consider the experimentally determined volume, V, of the skeleton as a sum of the volumes of such 14-wall bodies with an edge distribution function f(y):

$$V = 0.64 \int_{y_{min}}^{y_{max}} f(y) y^3 dy = 0.64 n y_{eff}^3 . \tag{9.6}$$

This final result can be interpreted as a replacement of the 14-walled body assemblies with an edge distribution function f(y) by an assembly of n number such identical bodies with an effective edge of y_{eff}. For the surface area of the skeleton constructed by these bodies, the equation $S = 3.9 n y_{eff}^2$ is valid and for its surface area to volume ratio:

$$\frac{S}{V} \approx \frac{3.9 n y_{eff}^2}{0.64 n y_{eff}^3} \approx \frac{6.1}{y_{eff}} \tag{9.7}$$

A combination of eqs. (9.4) and (9.7) allows a representation of the dependence of the characteristic parameter y_{eff} on the experimentally determined $\frac{N_H}{N_{Si}}$ ratio:

$$y_{eff} \approx 12.2 \left(\frac{N_H}{N_{Si}} \right)^{-1} \quad [\text{Å}]. \tag{9.8}$$

The results from the thermal effusion and the infrared transmission spectroscopy enable the unusual concept of a curved crystal surface to be accepted (see sections 8.1.4. and 8.2.5.). Such a crystal surface shape appears only because of the specific formation conditions: the electrochemical etching and the possible subsequent local reconstruction. "This type of reconstruction of a step facet contains a relatively high degree of freedom in the bond angles and permits strain in the bonds which can round off corners and steps" [see *Reppich*]. The particle shape in this case, answering the requirements for a minimum number of characteristic parameters, is the sphere described through its radius (or diameter). X-ray investigations on porous silicon [see *Franz*] support such an assumption. It has to be emphasized once more that the spherical shape is only one approximation allowing us to characterize such a complicated structure as porous silicon.

Having m spheres, with a radius distribution function f(r), which fill the experimentally determined volume V of the skeleton, we can average

$$V = \frac{4}{3}\pi \int_{r_{min}}^{r_{max}} f(r) r^3 dr = m \frac{4}{3}\pi r_{eff}^3 = m\pi \frac{d_{eff}^3}{6} . \tag{9.9}$$

This means that the skeleton can be considered, effectively, as composed of m identical

spherical particles of radius (diameter) $r_{eff}(d_{eff})$. For the entire surface S of the spheres, the equation:

$$S = m4\pi r_{eff}^2 = m\pi d_{eff}^2 \tag{9.10}$$

is valid.

Constructing the surface to volume ratio by means of expressions (9.4), (9.9) and (9.10), one obtains the following formula:

$$\frac{S}{V} = \frac{6}{d_{eff}} \approx 0.5\frac{N_H}{N_{Si}} \text{ or,}$$

$$d_{eff} \approx 12\left(\frac{N_H}{N_{Si}}\right)^{-1} \quad [\text{Å}]. \tag{9.11}$$

It is seen that by means of the discussed assumptions from the experimentally determined N_H and N_{Si} one can obtain the characteristic parameter of the particles. A comparison of eqs. (9.8) and (9.11) persuades us that the choice of particle shape in the considered cases is not critical to a determination of the magnitude of the characteristic parameter and that differences between calculated results are insignificant.

Another approach for a determination of d_{eff} is also possible. This procedure allows the uncertainties connected with the orientation of the internal surface to be treated in a different manner. Such an approach corresponds to the second possible interpretation of the results from the thermal effusion and infrared transmission spectroscopy measurements, which allows that the etching procedure leaves behind a surface without any long-range order. One can consider a sphere as cut out from a piece of silicon monocrystal. For this purpose, the Si-Si bonds between the Si atoms on the surface of the sphere and their neighbours, which remain outside the sphere, have been broken. With this procedure, "dangling bonds" have been created on the surface. For some of the atoms, only one bond has been broken. For others, two bonds are broken and there are atoms with three broken bonds. For single crystal silicon, the number of atoms with one, two and three "dangling bonds", respectively, and their relationship, could be calculated precisely and it was discovered that this relationship depends on the diameter of the sphere. The procedure described resembles the porous silicon production process. In this case, the "dangling bonds" can be considered as saturated by hydrogen atoms. Thus, the number of broken bonds is equal to the number of experimentally determined hydrogen atoms.

The program utilized delivers the results in a form of a table (see tab. 6.1, chapter 6) with seven columns. The first column shows the diameter of the sphere. The second, third and

fourth columns contain the numbers of SiH, SiH_2 and SiH_3 bonds respectively. The fifth column expresses the number of the Si atoms enclosed by the spherical surface. The sixth column comprises the hydrogen to silicon atom number ratio N_H/N_{Si} and the last column the reciprocal quantity N_{Si}/N_H. The formula connecting the ratio N_{Si}/N_H with the diameter of the particles is linear

$$\frac{N_{Si}}{N_H} = A + Bd_{eff} \text{ or,}$$

$$d_{eff} = \frac{1}{B}\left(\frac{N_{Si}}{N_H} - A\right) \approx 10.49\left(\frac{N_{Si}}{N_H} - 0.22\right) \quad (9.12)$$

where A=0.22269 and B=0.09531.

9.2. Results and comments

An important result, which the data in table 9.1 illustrate and assert, is that increasing the di- to monohydride number ratio, and parallel to it the hydrogen to silicon atom number ratio, decreases the diameter of the spherical particles forming the skeleton. The smaller the

Position of the luminescence peak maximum (eV)	$\mathbf{N_H/N_{Si}}$	**characteristic parameter (Å)**		
		(approach: combination of {100} and {111})		**(approach: sphere cutout) $\mathbf{d_{eff}}$**
		14-walls body $\mathbf{y_{eff}}$	**sphere $\mathbf{d_{eff}}$**	
1.02	0.13	94	92	78
1.5	0.36	34	33	27
1.57	0.37	33	32	26
1.65	0.45	27	27	21
1.75	0.42	29	29	23
1.82	0.46	27	26	20
1.92	0.60	20	20	15
2.00	0.78	16	15	11

Tab.9.1: Peak luminescence energy vs. average particle characteristic parameter.

diameter, the stronger is the curvature of the spherical surface. Thus, certain a dependence between the surface curvature, on the one hand, and the distribution of the different hydrides and the surface to volume ratio (see section 4.2.), on the other hand, is established.

In table 9.1, the results obtained by applying both approaches to the experimentally obtained N_H/N_{Si} data are presented independently of how the samples were produced. The difference between the results of the two methods is not considerable. Applying the scheme with a combination of {100} and {111} orientations, which gives results about 25% higher, we used an estimate of the di- to monohydrides bonds number ratio. It is seen in tab. 8.1.1 that a value of 0.5 is a relatively rough approximation to be applied to all investigated samples. Since this value can be determined by thermal effusion as the temperature is ramped, it is recommended that such a measurement always be performed parallel to the other methods in order to enhance the accuracy. This measurement will also expose the possible influence of the production procedure (e.g. with illumination or in the darkness) on the internal surface properties. This is a task for further work in this field.

In our opinion, three additional factors have to be commented upon as relevant to the particle size determination. The **first** factor takes into account the fact that, to form a mechanically stable system, the particles actually have to be interconnected. For definiteness, we shall discuss the problem for a spherical particle shape, but the treatment is valid for any other shape. Having calculated the surface to volume ratio of the skeleton, the diameter of the spheres can be determined. It is easy to show that the interconnection between the particles of a certain diameter leads to a change of their surface to volume ratio if the diameter is already fixed. This ratio has a minimum. For example, in the simplest case of two particles, this is when the distance between their centres is equal to the sum of their radii. One can repeat the calculation with the reduced surface to volume ratio corresponding to an increased effective diameter for another system of separated identical spheres. This means that to every system of interconnected identical spheres of a certain radius and of a certain surface to volume ratio, one can juxtapose another system of separated spheres of a certain radius and the same surface to volume ratio. At the new radius for the interconnected spheres, the spacing will be smaller than the radius of the separated spheres. In other words, any experimentally obtained surface to volume ratio can be related to one system of separated identical spheres of a larger effective diameter and to other systems of interconnected identical spheres of a smaller effective diameter. The length of this diameter depends on the degree of interconnection. For a correct determination of the diameter, it appears necessary for the degree of interconnection to be characterized. We only note this problem because we don’t have any available

experimental information. A borderline case is when the cylindrical shape (observed in the mesoporous structure) can be treated as formed by many connected spheres. The same is valid for the elliptical particle shape. Such a shape is obtained by optical measurements. In both cases, an effective reduction of the surface to volume ratio is valid. This is true to an even greater degree for the cylindrical shape.

The **second** factor is the possible presence of reconstruction. This effectively causes an increase of the mono- to dihydride bond ratio and, according to the chosen method for surface area assessment, its underestimation. In reality, one has a greater area representing a d_{eff} smaller than that calculated. The value of 0.5 adopted as a rough approximation for the considered ratio in our approach eliminates the effect of reconstruction.

A similar influence on the surface to volume ratio has the presence of a certain number of dangling bonds on the surface as the **third** factor. In this case, Si atoms, which are not bonded to hydrogen and are therefore excluded from the area of calculation, are available on the surface. Thus, the area obtained is underestimated and consequently d_{eff} is in fact smaller than calculated.

The particle size is influenced by a combination of these factors. An estimation of the quantitative contribution of each of these is impossible because of a lack of experimental data. One could only speculate about which contribution is more significant so the three factors discussed illustrate the limitations of this approach for particle size estimation.

Irrespective of the difficulties in arriving at a determination of the exact particle size, the increasing of the surface to volume ratio and the parallel and independently obtained increase of the SiH_2/SiH ratio with the blue shift of the luminescence, in our opinion, speaks clearly of the decisive influence of the size effect on the porous silicon properties.

9.3. Comparison with the available data from the literature

The following pictures present comparatively the data obtained by different methods, which we have found in the literature together with the results in the current work. Both theoretical results (fig. 9.2) and experimental data (fig. 9.3) are shown. Two groups of theoretical results are included. The first of these refers to an energy band gap versus the diameter of the particles and the second is related to the excitonic energy gap versus the diameter, which is denoted in brackets on the figure.

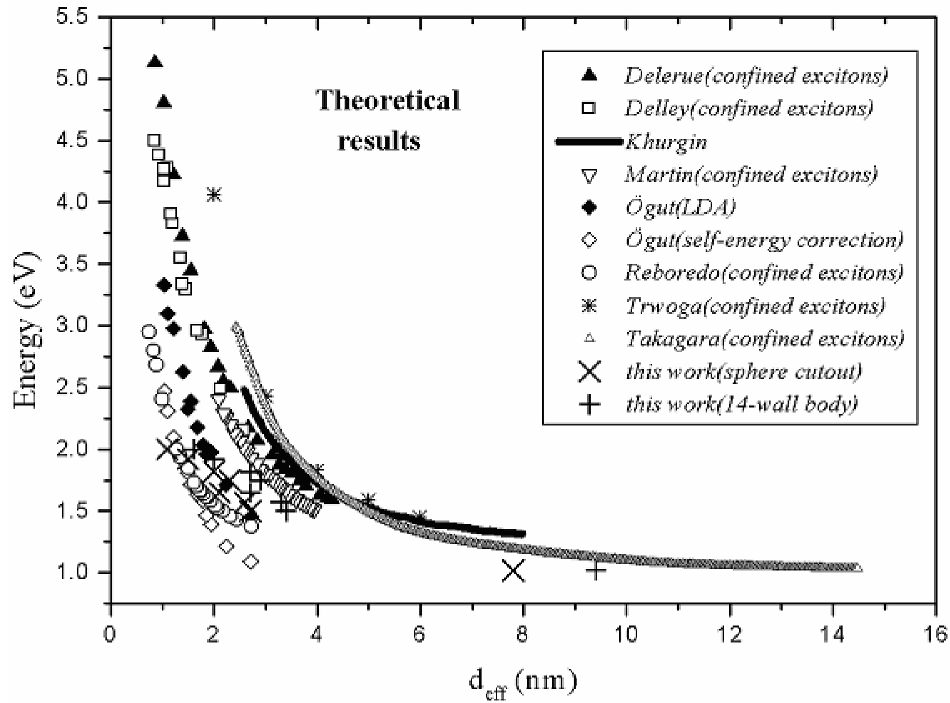

Fig.9.2: Comparison of the available theoretical results with those of the current work.

Among the theoretical data are:

Delerue et al. [see *Delerue*] calculated the electronic and optical properties of silicon crystallites using a technique for the linear combination of atomic orbitals; the LCAO technique.

Delley et al. [see *Delley*] presented the size dependence of the energy band gap for hydrogen saturated silicon clusters computed using all electron density functional theory.

Khurgin et al. [see *Khurgin*] proposed a model of the quantum nanocrystallites as blocks with three unequal sides, each of which is an independent random variable distributed around a common average size, and performed a computer simulation of their emission spectrum.

Takagahara et al. [see *Takagahara*] investigated the quantum confinement effect on excitons in nanostructures of indirect-gap materials and calculated the exciton transition energy, exciton binding energy and exciton oscillator strength.

Martin et al. [see *Martin*] used a tight-binding configuration-interaction technique to calculate the binding energies of excitons in crystallites with respect to the particle size.

Ögüt et al. [see *Ögut*] presented calculations from first principles using a real-space higher-order finite-difference pseudopotential method of the quasiparticle gaps, self-energy corrections, exciton Coulomb energies and optical gaps in Si quantum dots for hydrogen-passivated spherical Si clusters. The calculations were performed within the local density approximation (LDA). The size dependence of the LDA band gaps and the self-energy corrections are shown.

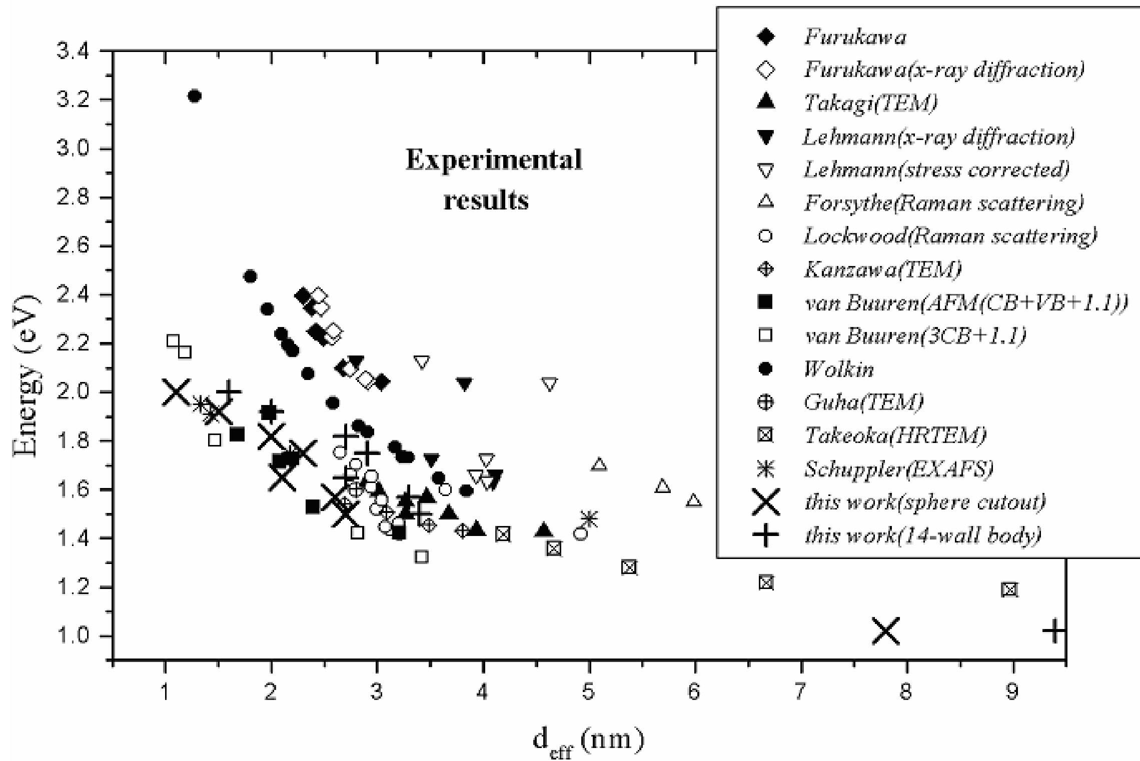

Fig.9.3: Comparison of the available experimental results with that of the current work.

Reboredo et al. [see *Reboredo*] utilized pseudopotential calculations of the single-particle states of Si quantum dots and a direct evaluation of the screened electron-hole Coulomb interaction. The full excitonic spectrum of these dots is described by using a many-body expansion that includes both Coulomb and exchange electron-hole terms and the predicted excitonic spectra are presented.

Trwoga et al. [see *Trwoga*] suggested that the major contribution to luminescence in silicon nanoclusters was from radiative recombination of confined excitons. Utilizing the effective mass approximation, they considered the variation in oscillator strength with cluster size. By varying both the mean cluster size and size distribution of silicon nanoclusters, the luminescence spectra are modeled.

Among the experimental data are:

Furukawa et al. [see *Furukawa*] deduced the average microcrystal size from the half-width of the (111) diffraction peak for materials fabricated by means of a planar magnetron r.f. sputtering technique in hydrogen gas onto a low temperature $(\sim 100\ \mathrm{K})$ substrate. To confirm the results, they made supplementary estimates of the average microcrystal size using formula for the diameter of small spherical silicon particles surrounded by hydrogen atoms (which are bonded in the form of SiH_2).

Takagi et al. [see *Takagi*] investigated Si microcrystallites embedded in a Si oxide matrix

and determined the crystallite size from the half width of the (111) line of x-ray diffraction (XRD).

Lehmann et al. [see *Lehmann*] calculated the average size of crystalline microparticles from the broadening of x-ray diffraction lines and also showed stress corrected size data for electrochemically prepared porous structures.

Forsythe et al. [see *Forsythe*] used Raman scattering to estimate the particle size of quantum nanocrystals formed from Si embedded in a SiO_2 matrix.

Lockwood et al. [see *Lockwood*] used the shift down in frequency of the bulk Si optical mode at $520.0\ cm^{-1}$ and the Raman linewidth modeling for the size determination in the ideal case of spheres in samples prepared by electrochemical dissolution of Si in HF-based electrolyte followed by extended chemical dissolution in the dark.

Kanzawa et al. [see *Kanzawa*] investigated Si nanocrystals embedded in SiO_2 films which were prepared by r.f. cosputtering of Si and SiO_2 and post-annealing. The average particle sizes were directly estimated by high-resolution transmission electron microscopic observations.

Van Buuren et al. [see *Van Buuren*] synthesized silicon nanocrystals by thermal vaporization of Si in an argon buffer gas followed by exposure to atomic hydrogen to passivate the surface. They utilized high-resolution atomic force microscope (AFM) measurements of the cluster size.

Wolkin et al. [see *Wolkin*] didn't mention explicitly how they had determined the size of the particles in their samples. The PSi structures were formed by electrochemical etching followed by photoassisted stain etching. Being based on other publications from the same research group [see *von Behren*], we concluded that the Raman spectroscopy had been applied to identify the average crystallite size.

Guha [see *Guha*] presented a study of Si^+ ions implanted into silica glasses and estimated the average particle size from the width and shift of the phonon peak as compared to the bulk phonon mode at $522\ cm^{-1}$.

Takeoka et al. [see *Takeoka*] studied Si nanocrystals embedded in SiO_2 matrices prepared by an r.f. cosputtering method followed by annealing in a gas atmosphere. The cross-sectional high-resolution transmission electron microscope (HRTEM) image was used for the particle size determination.

Schuppler et al. [see *Schuppler*] utilized the method which is extensively discussed in chapter 6.

References

1. *Sze* S.M. Sze, Physics of Semiconductor Devices, John Wiley, New York (1981).
2. *Reppich* Thin Film Handbook, ed. H.S. Nalwa, Academic Press, to be published.
3. *Franz* H. Franz, V. Petrova-Koch, T. Muschik, V. Lehmann and J. Peisl, Mat. Res. Soc. Symp. Proc. **283**, 133 (1993).
4. *Delerue* C. Delerue, G. Allan, and M. Lanoo, Phys. Rev. B **48**(15), 11024 (1993).
5. *Delley* B. Delley and F. Steigmeier, Appl. Phys. Lett. **67**(16), 2370 (1995).
6. *Khurgin* J.B. Khurgin, E.W. Forsythe, S.I. Kim, B.S. Sywe, B.A. Khan, and G.S. Tompa, Mat. Res. Soc. Symp. Proc. **358**, 193 (1995).
7. *Takagahara* Toshide Takagahara and Kyozaburo Takeda, Phys. Rev. B **46**(23), 15578 (1992).
8. *Martin* E. Martin, C. Delerue, G. Allan, and M. Lannoo, Phys. Rev. B **50**(24), 18258 (1994).
9. *Ögut* Serdar Ögut and James R. Chelikowsky, Steven G.Louie, Phys. Rev. Lett. **79**(9), 1770 (1997).
10. *Reboredo* F. A. Reboredo, A. Franceschetti, and A. Zunger, submitted to Phys. Rev. B.
11. *Trwoga* P. F. Trwoga, A. J. Kenyon, and C. W. Pitt, J. Appl. Phys. **83**(7), 3789 (1998).
12. *Furukawa* Shoji Furukawa and Tatsuro Miyasato, Phys. Rev. B **38**(8), 5726 (1988).
13. *Takagi* H. Takagi, H. Ogawa, Y. Yamazaki, and T. Nakagiri, Appl. Phys. Lett. **56**(24), 2379 (1990).
14. *Lehmann* V. Lehmann, B. Jobst, T. Mushik, A. Kux, and V. Petrova-Koch, Jap. J. Appl. Phys. **32**, 2095 (1993).
15. *Forsythe* E. W. Forsythe, E. A Whittaker, F. H. Pollak, B. S Sywe, G. S. Tompa, B. A. Khan, J. Khurgin, H. W. H. Lee, F. Adar, H. Schaffer, Mat. Res. Soc. Symp. Proc. **358**, 87 (1995).
16. *Lockwood* D. Lockwood and A. G. Wang, Electrochemical Society Proc. **25**, 166 (1995).
17. *Kanzawa* J. Kanzawa, T. Kageyama, S. Takeoka, M. Fijii, S. Hayashi, and K. Yamamoto, Sol. State Comm. **102**, 533 (1997).
18. *Van Buuren* T. van Buuren, L. N. Dinh, L. L. Chase, W. J. Siekhaus, and L. J. Terminello, Phys. Rev. Lett. **80**, 3803 (1998).

19. *Wolkin* M. V. Wolkin, J. Jorne, and P. M. Fauchet, Phys. Rev. Lett. **82**, 197 (1999).

20. *von Behren* J. von Behren, T. Van Buuren, M. Zacharias, E. H. Chimowitz, and P. M. Fauchet, Solid State Commun. **105**, 317 (1998).

21. *Guha* Soumyendu Guha, J. Appl. Phys. **84**, 5210 (1998).

22. *Takeoka* Shinji Takeoka, Minoru Fujii, and Shinji Hayashi, Phys. Rev. B **62**, 16820 (2000).

23. *Schuppler* S. Schuppler, S.L. Friedmann, M.A. Marcus, D.A. Adler, Y.-H. Xie, F.M. Ross, T.D. Harris, W.L. Brown, Y.J. Chabal, L.E. Brus, and P.H. Citrin, Phys. Rev. Lett., **72**(16), 2648 (1994).

Chapter 10. SUMMARY

The aim of this work is the size of the particles, building the skeleton of the porous silicon structure, to be assessed. As a main method, the thermal effusion in its two versions has been utilized. The thermal effusion at a constant temperature combined with the gravimetry has delivered the number of the hydrogen and the silicon atoms, respectively. The H/Si atom number ratio is considered as a standard for the surface to volume ratio of the porous silicon structure. To verify the obtained results there have been involved some other appropriate methods for composition determination. The elastic recoil detection analysis confirmed the thermal effusion results in the whole range of etching current densities, as a structure determining parameter. The “burning” method was productive for the mesoporous samples. In such way, the last two methods served as arbitrators for the clarification of the controversies between the experimental results from the extended x-ray absorption fine structure method and the thermal effusion in favor of the last one.

Interrelation of the hydrogen to silicon atom number ratio and the luminescence maximum position for various porous silicon samples is experimentally established. This position is used as a basis for a comparison between samples produced by different structure determining parameters and from different researcher groups.

Assuming the hydrogen to be bound only on the internal surface, the density of H atoms per unit area and the form of the particles are necessary to assess the size of the particles by means of the H/Si atom number ratio. The thermal effusion as the temperature is ramped and the transmission infrared spectroscopy have shown that most probably all orientations appear on the internal surface, and the hydrogen is roughly equally distributed respectively on the mono- and the dihydrides. Two particle forms are suggested as the most suitable approximations, what is in accordance with the interpretation of the results from the last two considered methods. Such forms satisfy the condition for a minimal number of the independent parameters for their characterization. Considering the internal surface as composed of both planes (111) and equivalent, representative for the monohydrides, and (100) and equivalent, representative for the dihydrides, an estimation of its area and the particle size is made. This approach gives a good agreement with the available theoretical and experimental literature data. The lack of experimental information about the degree of interconnection between the particles, the presence of reconstruction and dangling bonds are factors, which limit the precision of the estimation.

The most important results of this work are as follow:

- It was utilized an original method of investigation – the thermal effusion, especially in its realization at a constant temperature. Combined with the gravimetry, this approach enables the hydrogen to silicon atom number ratio for the studied porous structure in the whole interval of interest to be determined. Two other methods, which measure the same quantity, are also involved. Comparing the obtained results for equally prepared samples, the thermal effusion data show a good agreement with the experimental data from the elastic recoil detection analysis. For mechanically unstable structures the last method is inapplicable unlike the thermal effusion. The great differences from the results obtained by the extended x-ray absorption fine structure method are explained with a wrong interpretation of the experimental data. In addition, it has to be remarked that the two supplementary methods require incomparable more expensive equipment and all limitations, connected with using of an accelerator.

All those considerations make clear that for the selected approach of a particle size estimation the thermal effusion method has an important role.

The good agreement of the obtained results in the current work with all available results for particle size estimation in the porous structure confirms the appropriateness of the selected approach, whose inseparable ingredient are the thermal effusion results.

- The literature data from the extended x-ray absorption fine structure method are extensively analyzed. The role of the atom displacement and bond distortion on the internal surface for the correct interpretation of the experimental data is pointed out.

- Interrelation between the value of the H/Si atom number ratio and the position of the luminescence peak for different porous structures has been established. The larger the values of the considered ratio are, the larger the shift of the luminescence peak to higher energies is.

- The experimental results refute the superposed conception that the internal surface of the porous structure is [100] (or equivalent [010] and [001]) oriented. Most probably, on this surface appear all orientations with many steps and corners.

- The critical analysis of the literature data reveals significant controversies in the assignment of the features in the porous silicon IR transmission spectrum, which could not be surmounted by the current work. The origin of the differences is pointed out. Improvements in the experimental conditions are suggested for further investigations.

- The role of the oxygen for the studied characteristics of the porous structure and the oxidative effect of the rinse in alcohol is commented. All experimental results attest the absence of significant oxygen presence in the as-prepared porous structure. A proper handling

procedure is offered, which enables the samples to remain free of oxidation on air at least two hours after preparation.

- The experimental data show that the population of the internal surface is mainly by mono- and dihydrides. An interrelation between the dihydrides to monohydrides number ratio and the position of the luminescent peak is established. The larger the considered ratio the bigger the shift of the luminescence peak to higher energies is. The increase of the SiH_2/SiH number is characteristic for reducing the diameter of the particles building the porous silicon skeleton.

- An approach is suggested to estimate the particle size, assuming their form, from the obtained experimental data. The grounds for the selected approximation are pointed out. The factors limiting the accuracy of the selected approach are commented.

- **Irrespective of the difficulties at determination of the exact particle size, the increasing of the surface to volume ratio and the parallel and independently obtained increase of the** SiH_2/SiH **number ratio with the blue shift of the luminescence, in our opinion speaks clearly for the decisive influence of the quantum size effect on the porous silicon properties.**

DANKSAGUNG

An dieser Stelle möchte ich mich gerne ganz herzlich bei allen bedanken, die zum Gelingen dieser Arbeit beigetragen haben.

An erster Stelle geht mein Dank an Prof. Frederick Koch, Ph.D., der mir die Möglichkeit gegeben hat, dieses interessante Thema an seinem Institut E16 zu bearbeiten, und der die Dissertation mitgetragen hat. Er hat die Arbeit über den ganzen Zeitraum geduldig begleitet und sich immer wieder kritisch mit dem Thema und den erreichten Ergebnissen auseinandergesetzt. Nicht zuletzt danke ich ihm auch für die finanzielle Unterstützung, die ich im Laufe der Arbeit erhalten habe.

Frau Dr. Vesselinka Petrova-Koch bin ich zu großem Dank verpflichtet für ihre wichtigen Impulse und Beiträge insbesondere zu Beginn der Arbeit.

Herzlich danken möchte ich Dr. Horia Porteanu für seine vielseitige unschätzbare Unterstützung im Laufe der Arbeit, trotz seiner vielfältigen eigenen Aufgaben. Besonders wertvoll war für mich seine stete Bereitschaft, an thematischen Diskussionen als kritischer Zuhörer teilzunehmen.

Die Effusions–Messungen entstanden im Kristall-Labor des Physik-Departments. Herrn Heiko Schneider danke ich ganz herzlich dafür, dass er immer bereit war, seine fundierte experimentelle Erfahrung mit mir zu teilen. Bei ihm und allen Mitarbeitern des Kristall-Labors möchte ich mich besonders bedanken für den Teamgeist und die stetige Hilfsbereitschaft, die ich dort erfahren durfte.

Die ERDA–Messungen wurden von der Gruppe von Prof. G. Dollinger am Lehrstuhl E12 durchgeführt. Dr. A. Bergmaier hat dankenswerter Weise das entsprechende Kapitel in der Dissertation kritisch durchgesehen.

Für die „Burning"–Messungen konnte auf die entsprechende Apparatur am Lehrstuhl für Anorganische und Analytische Chemie im Chemie–Department zurückgegriffen werden. Prof. Schmidtbaur hat die Anwendung dieser Methode empfohlen und Hr. Barth hat die Durchführung der Experimente unterstützt.

Prof. Dmitri Kovalev hat mir sehr wertvolle Tipps für die Realisierung der optischen Messungen gegeben.

Ein grosser Teil der Infrarot-Transmissons–Messungen wurde in Zusammenarbeit mit Dr. B.

WURFEL von Lehrstuhl für Physikalische Chemie am Chemie Department durchgeführt. Mir wurde auch die Möglichkeit gegeben die entsprechende Apparatur am Lehrstuhl für Materialwissenschaften (PROF. DR. S. VEPREK) im Chemie–Department zu benutzen.

Sehr wertvoll Hilfe durfte ich durch PROF. P. JAKOB (E 20) erfahren. Die Diskussionen mit ihm haben ganz wesentlich zur Klärung offener Fragestellungen bei den Ergebnissen der Thermischen Effusion und der Infrarot-Transmissions–Messungen beigetragen. Auch die zahlreichen Gespräche mit PROF. TH. DITTRICH und PROF. V. TIMOSHENKO waren für die Lösung dieser Probleme sehr hilfreich.

Meinen Kollegen und Freunden DR. WOLFGANG STADLER, DR. THOMAS FISCHER und DR. THOMAS MUSCHIK bin ich sehr dankbar für ihre Hilfsbereitschaft, ihre vielseitige Unterstützung und vor allem auch für die aufrichtige Freundschaft, die während meines Aufenthalts an E16 entstanden ist.

Bei PROF. L. VATSKICHEV (Uni Sofia), PROF. M. ARNAUDOV (Uni Sofia), DR. B. IVANOVA(Uni Sofia), PROF. D. MALINOVSKA (BAW) und PROF. A. MANOV (BAW) bedanke ich mich für die kritische Durchsicht des Manuskripts.

Ein Wort des Dankes geht auch an die Sekretärinnen FRAU VERONIKA ENTER und FRAU LAURA DARABAS. Sie haben mich durch ihre Hilfsbereitschaft und Menschlichkeit beeindruckt und standen mir vor allem auch bei allen administrativen Problemen zur Seite.

Der Werkstattmannschaft von E16 danke ich für die rasche Erledigung meiner vielfältigen Aufträge.

B. PETKOV gebührt mein Dank für seine Hilfe bei der technischen Realisierung der Doktorarbeit.

T. WHALEN und S. MARKOVSKA danke ich für die sprachliche Korrektur des Manuskripts.

Meine besondere Dankbarkeit gilt meinem Freund T. CANOV für seine große moralische Unterstützung.

Allen, die noch nicht namentlich genannt wurden und einen Beitrag zu dieser Dissertation geleistet haben, sei an dieser Stelle noch einmal Dank gesagt!

Ich widme diese Arbeit meiner verstorbenen Großmutter, die mich großgezogen hat, und meiner Tante Pobeda, die mich in meinem Leben immer wieder so großzügig unterstützt hat.